

ASSOCIATION OF TOO SHORT ARCS USING ADMISSIBLE REGION

A Thesis

Submitted to the Faculty

of

Purdue University

by

Surabhi Bhadauria

In Partial Fulfillment of the

Requirements for the Degree

of

Master of Science

May 2020

Purdue University

West Lafayette, Indiana

**THE PURDUE UNIVERSITY GRADUATE SCHOOL  
STATEMENT OF THESIS APPROVAL**

Dr. Carolin Frueh, Chair

School of Aeronautics and Astronautics

Dr. David Spencer

School of Aeronautics and Astronautics

Dr. Kathleen Howell

School of Aeronautics and Astronautics

**Approved by:**

Dr. Gregory Blaisdell

Head of the School Graduate Program

*Dedicated to my loving grandmother, grandfather,  
mother and father*

## ACKNOWLEDGMENTS

I am immensely grateful to all who have been a constant support to me in this journey. It has been quite a ride switching to Aeronautics and Astronautics from Materials and Metallurgical Engineering and would not have been possible without the following people believing in me.

Firstly, I would like to thank my advisor, Dr. Carolin Frueh, for guiding me in the right direction to pursue my dream. She has been a wonderful and a cheerful mentor, which always makes research a fun process. I would also like to extend my gratitude to my committee members, Dr. Kathleen Howell and Dr. David Spencer. Dr. Howell's course on orbital mechanics really sparked my interest in astrodynamics. My lab mates have been a huge help in solving some problems and providing feedback on the thesis. As a graduate assistant, I am also greatly thankful to Teaching and Learning Technologies Team at Purdue for lifting the financial burden off me.

I am who I am because of my family. They have always given me the freedom to make choices and supported them throughout. I feel extremely fortunate and thankful to my *Dadi, Baba, Maa, Papa*, my brother *Vishwajeet* and my sister-in-law *Pragya* for always being there for me.

Lastly, I would like to thank my friends - Rashmi, Sachin, Neha, Prasoon, Romila, Gaurav, Prashansa, Vinu, Priyanshi, Rohith, Clément, Aakriti, Karan who have been a nonstop source of my happiness. A special thanks to little Aisha for getting more fun in life through Friday art sessions. A heartfelt thanks to my roommates - Ayesha and Harshita, for making the transition from India to US smooth and comforting.



## TABLE OF CONTENTS

	Page
LIST OF TABLES . . . . .	viii
LIST OF FIGURES . . . . .	ix
ABBREVIATIONS . . . . .	xii
ABSTRACT . . . . .	xiii
1 INTRODUCTION . . . . .	1
1.1 Objective . . . . .	4
1.1.1 Assumptions . . . . .	5
1.1.2 Chapter Outline . . . . .	5
2 PROBABILITY PRELIMINARIES . . . . .	7
2.1 Gaussian Distribution . . . . .	8
2.1.1 Covariance Transformation Using Jacobian [19] . . . . .	9
3 COORDINATE SYSTEMS . . . . .	12
3.1 Geocentric Equatorial System . . . . .	12
3.2 Topocentric Equatorial System . . . . .	14
3.3 Topocentric Local Horizon Coordinate System . . . . .	17
4 ORBITAL ELEMENT SPACES . . . . .	20
4.1 Keplerian Orbital Elements . . . . .	20
4.2 Delaunay Orbital elements . . . . .	28
5 ADMISSIBLE REGION . . . . .	30
5.1 With Energy Constraint . . . . .	30
5.2 With Semimajor Axis And Eccentricity Constraint [14] . . . . .	33
5.3 Example Of An Admissible Region . . . . .	35
6 APPROXIMATING THE ADMISSIBLE REGION USING GAUSSIAN MIX- TURE MODEL . . . . .	38

	Page
6.1 Application To The Admissible Region . . . . .	40
6.2 Approximating Univariate GMM For Range . . . . .	41
6.3 Approximating Bivariate GMM For Range-Rate . . . . .	43
7 FILTERING TECHNIQUES . . . . .	48
7.1 Kalman Filter . . . . .	48
7.1.1 Kalman Filter Initialization . . . . .	49
7.1.2 Kalman Filter Prediction . . . . .	49
7.1.3 Kalman Filter Update . . . . .	50
7.2 Extended Kalman Filter . . . . .	51
7.2.1 Extended Kalman Filter Initialization . . . . .	51
7.2.2 Extended Kalman Filter Prediction . . . . .	52
7.2.3 Extended Kalman Filter Update . . . . .	52
7.2.4 Numerical Error Build-up During EKF . . . . .	55
8 INFORMATION MEASURES . . . . .	59
8.1 KL Divergence Between Gaussian Mixture Models . . . . .	61
8.1.1 All Components . . . . .	62
8.1.2 Using Optimized Matching . . . . .	62
9 MONTE-CARLO SIMULATIONS . . . . .	64
10 SIMULATION MODEL . . . . .	69
10.1 Sensor Measurement Model . . . . .	69
10.2 Target Motion Model . . . . .	70
10.3 Simulation Procedure . . . . .	71
10.3.1 GEO Objects . . . . .	72
10.3.2 LEO Objects . . . . .	74
11 RESULTS . . . . .	76
11.1 GEO Unsorted And Propagated In Cartesian Coordinates . . . . .	76
11.2 GEO Sorted And Propagated In Cartesian Coordinates . . . . .	89
11.3 GEO Unsorted And Propagated In Keplerian Orbital Elements . . . . .	102

	Page
11.4 LEO Scenario 1 . . . . .	114
11.5 LEO Scenario 2 . . . . .	123
12 SUMMARY . . . . .	133
12.1 Conclusions . . . . .	133
12.2 Recommendations . . . . .	136
REFERENCES . . . . .	137

## LIST OF TABLES

Table	Page
7.1 Comparison of volume of uncertainty between classical and state transition matrix method for covariance propagation . . . . .	57
9.1 Mahalanobis distance in different frames . . . . .	67

## LIST OF FIGURES

Figure	Page
2.1 Normal density function . . . . .	9
3.1 Right ascension and declination . . . . .	13
3.2 Topocentric Local Horizon coordinate system . . . . .	18
4.1 Classical orbital elements . . . . .	21
5.1 Admissible Region with zero energy constraint . . . . .	36
5.2 Region of admissible range/range-rate values given angle and angle rate data and eccentricity as 0.8 . . . . .	37
6.1 Illustration of the process for computing a Gaussian mixture approxima- tion of the range-marginal PDF . . . . .	43
6.2 Gaussian mixture representation of the constrained Admissible Region with 206 components . . . . .	46
6.3 Gaussian mixture representation of the constrained Admissible Region with 97 components . . . . .	46
6.4 Gaussian mixture representation of the constrained Admissible Region with 807 components . . . . .	47
7.1 Gaussian mixture representation of the constrained Admissible Region . .	54
8.1 All components with all components for two GMMs . . . . .	63
8.2 Optimized matching of components for two GMMs . . . . .	63
9.1 Position of Monte-Carlo points and mean in range range-rate space . . . .	66
9.2 Position of Monte-Carlo points and mean transformed to Keplerian orbital elements . . . . .	67
9.3 Position of Monte-Carlo points and mean transformed to Delaunay orbital elements . . . . .	67
10.1 Flowchart for finding KL divergence of object 1 with itself after EKF . . .	74
10.2 Flowchart for finding KL divergence of object 1 with object 2 . . . . .	74
11.1 Plot of GEO objects with orbits . . . . .	77

Figure	Page
11.2 Plot for KL divergence vs case number for 10 minutes of propagation time using optimized matching of components for GEO scenario 1 . . . . .	78
11.3 Plot for KL divergence vs case number for 10 minutes propagation time using all components for GEO scenario 1 . . . . .	80
11.4 Plot for KL divergence vs case number for 30 minutes propagation time using optimized matching of components for GEO scenario 1 . . . . .	82
11.5 Plot for KL divergence vs case number for 30 minutes propagation time using all components for GEO scenario 1 . . . . .	84
11.6 Plot for KL divergence vs case number for 30 minutes propagation time using optimized matching of components for GEO scenario 1 . . . . .	86
11.7 Plot for KL divergence vs case number for 30 minutes propagation time using all components for GEO scenario 1 . . . . .	88
11.8 Plot of GEO objects with orbits close to each other . . . . .	90
11.9 Plot for KL divergence vs case number for 10 minutes propagation time using optimized matching of components for GEO scenario 2 . . . . .	91
11.10 Plot for KL divergence vs case number for 10 minutes propagation time using all components for GEO scenario 2 . . . . .	93
11.11 Plot for KL divergence vs case number for 30 minutes propagation time using optimized matching of components for GEO scenario 2 . . . . .	95
11.12 Plot for KL divergence vs case number for 30 minutes propagation time using all components for GEO scenario 2 . . . . .	97
11.13 Plot for KL divergence vs case number for 500 minutes propagation time using optimized matching of components for GEO scenario 2 . . . . .	99
11.14 Plot for KL divergence vs case number for 500 minutes propagation time using all components for GEO scenario 2 . . . . .	101
11.15 Plot for KL divergence vs case number for 10 minutes propagation (in Keplerian orbital elements) time using optimized matching of components for GEO scenario 3 . . . . .	103
11.16 Plot for KL divergence vs case number for 10 minutes propagation (in Keplerian orbital elements) time using all components for GEO scenario 3	105
11.17 Plot for KL divergence vs case number for 30 minutes propagation (in Keplerian orbital elements) time using optimized matching of components for GEO scenario 3 . . . . .	107

Figure	Page
11.18Plot for KL divergence vs case number for 30 minutes propagation (in Keplerian orbital elements) time using all components for GEO scenario 3	109
11.19Plot for KL divergence vs case number for 500 minutes propagation (in Keplerian orbital elements) time using optimized matching of components for GEO scenario 3 . . . . .	111
11.20Plot for KL divergence vs case number for 500 minutes propagation (in Keplerian orbital elements) time using all components for GEO scenario 3	113
11.21Plot of LEO objects with orbits for scenario 1 . . . . .	115
11.22Plot for KL divergence vs case number for 3 minutes propagation time using optimized matching of components for LEO scenario 1 . . . . .	116
11.23Plot for KL divergence vs case number for 3 minutes propagation time using all components for LEO scenario 1 . . . . .	118
11.24Plot for KL divergence vs case number for 10 minutes propagation time using optimized matching of components for LEO scenario 1 . . . . .	120
11.25Plot for KL divergence vs case number for 10 minutes propagation time using all components for LEO scenario 1 . . . . .	122
11.26Plot of LEO objects with orbits for scenario 2 . . . . .	124
11.27Plot for KL divergence vs case number for 3 minutes propagation time using optimized matching of components for LEO scenario 2 . . . . .	125
11.28Plot for KL divergence vs case number for 3 minutes propagation time using all components for LEO scenario 2 . . . . .	127
11.29Plot for KL divergence vs case number for 10 minutes propagation time using optimized matching of components for LEO scenario 2 . . . . .	129
11.30Plot for KL divergence vs case number for 10 minutes propagation time using all components for LEO scenario 2 . . . . .	131

## ABBREVIATIONS

GMM	Gaussian Mixture Model
EKF	Extended Kalman Filter
GEO	Geostationary Earth Orbits
MEO	Medium Earth Orbits
LEO	Low Earth Orbits
PDF	Probability Distribution Function
AEOE	Alternate Equinoctial Orbital Elements
KOE	Keplerian Orbital Elements
CART	Cartesian Coordinates
TLE	Two Line Element
KL	Kullback Leibler divergence
MD	Mahalanobis distance
USSTRATCOM	US Strategic Command



# ABSTRACT

Bhadauria, Surabhi M.S., Purdue University, May 2020. Association of Too Short Arcs using Admissible Region. Major Professor: Carolin Frueh.

The near-Earth space is filled with over 300,000 artificial debris objects with a diameter larger than one cm [1]. For objects in GEO and MEO region, the observations are made mainly through optical sensors. These sensors take observations over a short time which cover only a negligible part of the object's orbit. Two or more such observations are taken as one single Too Short Arc (TSA). Each set of TSA from an optical sensor consists of several angles, the angles of right ascension ( $\alpha$ ), declination ( $\delta$ ), along with the rate of change of the right ascension angle ( $\dot{\alpha}$ ) and the declination angle ( $\dot{\delta}$ ). However, such observational data obtained from one TSA because it is covering only a very small fraction of the orbit, is not sufficient for the complete initial determination of an object's orbit. For a newly detected unknown object, only TSAs are available with no information about the orbit of the object. Therefore, two or more such TSAs that belong to the same object are required for its orbit determination. To solve this correlation problem, the framework of the probabilistic Admissible Region is used, which restricts possible orbits based on a single TSA. To propagate the Admissible Region to the time of a second TSA, it is represented in closed-form Gaussian Mixture representation. This way, a propagation with an Extended Kalman filter is possible. To decide if two TSAs are correlated, that is if they belong to the same object, respectively, an overlap between the regions is found in a suitable orbital mechanic's based coordinate frame. To compute the overlap, the information measure of Kullback-Leibler divergence is used.

## 1. INTRODUCTION

The near-Earth space is filled with over 300,000 artificial debris objects with a diameter larger than one cm [1]. This space containing debris is divided into three main regions based on the altitude from Earth's surface: the Low Earth Orbit (LEO), the Medium Earth Orbit (MEO), and the Geosynchronous Earth Orbit (GEO), which cover the altitudes below 2,000 km, between 2,000 km and 35,586 km, and between 35,586 km and 35,986 km, respectively. The orbits of certain unclassified spacecrafts/objects in these three regions are publicly made available by US Strategic Command (USSTRATCOM). This catalogue features objects with sizes above ten cm in LEO and larger than one meter-sized debris in GEO but is far from complete even within these size ranges. Currently, about 17,000 objects are being tracked on a continuous basis. The orbital data corresponding to each of these objects is available in the two-line element (TLE) format by USSTRATCOM. The TLE format provides only the orbital element data and gives no information on the uncertainty associated with it.

In the observation and detection of new objects, the sky is scanned in an organized manner. For objects in MEO and GEO, observations are usually done using optical sensors. Each set of observations made on a given object during a short period of time is called a Too Short Arc (TSA), which is also sometimes referred to as a tracklet or an uncorrelated observation [2]. These observations consist of angular observations, which are combined in a TSA, having information on angles and angle-rates. Thus, a TSA from an optical sensor consists of four quantities: the angles of right ascension ( $\alpha$ ) and declination ( $\delta$ ), along with the rate of change of the right ascension angle ( $\dot{\alpha}$ ) and the declination angle ( $\dot{\delta}$ ). However, such observational data obtained from one TSA is not sufficient for the complete initial determination of an object's orbit because one TSA covers only a small fraction of an object's orbit. For a complete initial

determination of an object's orbit, one requires six unknown independent quantities (which are discussed later), whereas as outlined above a single TSA only provides information on four quantities because of the short time over which the observations were collected. Thus, to determine each of the six orbital elements, one, therefore, requires observational data from more than one set of TSA measurements belonging to the same object.

For known objects, TSAs can be used to update and improve the existing orbits, e.g. known from the TLEs. However, for a newly detected unknown object, only TSAs are available. Therefore, it is required to correlate TSAs to find out if they belong to the same object. As the number of objects increase, it becomes even more difficult to associate TSAs in order to even start a successful initial orbit determination procedure. Therefore, the correlation/identification problem associated with TSAs needs to be solved first before the desired object's orbit can be determined. The central goal of the correlation problem is to determine whether two or more sets of TSAs belong to the same object.

In literature, a couple of approaches have been adopted to address this correlation problem. The TSA problem has been analysed by Milani et al. [3], in which the authors provide a full algebraic description of an Admissible Region which restricts the possible orbits captured by a central body that can be represented by an attributable  $(\alpha, \dot{\alpha}, \delta, \dot{\delta})$  and range range-rate values by putting an energy constraint. A later work by Milani et al. [4] also provide an algorithm to find a preliminary orbit which could fit two attributables with small residuals. This is done by using the minimum identification penalty for each of the attributables. Another popular approach for correlation of the two independent too short arc observations is to compare the covariances and fit the two arcs together [5]. Tommei et al. [2] discuss the definition of the Admissible Region for space debris, both in the case of optical observations and radar observations for Earth bound objects. Maruskin et al. [6] introduce mapping of Admissible Region in Delaunay orbit element space for correlating the second observation. Farnocchia et al. [7] discuss two methods for solving the linkage problem:

the first method exploits Admissible Region to generate virtual objects which are propagated in time to find second observation belonging to the same object, and the second method leverages the integrals of two-body problem which are constant for a significant time span and thus should apply to both observed arcs of the same object. Fujimoto and Scheeres [8] propose a technique of correlating multiple ground-based optical observations using highly constrained probability distribution in Poincare orbit element space. They have also studied the same for space-based observations in [9]. Milani et al. [10] provide a virtual debris algorithm and Keplerian integrals method for objects based on sparse optical data. The concept of sampling the Admissible Region using Delaunay triangulation for generating virtual space objects from two observations for drawing a comparison between them has also been studied by Khoury and Frueh in [11]. Musci and Schildknecht et al. [12] present the idea of generating a circular orbit from a single TSA and then further improving that orbit using follow-up observations for better determination of elliptical orbits. The follow-up TSAs have been correlated based on the circular orbits with tight restrictions on the time between TSAs. This approach did not involve the use of an Admissible Region. Holzinger, Scheeres and Alfrend have demonstrated the utility of using control efforts for correlating the space objects [13].

The concept of using information measures to find the overlap between two probability distributions which represent the TSAs is studied for correlating them, an approach that is not explored in any of the previous works. In this thesis, a representation of the Admissible Region via Gaussian Mixture Model (GMM) is chosen. This can be done by approximating the Admissible Region by a Gaussian Mixture Model [14]. The GMM presents the Admissible Region in terms of mean and covariance of Gaussian components which can further be propagated to time  $t_2$  using the concept of Extended Kalman filter (EKF) [15]. EKF propagation gives the GMM obtained from observation one at time  $t_2$ . The Admissible Region obtained from observation two at time  $t_2$  can also be approximated by GMM. Furthermore, these two GMMs associated with two different observations can be used to find the overlap be-

tween two observations. Kullback-Leibler (KL) divergence [16], also known as relative entropy, is one such tool which gives a measure of the overlap between two probability distributions. For propagating the Admissible Region to time  $t_2$ , the GMM has to be transformed to a suitable coordinate frame, such as Cartesian coordinates or Keplerian orbital elements. Different coordinate frames show different overlap between two same Admissible Regions. To compute the overlap between two Admissible Regions, a suitable coordinate frame has to be found. The choice of coordinate frame is dictated by the mandate that, for the true orbit, the state at  $t_1$  and  $t_2$  are repeated or are at least very closely correlated. This is true for Keplerian orbital elements, which are constant for a two-body orbit, or for Delaunay elements, which are action angles along with their conjugate momenta. This is not expected in range range-rate space and Cartesian coordinates as the state of the object changes continuously. A major challenge is that the transformations between the frames are non-linear and Gaussianity is not preserved. Despite the potential advantages KL divergence offers, there has only been limited research on utilizing this tool for finding out the overlap between Gaussians mixture models obtained from the Admissible Region of two observations. The major focus of this work is to bridge this gap by applying the KL divergence to solve the correlation problem.

### 1.1 Objective

The central aim of this research work is to solve the correlation problem associated with two independent Too Short Arcs. The framework used for this work is based on the probabilistic interpretation of the Admissible Region. For solving the correlation problem, the aim is to find answers to the following questions:

- Can a Gaussian Mixture Model (GMM) representation of the Admissible Region in combination with utilizing the Extended Kalman Filter and Kullback-Leibler divergence as an information measure be leveraged to address the correlation problem?

- Is there a specific orbital element space or coordinate frame preferable for finding the overlap between two GMMs?
- Can a correlation decision still be made in the presence of linearizations for various time spans of Too Short Arcs?

### 1.1.1 Assumptions

- All the objects are bound by earth's gravity
- Two-body motion of an object without any perturbations is considered for the propagation of an object
- No process noise is taken into account for the propagation of uncertainty

### 1.1.2 Chapter Outline

Chapter 2 explains the basic probability concepts used in this thesis. It introduces mean, covariance, normal distribution and Jacobians. Chapter 3 describes the fundamentals of the Geocentric Equatorial coordinate system, the Topocentric coordinate system and the Topocentric Local Horizon coordinate system in detail. It also details how to transform mean and covariance from one frame to another. Chapter 4 focuses on the Keplerian orbital elements and Delaunay orbital elements. It further details the transformations relating the mean and covariance of a GMM from Geocentric equatorial system to Keplerian orbital element spaces. Chapter 5 describes the concept of the Admissible Region and discusses its utility and application to optical observations. Furthermore, this chapter also discusses the application of the semi-major axis and eccentricity constraint on the Admissible Region. In Chapter 6, the framework of approximating an Admissible Region using a Gaussian Mixture Model is presented. The process of creating a bivariate Gaussian Mixture Model from range range-rate values are explained in detail. Chapter 7 includes the basics of the Kalman filter and Extended Kalman filter. The utility of these computational

techniques to specific applications is also discussed. This is followed by a discussion on the initialization, prediction and updating steps associated with the filter. Finally, the numerical challenges presented by using a numerical integrator are discussed in detail. Chapter 8 describes the statistical tool: Kullback-Leibler divergence and how it can be applied to Gaussian Mixture Models. Chapter 9 presents the Monte-Carlo simulations that have been performed to evaluate the robustness of the implemented transformations from one space to other. Chapter 10 defines the sensor measurement model, target motion model used in the simulations. It also describes the various scenarios associated with the Geosynchronous and Low-Earth orbits. Chapter 11 details the results generated from GEO scenarios, LEO scenarios followed by discussions on them. Chapter 12 summarizes the work done for this thesis and also presents suggestions for future work.

## 2. PROBABILITY PRELIMINARIES

A random variable  $x$  is a variable that takes on values at random and realizations of the random variable may be thought of as the outcomes of some random experiment [17]. A probability distribution function is the density of probability of the event that a random variable  $x$  takes on in its vicinity.

For a random variable, the expectation is defined as the sum of all values that the random variable may take, each multiplied by the probability at that value of  $x$ .

$$\mu = E\{x\} = \int_{-\infty}^{\infty} xp(x)dx \quad (2.1)$$

It is also referred to as the mean distribution of  $x$  (denoted by  $\mu$ ) or the first moment of  $x$ . The quantity  $E\{x^n\}, n \geq 1$  is called the  $n$ th moment of  $x$ . Although the expectation of a random variable gives the weighted average of the possible values of  $x$ , it does not give any information about the variation, or spread, of these values. Two variables can have an equal expectation with varying spread around them. The variance of  $x$  is defined as the mean squared deviation of the random variable from its mean. It is denoted by  $\sigma^2$ .

$$\sigma^2 = \int_{-\infty}^{\infty} (x - E\{x\})^2 p(x) dx \quad (2.2)$$

$$= E\{(x - E\{x\})^2\} \quad (2.3)$$

It is also referred to as the second moment of  $x$ . For two random variables, the covariance is given by the expectation of the product of the deviations of the random variables from their respective means.



$$E\{(x - E\{x\})(y - E\{y\})\} = \int_{-\infty}^{\infty} \int_{-\infty}^{\infty} (x - E\{x\})(y - E\{y\})p(x, y)dxdy \quad (2.4)$$

$$= E\{xy\} - E\{x\}E\{y\} \quad (2.5)$$

## 2.1 Gaussian Distribution

The Gaussian or normal distribution has been introduced by the French mathematician Abraham DeMoivre in 1733 to approximate the binomial random variables with large  $n$  [18]. It is a symmetric distribution having a bell-shaped curve and a peak at the center of the distribution. A Gaussian distribution can be fully described by defining its mean and variance or spread as all the higher moments are exactly zero. For a normal random variable  $x$ , the probability density of  $x$  is given by

$$f(x) = \frac{1}{\sqrt{2\pi}\sigma} e^{-(x-\mu)^2/2\sigma^2} \quad -\infty < x < \infty \quad (2.6)$$

The density function is symmetric about the mean of  $x$ . For a Gaussian distribution, the first two moments i.e mean and variance are sufficient to describe it.

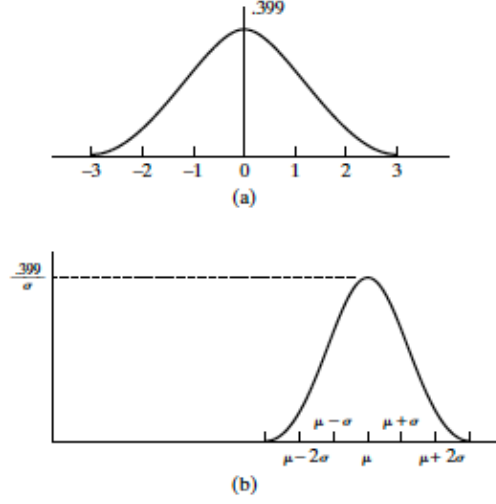


Fig. 2.1.: Normal density function: (a)  $\mu = 0, \sigma = 1$ ; (b) arbitrary  $\mu, \sigma^2$  [18]

### 2.1.1 Covariance Transformation Using Jacobian [19]

For the transformation of a probability density function from one system to another, Jacobians can be used. The Jacobian is a linearization and provides the ability to compute an approximation of the true second moment after the transformation. The mean can be transformed via point transformation. The Jacobian is derived as the following, using Taylor series expansion. Consider Taylor expansion of a function  $F(x)$  about  $x_0$ , with  $x - x_0 = h$

$$F(x) = F(x_0) + h \frac{dF(x_0)}{dx} + \frac{h^2}{2!} \frac{d^2F(x_0)}{dx^2} + \dots \quad (2.7)$$

where

$$\frac{dF(x_0)}{dx} = \left. \frac{dF}{dx} \right|_{x=x_0}, \quad \frac{d^2F(x_0)}{dx^2} = \left. \frac{d^2F}{dx^2} \right|_{x=x_0}, \quad (2.8)$$

For a function in two variables  $F(x,y)$ , the Taylor series expansion about a point  $(x_0, y_0)$  is given as

$$F(x, y) = F(x_0, y_0) + h \frac{dF(x_0, y_0)}{dx} + k \frac{dF(x_0, y_0)}{dy} + \quad (2.9)$$

$$\frac{1}{2!} \left\{ h^2 \frac{d^2 F(x_0, y_0)}{dx^2} + 2hk \frac{d^2 F(x_0, y_0)}{dxdy} + k^2 \frac{d^2 F(x_0, y_0)}{dy^2} \right\} + \dots \quad (2.10)$$

where

$$\frac{dF(x_0, y_0)}{dx} = \left. \frac{dF}{dx} \right|_{x=x_0, y=y_0}, \quad \frac{d^2 F(x_0, y_0)}{dx^2} = \left. \frac{d^2 F}{dx^2} \right|_{x=x_0, y=y_0}, \quad (2.11)$$

Now, consider the pair of ODEs in the variables  $x(t)$  and  $y(t)$

$$\dot{x} = F(x, y) \quad \dot{y} = G(x, y) \quad (2.12)$$

To study the behavior near a particular point  $(x_0, y_0)$ , take the Taylor expansion using  $h(t) = x(t) - x_0$  and  $k(t) = y(t) - y_0$

$$\dot{h} = h \frac{dF(x_0, y_0)}{dx} + k \frac{dF(x_0, y_0)}{dy} + \dots \quad (2.13)$$

$$\dot{k} = h \frac{dG(x_0, y_0)}{dx} + k \frac{dG(x_0, y_0)}{dy} + \dots \quad (2.14)$$

After ignoring the higher-order terms, these can now be written in the matrix form as

$$\dot{X} = JX \quad (2.15)$$

where  $X(t) = (h, k)^T$  and the matrix is called the Jacobian matrix

$$J = \begin{bmatrix} \left. \frac{dF}{dx} \right|_{(x_0, y_0)} & \left. \frac{dF}{dy} \right|_{(x_0, y_0)} \\ \left. \frac{dG}{dx} \right|_{(x_0, y_0)} & \left. \frac{dG}{dy} \right|_{(x_0, y_0)} \end{bmatrix} \quad (2.16)$$

The transformation equation for covariance matrix  $P$  is

$$P' = JPJ^T \quad (2.17)$$

As stated above, this Jacobian is just an approximation by ignoring higher terms in Taylor series. In a non-linear transformation, Gaussianity is not preserved. Using the linearization of the Jacobian, an approximation of the second moment of the new probability density function can be provided. No higher moments are provided, hence a complete reconstruction of the probability distribution function is not possible.

Often, as only two moments are available, the new probability distribution function is treated as a Gaussian in the new space, although this is, of course, a crude approximation even when the true second moment is close to the estimated one, as higher moments are ignored.

### 3. COORDINATE SYSTEMS

A coordinate system is defined by specifying its origin, fundamental plane, sense (right-handed sense or left-handed sense) and the preferred direction. The coordinate systems covered in this chapter are all Earth-based systems with the origin at either Earth's center (geocentric) or Earth's surface (topocentric). This chapter also explains how the state of an object and the uncertainty associated with it can be transformed from one coordinate system to others. During the course of this work, Geocentric Equatorial coordinate system, Topocentric Equatorial coordinate system and Topocentric Local Horizon coordinate system ( [20], [21], [17] ) have been used for different purposes like Extended Kalman filtering [15] and calculating Kullback-Leibler divergence [16].

#### 3.1 Geocentric Equatorial System

This system originates at the center of the Earth and is one of the most commonly used systems in astrodynamics. The reference direction, origin, plane associated with the Geocentric Equatorial system are as follows:

- Origin: centre of the Earth
- Fundamental plane: equator at a fixed equinox
- Reference direction: vernal equinox at a fixed equinox
- Handedness: right-handed system
- Coordinates: right ascension  $\alpha$ , declination  $\delta$ , radial distance  $r$

The state of the object is defined in terms of its geocentric position and velocity. The position and velocity in terms of angles and their rate of change with time can be given as

$$\begin{bmatrix} x \\ y \\ z \end{bmatrix} = \begin{bmatrix} r \cos \alpha \cos \delta \\ r \sin \alpha \cos \delta \\ r \sin \delta \end{bmatrix}, \quad (3.1)$$

$$\begin{bmatrix} \dot{x} \\ \dot{y} \\ \dot{z} \end{bmatrix} = \begin{bmatrix} \dot{r} \cos \alpha \cos \delta - r \cos \delta \sin \alpha \dot{\alpha} - r \sin \delta \cos \alpha \dot{\delta} \\ \dot{r} \sin \alpha \cos \delta - r \sin \delta \sin \alpha \dot{\alpha} + r \cos \delta \cos \alpha \dot{\alpha} \\ \dot{r} \sin \delta + r \cos \delta \dot{\delta} \end{bmatrix}, \quad (3.2)$$

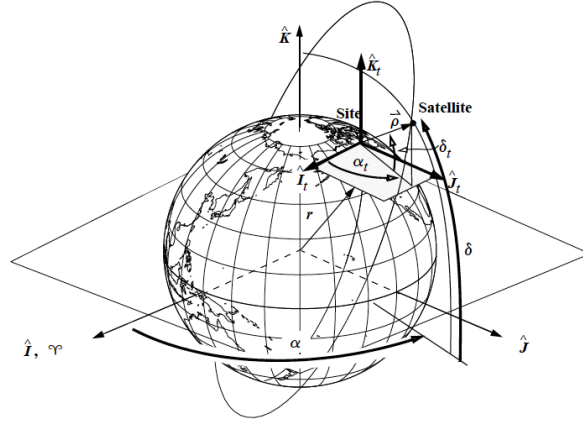


Fig. 3.1.: **Right Ascension and Declination.** Geocentric right ascension ( $\alpha$ ) and declination ( $\delta$ ) use the Earth's Equatorial plane. Topocentric right ascension ( $\alpha_t$ ) and declination values ( $\delta_t$ ) use a plane parallel to the Earth's equator but located at a particular site. [22]

$\alpha$  is the in-plane angle and defined to be zero for the direction to the vernal equinox,  $\delta$  defines the angle above or below the equator (South pole =  $-\pi/2$ , North pole =  $\pi/2$ ) counted from the equator plane.

The angles are related to position and velocity using following equations:

$$\begin{aligned}
r &= \sqrt{x^2 + y^2 + z^2} \\
\tilde{r} &= \sqrt{x^2 + y^2} \\
\delta &= -\frac{\pi}{2}, 0, \frac{\pi}{2} \quad \text{for } \tilde{r} = 0 \quad \text{and} \quad z > 0, z = 0, z < 0 \\
\delta &= \tan^{-1} \left( \frac{z}{\tilde{r}} \right) \quad \text{for } \tilde{r} \neq 0 \\
\alpha &= 0 \quad \text{for } x = 0 \quad \text{and} \quad y = 0 \\
\alpha &= \phi \quad \text{for } x \geq 0 \quad \text{and} \quad y \geq 0 \\
\alpha &= 2\pi + \phi \quad \text{for } x \geq 0 \quad \text{and} \quad y \leq 0 \\
\alpha &= 2\pi + \phi \quad \text{for } x \leq 0 \\
\phi &= 2 \tan^{(-1)} \left( \frac{y}{|x| + \tilde{r}} \right)
\end{aligned} \tag{3.3}$$

The Geocentric Equatorial system is also a good approximation of an inertial system. Figure 3.1 shows the coordinates in Geocentric Equatorial system.

### 3.2 Topocentric Equatorial System

Since most of the observations are performed at the surface of the Earth, Topocentric Equatorial system becomes handier than Geocentric Equatorial system during such observations. The characteristics associated with this reference system are as follows:

- Origin: topocenter (position of the observer on the Earth surface, time-dependent)
- Fundamental plane: plane parallel to the equator at a fixed equinox
- Reference direction: vernal equinox at a fixed equinox
- Handedness: right-handed system
- Coordinates: right ascension  $\alpha'$ , declination  $\delta'$ , range  $\rho$ , sidereal angle  $\theta$

The terms right ascension and declination are used for both the Topocentric and the Geocentric system. The declination of the zenith (the point directly above the observer) is equal to the geographic latitude of the observer. The right ascension of the zenith depends on the geographic longitude and the time, not on the latitude. For the observations of objects that are at stellar distances, the difference between the Topocentric and Geocentric Equatorial systems are negligible, for Earth-orbiting satellites, the difference is crucial, because of the relatively small distance of the objects relative to the Earth radius.

The sidereal time  $\theta$  is the right ascension of the zenith at a given time  $t$ , the sidereal time of all observers at the same longitudes is the same. The hour angle  $\tau$  is the difference between the sidereal time and the right ascension of an object:  $\tau = \theta - \alpha$ . The sidereal time is hence the hour angle of the vernal equinox. Hence,  $\theta, \tau, \alpha$  are measured often in units of time rather than degrees or radians.  $\phi$  is the geocentric geographic latitude of the observer (Earth fixed).

The state of an object in the Topocentric Equatorial system is defined by  $(\alpha', \dot{\alpha}', \delta', \dot{\delta}', \rho, \dot{\rho})$ . The equations correlating Geocentric Equatorial system to Topocentric Equatorial system are as follows:

$$\begin{bmatrix} r \cos \alpha \cos \delta \\ r \sin \alpha \cos \delta \\ r \sin \delta \end{bmatrix} = \begin{bmatrix} \rho \cos \alpha' \cos \delta' + R \cos \phi \cos \theta \\ \rho \sin \alpha' \cos \delta' + R \cos \phi \sin \theta \\ \rho \sin \delta' + R \sin \phi \end{bmatrix}, \quad (3.4)$$

### **Changing mean and covariance from Topocentric Equatorial System (range and range-rate space) to Geocentric Equatorial system (position and velocity)**

This section discusses about the transformation of mean and covariance from the Geocentric Equatorial system (position and velocity) to the Topocentric Equatorial system (range and range-rate). It will be used for propagation of the GMM (mean and covariance) using Extended Kalman filter and for calculating KL divergence.



Geocentric position and velocity can be found out if the position of topocenter as well position of the object is known.

$$\begin{bmatrix} x \\ y \\ z \end{bmatrix} = \begin{bmatrix} R_{topo,x} + \rho \cos \alpha \cos \delta \\ R_{topo,y} + \rho \sin \alpha \cos \delta \\ R_{topo,z} + \rho \sin \delta \end{bmatrix}, \quad (3.5)$$

$$\begin{bmatrix} \dot{x} \\ \dot{y} \\ \dot{z} \end{bmatrix} = \begin{bmatrix} \dot{R}_{topo,x} + \dot{\rho} \cos \alpha \cos \delta - \rho \cos \delta \sin \alpha \dot{\alpha} - \rho \sin \delta \cos \alpha \dot{\delta} \\ \dot{R}_{topo,y} + \dot{\rho} \sin \alpha \cos \delta - \rho \sin \delta \sin \alpha \dot{\alpha} + \rho \cos \delta \cos \alpha \dot{\alpha} \\ \dot{R}_{topo,z} + \dot{\rho} \sin \delta + \rho \cos \delta \dot{\delta} \end{bmatrix}, \quad (3.6)$$

For covariance transformation, Jacobian can be calculated using the following equations:

$$\begin{aligned} \frac{\partial x}{\partial \alpha} &= -\rho \cos \delta \sin \alpha, & \frac{\partial x}{\partial \dot{\alpha}} &= 0, \\ \frac{\partial x}{\partial \delta} &= -\rho \sin \delta \cos \alpha, & \frac{\partial x}{\partial \dot{\delta}} &= 0, \\ \frac{\partial x}{\partial \rho} &= \cos \delta \cos \alpha, & \frac{\partial x}{\partial \dot{\rho}} &= 0 \\ \frac{\partial y}{\partial \alpha} &= \rho \cos \delta \sin \alpha, & \frac{\partial y}{\partial \dot{\alpha}} &= 0, \\ \frac{\partial y}{\partial \delta} &= -\rho \sin \delta \sin \alpha, & \frac{\partial y}{\partial \dot{\delta}} &= 0, \\ \frac{\partial y}{\partial \rho} &= \cos \delta \sin \alpha, & \frac{\partial y}{\partial \dot{\rho}} &= 0 \\ \frac{\partial z}{\partial \alpha} &= 0, & \frac{\partial z}{\partial \dot{\alpha}} &= 0, \\ \frac{\partial z}{\partial \delta} &= \rho \cos \delta, & \frac{\partial z}{\partial \dot{\delta}} &= 0, \\ \frac{\partial z}{\partial \rho} &= \sin \delta, & \frac{\partial z}{\partial \dot{\rho}} &= 0, \\ \frac{\partial \dot{x}}{\partial \alpha} &= -\dot{\rho} \cos \delta \sin \alpha - \rho \cos \delta \cos \alpha \dot{\alpha} + \rho \sin \delta \sin \alpha \dot{\delta}, & \frac{\partial \dot{x}}{\partial \dot{\alpha}} &= -\rho \cos \delta \sin \alpha, \\ \frac{\partial \dot{x}}{\partial \delta} &= -\dot{\rho} \sin \delta \cos \alpha + \rho \sin \delta \sin \alpha \dot{\alpha} - \rho \cos \delta \cos \alpha \dot{\delta}, & \frac{\partial \dot{x}}{\partial \dot{\delta}} &= -\rho \sin \delta \cos \alpha, \end{aligned} \quad (3.7)$$

$$\begin{aligned}
\frac{\partial \dot{x}}{\partial \rho} &= -\cos \delta \sin \alpha \dot{\alpha} - \sin \delta \cos \alpha \dot{\delta}, & \frac{\partial \dot{x}}{\partial \dot{\rho}} &= \cos \delta \cos \alpha \\
\frac{\partial \dot{y}}{\partial \alpha} &= \dot{\rho} \cos \delta \cos \alpha - \rho \cos \delta \sin \alpha \dot{\alpha} - \rho \sin \delta \cos \alpha \dot{\delta} & \frac{\partial \dot{y}}{\partial \dot{\alpha}} &= -\rho \cos \delta \cos \alpha, \\
\frac{\partial \dot{y}}{\partial \delta} &= -\dot{\rho} \sin \delta \sin \alpha - \rho \sin \delta \cos \alpha \dot{\alpha} - \rho \cos \delta \sin \alpha \dot{\delta} & \frac{\partial \dot{y}}{\partial \dot{\delta}} &= -\rho \sin \delta \sin \alpha, \\
\frac{\partial \dot{y}}{\partial \rho} &= -\sin \delta \sin \alpha \dot{\delta} + \cos \delta \cos \alpha \dot{\alpha}, & \frac{\partial \dot{y}}{\partial \dot{\rho}} &= \cos \delta \sin \alpha \\
\frac{\partial \dot{z}}{\partial \alpha} &= 0, & \frac{\partial \dot{z}}{\partial \dot{\alpha}} &= 0, \\
\frac{\partial \dot{z}}{\partial \delta} &= \dot{\rho} \cos \delta - \rho \sin \delta \dot{\delta}, & \frac{\partial \dot{z}}{\partial \dot{\delta}} &= \rho \cos \delta, \\
\frac{\partial \dot{z}}{\partial \rho} &= \cos \delta \dot{\delta}, & \frac{\partial \dot{z}}{\partial \dot{\rho}} &= \sin \delta,
\end{aligned} \tag{3.8}$$

$$J_{\rho\dot{\rho}\text{-cart}} = \begin{bmatrix} \frac{\partial x}{\partial \alpha} & \frac{\partial x}{\partial \dot{\alpha}} & \frac{\partial x}{\partial \delta} & \frac{\partial x}{\partial \dot{\delta}} & \frac{\partial x}{\partial \rho} & \frac{\partial x}{\partial \dot{\rho}} \\ \frac{\partial y}{\partial \alpha} & \frac{\partial y}{\partial \dot{\alpha}} & \frac{\partial y}{\partial \delta} & \frac{\partial y}{\partial \dot{\delta}} & \frac{\partial y}{\partial \rho} & \frac{\partial y}{\partial \dot{\rho}} \\ \frac{\partial z}{\partial \alpha} & \frac{\partial z}{\partial \dot{\alpha}} & \frac{\partial z}{\partial \delta} & \frac{\partial z}{\partial \dot{\delta}} & \frac{\partial z}{\partial \rho} & \frac{\partial z}{\partial \dot{\rho}} \\ \frac{\partial \dot{x}}{\partial \alpha} & \frac{\partial \dot{x}}{\partial \dot{\alpha}} & \frac{\partial \dot{x}}{\partial \delta} & \frac{\partial \dot{x}}{\partial \dot{\delta}} & \frac{\partial \dot{x}}{\partial \rho} & \frac{\partial \dot{x}}{\partial \dot{\rho}} \\ \frac{\partial \dot{y}}{\partial \alpha} & \frac{\partial \dot{y}}{\partial \dot{\alpha}} & \frac{\partial \dot{y}}{\partial \delta} & \frac{\partial \dot{y}}{\partial \dot{\delta}} & \frac{\partial \dot{y}}{\partial \rho} & \frac{\partial \dot{y}}{\partial \dot{\rho}} \\ \frac{\partial \dot{z}}{\partial \alpha} & \frac{\partial \dot{z}}{\partial \dot{\alpha}} & \frac{\partial \dot{z}}{\partial \delta} & \frac{\partial \dot{z}}{\partial \dot{\delta}} & \frac{\partial \dot{z}}{\partial \rho} & \frac{\partial \dot{z}}{\partial \dot{\rho}} \end{bmatrix} \tag{3.9}$$

Thus, as discussed in chapter 2, the covariance matrix in the Geocentric Equatorial system is given as

$$P_{\text{cart}} = J_{\rho\dot{\rho}\text{-cart}}(P_{\rho\dot{\rho}})J_{\rho\dot{\rho}\text{-cart}}^T \tag{3.10}$$

### 3.3 Topocentric Local Horizon Coordinate System

This system is useful in observing satellites or debris and is used extensively with sensor systems. This reference system rotates along with the rotation of topocenter.

- Origin: Topocenter (position of the observer on the Earth surface, time-dependent)
- Fundamental plane: local horizon

- Reference direction: South (direction, in which places of the same geographic latitude but smaller latitude are located)
- Handedness: left-handed system
- Coordinates: elevation  $h$ , azimuth  $a$ , (normally range  $\rho$  is not reported in this system)

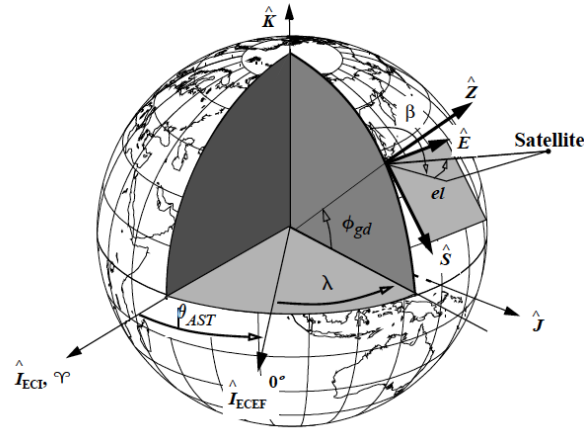


Fig. 3.2.: **Topocentric Local Horizon Coordinate System.** Azimuth ( $\beta$ ) and elevation ( $el$ ) use the Earth's Equatorial plane. Topocentric right ascension ( $\alpha_t$ ) are measured from the topocenter. [22]

Figure 3.2 shows the coordinates in Topocentric Local Horizon coordinate system. Elevation angle  $h$  is the angle above (positive) or below (below) the local horizon. For objects to be visible in the sky, the angle of elevation should be greater than zero. Zenith is defined to be  $\pi/2$ . The azimuth angle is defined from 0 (South) to  $2\pi$ . The transformation from the Topocentric Equatorial system to Topocentric Local Horizon system can be done only using angular measurements.

$$\begin{bmatrix} \cos \alpha' \cos \delta' \\ \sin \alpha' \cos \delta' \\ \sin \delta' \end{bmatrix} = S_2 R_3(\theta) R_2 \left( -\left(\frac{\pi}{2} - \phi\right) \right) \begin{bmatrix} \cos a \cos h \\ \sin a \cos h \\ \sin h \end{bmatrix}, \quad (3.11)$$

This equation can also be written as

$$\begin{bmatrix} \cos a \cos h \\ \sin a \cos h \\ \sin h \end{bmatrix} = \begin{bmatrix} \sin \phi \cos \delta \cos \tau - \cos \phi \sin \delta \\ \sin \tau \cos \delta \\ \sin \phi \sin \delta + \cos \phi \cos \delta \cos \tau \end{bmatrix}, \quad (3.12)$$

For all of these coordinate systems, the state of an object which comprises of six quantities is continuously changing with time due to the movement of the object. Therefore, it might be useful to work in orbital element spaces as five of the six orbital elements remain fixed for an object with time if no perturbation is taken into account. Only the mean or true anomaly of the object changes with time.

## 4. ORBITAL ELEMENT SPACES

This chapter addresses the basics of Keplerian orbital element space and Delaunay orbital element space. It also describes the transformation of state and uncertainty of an object from the Keplerian orbital element to Delaunay orbital elements. The main advantage behind using orbital element spaces is that not all six quantities change with the movement of the object if only two-body dynamics is considered for the motion of the object.

### 4.1 Keplerian Orbital Elements

Keplerian orbital elements space or classical orbital elements space is the most common elements set used for defining orbits of any space object [22]. The six orbital elements are defined as follows (refer figure 4.1):

- Semi-major axis: It is the half of the largest axis of an elliptical orbit. It can be used to derive extreme points in an orbit.
- Eccentricity: It is referred to as the shape of the orbit. It is a non-negative number which characterizes the shape of a conic section. The value of eccentricity for an ellipse is bounded between 0.0 and 1.0.
- Inclination angle: It is referred to as the tilt of an orbit plane. The angle is measured from the unit vector  $\vec{K}$  to the angular momentum vector  $\vec{h}$ . It ranges from  $0^\circ$  to  $180^\circ$ . The inclination angle of  $0^\circ$  and  $180^\circ$  are equatorial orbits, whereas all others are inclined orbits.
- Right ascension of ascending node: It is the angle in the equatorial plane measured positive eastward from the I unit vector to the location of the ascending

node. The ascending node is the point on the equatorial plane at which the satellite crosses the equator from south to north. Inclined orbits also have a descending node at which the satellite crosses from north to south across the equatorial plane. The line joining these two nodes is referred to as the line of nodes. This angle ranges from  $0^\circ$  to  $360^\circ$ .

- Argument of perigee: It is measured from the ascending node in the direction of satellite motion until perigee. This angle also ranges from  $0^\circ$  to  $360^\circ$ .
- True anomaly: This determines the satellite's current position relative to the location of periapsis. This angle also ranges from  $0^\circ$  to  $360^\circ$ .

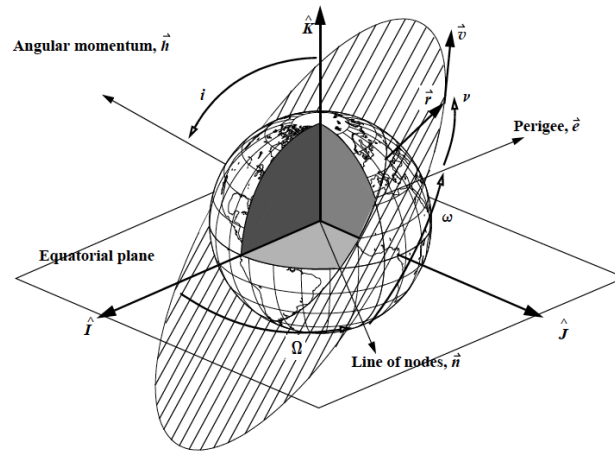


Fig. 4.1.: **Classical Orbital Elements.** The six classical orbital elements are the semimajor axis,  $a$ ; eccentricity,  $e$ ; inclination  $i$ ; right ascension of ascending node,  $\Omega$ ; argument of perigee,  $\omega$ ; and true anomaly,  $\nu$ . [22]

These orbital elements can be calculated from inertial velocity and position using the following equations [22]:

$$\begin{aligned}
 \vec{h} &= \vec{r} \times \vec{v} \quad h = |\vec{h}| \\
 \vec{n} &= \hat{K} \times \vec{h} \\
 \vec{e} &= \frac{(v^2 - \frac{\mu}{r}) \vec{r} - (\vec{r} \cdot \vec{v}) \vec{v}}{\mu} \quad e = |\vec{e}| \\
 \xi &= \frac{v^2}{2} - \frac{\mu}{r} \\
 \text{If } e &\neq 1.0 \quad \text{then} \quad a = -\frac{\mu}{2\xi}, \quad p = a(1 - e^2) \\
 &\quad \text{else} \quad p = \frac{h^2}{\mu}, \quad \text{and} \quad a = \infty
 \end{aligned} \tag{4.1}$$

$$\begin{aligned}
 \cos(i) &= \frac{h_K}{|\vec{h}|} \\
 \cos(\Omega) &= \frac{n_I}{|\vec{n}|} \quad \text{If } (n_J < 0) \quad \text{then} \quad \Omega = 360^\circ - \Omega \\
 \cos(\omega) &= \frac{\vec{n} \cdot \vec{e}}{|\vec{n}||\vec{e}|} \quad \text{If } (e_K < 0) \quad \text{then} \quad \omega = 360^\circ - \omega \\
 \cos(\nu) &= \frac{\vec{e} \cdot \vec{r}}{|\vec{e}||\vec{r}|} \quad \text{If } (\vec{r} \cdot \vec{v} < 0) \quad \text{then} \quad \nu = 360^\circ - \nu
 \end{aligned}$$

For special cases,

Elliptical Equatorial:

$$\cos(\tilde{\omega}_{\text{true}}) = \frac{e_I}{|\vec{e}|} \quad \text{If } (e_J < 0) \quad \text{then} \quad \tilde{\omega}_{\text{true}} = 360^\circ - \tilde{\omega}_{\text{true}}$$

Circular Inclined:

$$\cos(u) = \frac{\vec{n} \cdot \vec{r}}{|\vec{n}||\vec{r}|} \quad \text{If } (r_K < 0) \quad \text{then} \quad u = 360^\circ - u \tag{4.2}$$

Circular Equatorial:

$$\cos(\lambda_{\text{true}}) = \frac{r_I}{|\vec{r}|} \quad \text{If } (r_J < 0) \quad \text{then} \quad \lambda_{\text{true}} = 360^\circ - \lambda_{\text{true}}$$

Here,

$\vec{h}$ : Specific angular momentum,  $\omega$ : Argument of perigee,  $p$ : Semi-parameter,  
 $e$ : Eccentricity,  $a$ : Semi major axis,  $\vec{n}$ : Node vector,  $\nu$ : True anomaly,  
 $\xi$ : Energy,  $i$ : Angle of inclination,  $\Omega$ : Right ascension of ascending node

For a parabolic orbit, the semi-major axis is infinite and therefore can not be determined from the above equations. Similarly, for circular orbits and equatorial orbits, the argument of perigee is not defined as eccentricity is zero and magnitude of  $\vec{n}$  is zero, respectively. This happens because periapsis and the node do not exist for these special cases. The true anomaly of an object is also not defined for perfectly circular orbits. The orbits which approach a circular orbit might cause problems with computer solutions. Therefore, these orbital elements are defined under the special case scenario. These singularities can be overcome by using equinoctial orbital elements which are employed here for transformation from the Geocentric Equatorial system to Keplerian orbital elements.

### **Changing mean and covariance from Geocentric Equatorial system (position and velocity) to Keplerian orbital elements space**

Mean in Geocentric Equatorial system (position  $\vec{r}$  and velocity  $\vec{v}$ ) can be simply transformed to Keplerian orbital elements using equation 4.1. For finding the covariance in Keplerian orbital elements space, as discussed in chapter 2, one way can be by finding the Jacobian between Geocentric Equatorial coordinates to Keplerian orbital elements. Jacobian linearizes the non-linear system of equations which is nothing but an approximation. The direct differential of Keplerian orbital elements with respect to geocentric position and velocity is complicated so firstly Jacobian between the Alternate Equinoctial Orbital Elements (AEOE) and the Geocentric Equatorial system is calculated as an intermediate step. Further, the Jacobian between Alternate



Equinoctial Orbital elements and Keplerian orbital elements is calculated. These two Jacobians when substituted in the equation below give the final Jacobian.

$$\frac{dx^{\text{aeoe}}}{dx^{\text{cart}}} = \frac{dx^{\text{aeoe}}}{dx^{\text{koe}}} \frac{dx^{\text{koe}}}{dx^{\text{cart}}} \quad (4.3)$$

Alternate Equinoctial Orbital elements are used because they are well adapted to orbits with small eccentricity and inclination [23]. They are defined as follows:

$$\begin{aligned} n &= \sqrt{\mu/a^3} \\ h &= e \sin(\omega + \Omega) \\ k &= e \cos(\omega + \Omega) \\ p &= \tan(i/2) \sin \Omega \\ q &= \tan(i/2) \cos \Omega \\ \lambda &= M + \omega + \Omega \end{aligned} \quad (4.4)$$

The position and velocity of the object in the equinoctial frame are given by

$$\begin{aligned} X &= a(\cos E - e) \quad \text{and} \quad Y = a\sqrt{1 - e^2} \sin E \\ \dot{X} &= -\frac{na^2 \sin E}{r} \quad \text{and} \quad \dot{Y} = \frac{na^2 \sqrt{1 - e^2} \cos E}{r} \\ r &= a(1 - e \cos E) \end{aligned} \quad (4.5)$$

Here, E is the eccentric anomaly.

$$L = \frac{a^2}{r}(e \cos E - 1 - \sin^2 E) \quad (4.6)$$

$$M = \frac{a^2 \sin E}{r\sqrt{1 - e^2}}(\cos E - e) \quad (4.7)$$

$$\dot{L} = \frac{na^4}{r^3}(e - 2 \cos E + e \cos^2 E) \sin E \quad \text{and} \quad (4.8)$$

$$\dot{M} = \frac{na^4}{r^3\sqrt{1 - e^2}}(e^2 - 1 - e \cos E + 2 \cos^2 E - e \cos^3 E) \quad (4.9)$$

$$(4.10)$$

A set of auxiliary vectors are introduced as

$$\begin{aligned}
\beta_1 &= L\mathbf{p} + M\mathbf{q} \\
\beta_2 &= \frac{1}{e}[X\mathbf{q} - Y\mathbf{p} - \frac{1}{n}\mathbf{v}^{\text{cart}}] \\
\beta_3 &= X\mathbf{q} - Y\mathbf{p} \\
\beta_4 &= [X \sin(\omega + \Omega) + Y \cos(\omega + \Omega)]\mathbf{r} \\
\beta_5 &= [X \cos(\omega + \Omega) - Y \sin(\omega + \Omega)]\mathbf{r} \\
\beta_6 &= [X \cos(\omega) + Y \sin(\omega)]\mathbf{r}
\end{aligned}$$

and (4.11)

$$\begin{aligned}
\dot{\beta}_1 &= \dot{L}\mathbf{p} + \dot{M}\mathbf{q} \\
\dot{\beta}_2 &= \frac{1}{e}[\dot{X}\mathbf{q} - \dot{Y}\mathbf{p} - \frac{1}{n}\dot{\mathbf{r}}^{\text{cart}}] \\
\dot{\beta}_3 &= \dot{X}\mathbf{q} - \dot{Y}\mathbf{p} \\
\dot{\beta}_4 &= [\dot{X} \sin(\omega + \Omega) + \dot{Y} \cos(\omega + \Omega)]\mathbf{r} \\
\dot{\beta}_5 &= [\dot{X} \cos(\omega + \Omega) - \dot{Y} \sin(\omega + \Omega)]\mathbf{r} \\
\dot{\beta}_6 &= [\dot{X} \cos(\omega) + \dot{Y} \sin(\omega)]\mathbf{r}
\end{aligned}$$

$\mathbf{p}, \mathbf{q}, \mathbf{r}$  are defined as the column vectors of the  $R_3(-\Omega)R_1(-i)R_3(-\omega)$  direction cosine matrix and  $\mathbf{r}^{\text{cart}}, \mathbf{v}^{\text{cart}}$  are the geocentric position and velocity. The Jacobian from Cartesian coordinates to AEOE is given as

$$J_{\text{cart-aeoe}} = \begin{bmatrix} j_{n,\mathbf{r}}^T & j_{n,\mathbf{v}}^T \\ j_{h,\mathbf{r}}^T & j_{h,\mathbf{v}}^T \\ j_{k,\mathbf{r}}^T & j_{k,\mathbf{v}}^T \\ j_{p,\mathbf{r}}^T & j_{p,\mathbf{v}}^T \\ j_{q,\mathbf{r}}^T & j_{q,\mathbf{v}}^T \\ j_{\lambda,\mathbf{r}}^T & j_{\lambda,\mathbf{v}}^T \end{bmatrix} \quad (4.12)$$

where the position related terms are as follows:

$$\begin{aligned}
j_{n,r}^T &= -\frac{3}{na^2} \frac{\mu}{r^3} \mathbf{r}^{\text{cart}} \\
j_{h,r}^T &= \sin(\omega + \Omega) \left[ \frac{-\alpha_1 n (a/r)^3 \mathbf{r}^{\text{cart}} + \dot{\beta}_2}{\alpha_3} \right] - \cos(\omega + \Omega) \left[ \frac{\dot{\beta}_1 + (e\alpha_5/(1-e^2))\dot{\beta}_6}{\alpha_3} \right] \\
j_{k,r}^T &= \sin(\omega + \Omega) \left[ \frac{-\alpha_1 n (a/r)^3 \mathbf{r}^{\text{cart}} + \dot{\beta}_2}{\alpha_3} \right] + \sin(\omega + \Omega) \left[ \frac{\dot{\beta}_1 + (e\alpha_5/(1-e^2))\dot{\beta}_6}{\alpha_3} \right] \\
j_{p,r}^T &= -\frac{\dot{\beta}_4}{\alpha_4(1 + \cos i)} \\
j_{q,r}^T &= -\frac{\dot{\beta}_5}{\alpha_4(1 + \cos i)} \\
j_{\lambda,r}^T &= -\frac{1}{na^2} \left[ \mathbf{v}^{\text{cart}} + \alpha_1 \alpha_2 \dot{\beta}_1 \right] - \left( \frac{\alpha_5}{\alpha_4} \right) \dot{\beta}_6
\end{aligned} \tag{4.13}$$

and the velocity related terms are as follows:

$$\begin{aligned}
j_{n,v}^T &= -\frac{3}{na^2} \mathbf{v}^{\text{cart}} \\
j_{h,v}^T &= -\sin(\omega + \Omega) \left[ \frac{(\alpha_1/n) \mathbf{v}^{\text{cart}} + \beta_2}{\alpha_3} \right] + \cos(\omega + \Omega) \left[ \frac{\beta_1 + (e\alpha_5/(1-e^2))\beta_6}{\alpha_3} \right] \\
j_{k,v}^T &= -\cos(\omega + \Omega) \left[ \frac{(\alpha_1/n) \mathbf{v}^{\text{cart}} + \beta_2}{\alpha_3} \right] - \sin(\omega + \Omega) \left[ \frac{\beta_1 + (e\alpha_5/(1-e^2))\beta_6}{\alpha_3} \right] \\
j_{p,v}^T &= \frac{\beta_4}{\alpha_4(1 + \cos i)} \\
j_{q,v}^T &= \frac{\beta_5}{\alpha_4(1 + \cos i)} \\
j_{\lambda,v}^T &= \frac{1}{na^2} \left[ -2\mathbf{r}^{\text{cart}} + \alpha_1 \alpha_2 \beta_1 \right] + \left( \frac{\alpha_5}{\alpha_4} \right) \beta_6
\end{aligned} \tag{4.14}$$

The auxiliary variables are

$$\begin{aligned}
\alpha_1 &= \frac{e}{1 + \alpha_2}, \quad \alpha_2 = \sqrt{1 - e^2}, \quad \alpha_3 = \frac{na^2}{\alpha_2}, \quad \alpha_4 = na^2 \alpha_2 \\
\alpha_5 &= \frac{\sin i}{1 + \cos i}, \quad \text{and} \quad \alpha_6 = \frac{\sin i}{\alpha_4(1 + \cos i)^2}
\end{aligned} \tag{4.15}$$

These equations give the Jacobian from Cartesian coordinates AEOEs. To find out the Jacobian from Keplerian orbital elements to AEOEs, the following equations can be employed:

$$J_{\text{koe-aeoe}} = \begin{bmatrix} \frac{\partial n}{\partial a} & \frac{\partial n}{\partial e} & \frac{\partial n}{\partial i} & \frac{\partial n}{\partial \omega} & \frac{\partial n}{\partial \Omega} & \frac{\partial n}{\partial M} \\ \frac{\partial h}{\partial a} & \frac{\partial h}{\partial e} & \frac{\partial h}{\partial i} & \frac{\partial h}{\partial \omega} & \frac{\partial h}{\partial \Omega} & \frac{\partial h}{\partial M} \\ \frac{\partial k}{\partial a} & \frac{\partial k}{\partial e} & \frac{\partial k}{\partial i} & \frac{\partial k}{\partial \omega} & \frac{\partial k}{\partial \Omega} & \frac{\partial k}{\partial M} \\ \frac{\partial p}{\partial a} & \frac{\partial p}{\partial e} & \frac{\partial p}{\partial i} & \frac{\partial p}{\partial \omega} & \frac{\partial p}{\partial \Omega} & \frac{\partial p}{\partial M} \\ \frac{\partial q}{\partial a} & \frac{\partial q}{\partial e} & \frac{\partial q}{\partial i} & \frac{\partial q}{\partial \omega} & \frac{\partial q}{\partial \Omega} & \frac{\partial q}{\partial M} \\ \frac{\partial \lambda}{\partial a} & \frac{\partial \lambda}{\partial e} & \frac{\partial \lambda}{\partial i} & \frac{\partial \lambda}{\partial \omega} & \frac{\partial \lambda}{\partial \Omega} & \frac{\partial \lambda}{\partial M} \end{bmatrix} \quad (4.16)$$

Each of the AEOE is differentiated with respect to Keplerian orbital elements (KOE) and the terms in the  $J_{\text{koe-aeoe}}$  are as follows:

$$J_{\text{koe-aeoe}} = \begin{bmatrix} -\frac{3}{2}\sqrt{\frac{\mu}{a^5}} & 0 & 0 & 0 & 0 & 0 \\ 0 & \sin(\omega + \Omega) & 0 & e \cos(\omega + \Omega) & e \cos(\omega + \Omega) & 0 \\ 0 & \cos(\omega + \Omega) & 0 & -e \sin(\omega + \Omega) & -e \sin(\omega + \Omega) & 0 \\ 0 & 0 & \frac{1}{2} \sec^2\left(\frac{i}{2}\right) \sin(\Omega) & 0 & \tan \frac{i}{2} \cos(\Omega) & 0 \\ 0 & 0 & \frac{1}{2} \sec^2\left(\frac{i}{2}\right) \cos(\Omega) & 0 & -\tan \frac{i}{2} \sin(\Omega) & 0 \\ 0 & 0 & 0 & 1 & 1 & 1 \end{bmatrix} \quad (4.17)$$

Using  $J_{\text{koe-aeoe}}$  and  $J_{\text{cart-aeoe}}$  in equation 4.3,  $J_{\text{cart-koe}}$  can be evaluated. Using  $J_{\text{cart-koe}}$ , the covariance matrix in Keplerian orbital elements is given as

$$P_{\text{koe}} = J_{\text{cart-koe}}(P_{\text{cart}})J_{\text{cart-koe}}^T \quad (4.18)$$

## 4.2 Delaunay Orbital elements

Delaunay orbital elements are action-angle coordinates consisting of the argument of periapsis, the mean anomaly and the longitude of the ascending node, along with their conjugate momenta [24]. This element space has singularities at zero eccentricity, zero inclination and critical inclination and therefore they are not defined for circular, equatorial or radial orbits.

- $l$  is the mean anomaly of the object
- $g$  is the argument of periapsis of the object
- $h$  is the right ascension of ascending node
- $L$  is related to the two-body orbital energy
- $G$  is the magnitude of orbital angular momentum
- $H$  is the z-component of the orbital angular momentum vector

### Changing mean and covariance from Keplerian orbital elements to Delaunay orbital elements

Mean from Keplerian orbital elements space to Delaunay orbital elements space can be calculated using the following equations:

$$\begin{aligned}
 l &= M \\
 g &= \omega \\
 h &= \Omega \\
 L &= \sqrt{\mu/a} \\
 G &= L\sqrt{1-e^2} \\
 H &= G \cos i
 \end{aligned}
 \tag{4.19}$$

For finding the Jacobian from Keplerian orbital elements space to Delaunay orbital elements space, differential of each Delaunay orbital elements is taken with respect to Keplerian orbital elements.

$$J_{\text{koe-dlly}} = \begin{bmatrix} \frac{\partial L}{\partial a} & \frac{\partial L}{\partial e} & \frac{\partial L}{\partial i} & \frac{\partial L}{\partial \omega} & \frac{\partial L}{\partial \Omega} & \frac{\partial L}{\partial M} \\ \frac{\partial l}{\partial a} & \frac{\partial l}{\partial e} & \frac{\partial l}{\partial i} & \frac{\partial l}{\partial \omega} & \frac{\partial l}{\partial \Omega} & \frac{\partial l}{\partial M} \\ \frac{\partial G}{\partial a} & \frac{\partial G}{\partial e} & \frac{\partial G}{\partial i} & \frac{\partial G}{\partial \omega} & \frac{\partial G}{\partial \Omega} & \frac{\partial G}{\partial M} \\ \frac{\partial g}{\partial a} & \frac{\partial g}{\partial e} & \frac{\partial g}{\partial i} & \frac{\partial g}{\partial \omega} & \frac{\partial g}{\partial \Omega} & \frac{\partial g}{\partial M} \\ \frac{\partial H}{\partial a} & \frac{\partial H}{\partial e} & \frac{\partial H}{\partial i} & \frac{\partial H}{\partial \omega} & \frac{\partial H}{\partial \Omega} & \frac{\partial H}{\partial M} \\ \frac{\partial h}{\partial a} & \frac{\partial h}{\partial e} & \frac{\partial h}{\partial i} & \frac{\partial h}{\partial \omega} & \frac{\partial h}{\partial \Omega} & \frac{\partial h}{\partial M} \end{bmatrix} \quad (4.20)$$

Value of each differential is as follows:

$$J_{\text{koe-dlly}} = \begin{bmatrix} \frac{1}{2} \sqrt{\frac{\mu}{a}} & 0 & 0 & 0 & 0 & 0 & 0 \\ 0 & 0 & 0 & 0 & 0 & 0 & 1 \\ \frac{1}{2} \sqrt{\frac{\mu(1-e^2)}{a}} & -e \sqrt{\frac{\mu a}{(1-e^2)}} & 0 & 0 & 0 & 0 & 0 \\ 0 & 0 & 0 & 1 & 0 & 0 & 0 \\ \frac{1}{2\sqrt{a}} \sqrt{\mu(1-e^2)} \cos i & -\sqrt{\frac{\mu a}{1-e^2}} e \cos i & -\sqrt{\mu(1-e^2)a} \sin i & 0 & 0 & 0 & 0 \\ 0 & 0 & 0 & 0 & 1 & 0 & 0 \end{bmatrix} \quad (4.21)$$

The covariance matrix thus in Delaunay orbital elements is given as

$$P_{\text{dlly}} = J_{\text{koe-dlly}}(P_{\text{koe}})J_{\text{koe-dlly}}^T \quad (4.22)$$

## 5. ADMISSIBLE REGION

To find out the complete orbit for any space debris, it is required to solve a system of equations with six unknowns. A major challenge arising in finding these unknowns for orbit determination is to correlate two or more TSAs belonging to the same physical object. In the case of having just a single TSA (angle and angle rates  $(\alpha, \dot{\alpha}, \delta, \dot{\delta})$ ), probabilistic method of determining the region of possible ranges and range-rates  $(\rho, \dot{\rho})$  for an optical attributable can be employed. This region can be obtained by imposing constraints on range and range-rate under certain premise and is called Admissible Region (refer [2], [7], [3], [17]). An optical attributable vector  $(\alpha, \delta, \dot{\alpha}, \dot{\delta})$  consists of angular coordinates and their rate of change with respect to time.  $\alpha$  is the right ascension,  $\delta$  is the declination,  $\dot{\alpha}$  is the rate of change of right ascension with time and  $\dot{\delta}$  is the rate of change of declination with time in the Topocentric Equatorial reference system. The values of range  $\rho$  and range-rate  $\dot{\rho}$  are not measured.

$$A_{opt} = (\alpha, \delta, \dot{\alpha}, \dot{\delta}) \in [-\pi, \pi) \times (-\pi/2, \pi/2) \times \mathbb{R}^2 \quad [3] \quad (5.1)$$

### 5.1 With Energy Constraint

For Earth orbiting objects, the two-body internal energy is given by

$$\varepsilon = \frac{\|\dot{\mathbf{r}}\|^2}{2} - \frac{\mu}{\|\mathbf{r}\|} \quad (5.2)$$

where  $\mu$  is the gravitational parameter of the central body,  $\mathbf{r}$  is the inertial position of the object with respect to the Earth center (ECI-Earth centered inertial frame), and  $\dot{\mathbf{r}}$  is the inertial velocity of the object in ECI.

Since the optical observation is done from a ground station, the position of the object with respect to the Earth center is given as the sum of the position of the ground station and the position of the object with respect to the station, and likewise for the velocities:

$$\mathbf{r} = \mathbf{R} + \boldsymbol{\rho} \quad \text{and} \quad \dot{\mathbf{r}} = \dot{\mathbf{R}} + \dot{\boldsymbol{\rho}} \quad (5.3)$$

where  $\mathbf{R}$  is the inertial position of the ground station,  $\dot{\mathbf{R}}$  is the inertial velocity of the ground station,  $\boldsymbol{\rho}$  is the topocentric position of the object with respect to the station, and  $\dot{\boldsymbol{\rho}}$  is the velocity of the object with respect to the station, both in Topocentric Equatorial system.

The position and the velocity of object with respect to the station given in the spherical coordinates of range,  $\rho$ , right ascension,  $\alpha$ , declination,  $\delta$ , and their rates with respect to time are

$$\boldsymbol{\rho} = \rho \mathbf{u}_\rho \quad \text{and} \quad \dot{\boldsymbol{\rho}} = \dot{\rho} \mathbf{u}_\rho + \rho \dot{\alpha} \mathbf{u}_\alpha + \rho \dot{\delta} \mathbf{u}_\delta \quad (5.4)$$

where the vectors  $\mathbf{u}_\rho$ ,  $\mathbf{u}_\alpha$ , and  $\mathbf{u}_\delta$  are given by

$$\mathbf{u}_\rho = \begin{bmatrix} \cos \alpha \cos \delta \\ \sin \alpha \cos \delta \\ \sin \delta \end{bmatrix}, \quad \mathbf{u}_\alpha = \begin{bmatrix} -\sin \alpha \cos \delta \\ \cos \alpha \cos \delta \\ 0 \end{bmatrix}, \quad \mathbf{u}_\delta = \begin{bmatrix} \cos \alpha \sin \delta \\ -\sin \alpha \sin \delta \\ \cos \delta \end{bmatrix} \quad (5.5)$$

As part of the attributable, the right ascension and the declination are known from the optical measurement. This means that the vectors  $\mathbf{u}_\rho$ ,  $\mathbf{u}_\alpha$  and  $\mathbf{u}_\delta$  can be computed; however, the range or the range-rate are still unknown. To proceed further, few scalar values are defined as

$$\begin{aligned} w_0 &= \|\mathbf{R}\|^2, & w_1 &= 2(\dot{\mathbf{R}} \cdot \mathbf{u}_\rho), & w_2 &= \dot{\alpha}^2 \cos^2 \delta + \dot{\delta}^2 \\ w_3 &= 2\dot{\alpha}(\dot{\mathbf{R}} \cdot \mathbf{u}_\alpha) + 2\dot{\delta}(\dot{\mathbf{R}} \cdot \mathbf{u}_\delta), & w_4 &= \|\dot{\mathbf{R}}\|^2, & w_5 &= 2(\dot{\mathbf{R}} \cdot \mathbf{u}_\rho) \end{aligned} \quad (5.6)$$



With these scalar values, the squared Euclidean norms of the position and velocity of the object with respect to the Earth center can be written as

$$\begin{aligned}\|\mathbf{r}\|^2 &= \rho^2 + w_5\rho + w_0 \\ \|\dot{\mathbf{r}}\|^2 &= \dot{\rho}^2 + w_1\dot{\rho} + w_2\rho^2 + w_3\rho + w_4\end{aligned}$$

Substituting the squared norms of the position and velocity into the two-body energy equation, it follows that twice the energy can be expressed as

$$2\varepsilon = \dot{\rho}^2 + w_1\dot{\rho} + F(\rho) \quad (5.7)$$

where

$$F(\rho) = w_2\rho^2 + w_3\rho + w_4 - \frac{2\mu}{\sqrt{\rho^2 + w_5\rho + w_0}} \quad (5.8)$$

The energy equation can be rewritten in standard quadratic form by subtracting  $2\varepsilon$  from both sides, such that

$$\dot{\rho}^2 + w_1\dot{\rho} + F(\rho) - 2\varepsilon = 0 \quad (5.9)$$

Therefore, given a value of  $\rho$ , the preceding equation for  $\dot{\rho}$  can be solved yielding two solutions as

$$\dot{\rho} = -\frac{w_1}{2} \pm \sqrt{\left(\frac{w_1}{2}\right)^2 - F(\rho) + 2\varepsilon} \quad (5.10)$$

If  $\varepsilon = 0$  (equation 5.2) is specified, the zero-energy curve can be obtained. Since all Earth-orbiting objects must have negative orbital energy, the zero-energy curve in range range-rate space describes the region of all locations of range and range-rate that, when paired with the measurements of the right ascension, declination, and their rates, leads to orbits bound to the Earth.

## 5.2 With Semimajor Axis And Eccentricity Constraint [14]

It is sometimes desired to add constraints to the Admissible Region in order to reduce the possible combinations of range range-rate pairs that lead to permissible orbit solutions. A wide variety of constraints can be considered, such as minimum periapse altitude or minimum range. Constraints on the semi-major axis of the orbit and constraints on the eccentricity of the orbit are discussed here.

The first constraint discussed here is the constraint on the semi-major axis, or equivalently energy since the two are related by

$$\varepsilon = -\frac{\mu}{2a} \quad (5.11)$$

where  $a$  is the semi-major axis. By setting a value for the semi-major axis, an equivalent energy value may be determined. Then, by using this value of energy, the admissible region procedure may be used to solve for range-rate given range values, which yields a curve of the constant semi-major axis in the range range-rate space.

To develop the eccentricity constraint, the specific angular momentum is as

$$\mathbf{h} = -\mathbf{r} \times \dot{\mathbf{r}} \quad (5.12)$$

Some vector parameters used later are defined as

$$\begin{aligned} h_1 &= \mathbf{R} \times \mathbf{u}_\rho, & h_2 &= \mathbf{u}_\rho \times (\dot{\alpha}\mathbf{u}_\alpha + \dot{\delta}\mathbf{u}_\delta), \\ h_3 &= \mathbf{u}_\rho \times \dot{\mathbf{R}} + \mathbf{R} \times (\dot{\alpha}\mathbf{u}_\alpha + \dot{\delta}\mathbf{u}_\delta), & h_4 &= \mathbf{R} \times \dot{\mathbf{R}} \end{aligned} \quad (5.13)$$

Next, a set of scalar parameters are defined as

$$\begin{aligned} c_0 &= \|\mathbf{h}_1\|^2, & c_1 &= 2\mathbf{h}_1 \cdot \mathbf{h}_2, & c_2 &= 2\mathbf{h}_1 \cdot \mathbf{h}_3, & c_3 &= 2\mathbf{h}_1 \cdot \mathbf{h}_4, & c_4 &= \|\mathbf{h}_2\|^2, \\ c_5 &= 2\mathbf{h}_2 \cdot \mathbf{h}_3, & c_6 &= 2\mathbf{h}_2 \cdot \mathbf{h}_4 + \|\mathbf{h}_3\|^2, & c_7 &= 2\mathbf{h}_3 \cdot \mathbf{h}_4, & c_8 &= \|\mathbf{h}_4\|^2 \end{aligned} \quad (5.14)$$

With these scalar parameters, it is possible to show that the squared Euclidean norm of the specific angular momentum is given by

$$\| \mathbf{h} \|^2 = c_0 \dot{\rho}^2 + P(\rho) \dot{\rho} + U(\rho) \quad (5.15)$$

where

$$\begin{aligned} P(\rho) &= c_1 \rho^2 + c_2 \rho + c_3 \\ U(\rho) &= c_4 \rho^4 + c_5 \rho^3 + c_6 \rho^2 + c_7 \rho + c_8 \end{aligned} \quad (5.16)$$

The eccentricity is related to both the specific angular momentum and specific energy by

$$e = \sqrt{1 + \frac{2\varepsilon \|\mathbf{h}\|^2}{\mu^2}} \quad (5.17)$$

which may be rearranged as

$$\varepsilon \|\mathbf{h}\|^2 = -\mu^2 (1 - e^2) \quad (5.18)$$

On substituting values of  $2\varepsilon$  and  $\|\mathbf{h}\|^2$ , it follows that

$$(\dot{\rho}^2 + w_1 \dot{\rho} + F(\rho))(c_0 \dot{\rho}^2 + P(\rho) \dot{\rho} + U(\rho)) = -\mu^2 (1 - e^2) \quad (5.19)$$

which may be rewritten as

$$a_4 \dot{\rho}^4 + a_3 \dot{\rho}^3 + a_2 \dot{\rho}^2 + a_1 \dot{\rho} + a_0 = 0 \quad (5.20)$$

where,

$$\begin{aligned} a_4 &= c_0, \quad a_3 = P(\rho) + c_0 w_1, \quad a_2 = U(\rho) + c_0 F(\rho) + w_1 P(\rho), \\ a_1 &= F(\rho) P(\rho) + w_1 U(\rho), \quad \text{and} \quad a_0 = F(\rho) U(\rho) + \mu^2 (1 - e^2) \end{aligned} \quad (5.21)$$

Given a value of eccentricity, a curve of constant eccentricity may be determined by solving for the roots of the quartic equation that have been developed above, where the equation is quartic in  $\dot{\rho}$  given a value of  $\rho$ . Solving for the roots of a quartic, four solutions will be obtained. Any imaginary solutions in the result are discarded and only the real solutions are considered when determining the curve of constant eccentricity.

### 5.3 Example Of An Admissible Region

To illustrate the determination of the Admissible Region, the object with following geocentric position and velocity is considered.

$$\mathbf{r} = 1.0e + 04 \begin{bmatrix} -3.5594 \\ 2.2557 \\ 0.0716 \end{bmatrix} \text{ km}, \quad \mathbf{v} = \begin{bmatrix} -1.6466 \\ -2.5981 \\ 0.0111 \end{bmatrix} \text{ km/s} \quad (5.22)$$

Given the geocentric position and velocity of the object and of the topocenter, topocentric angles ( $\alpha$ ,  $\delta$ ,  $\dot{\alpha}$  and  $\dot{\delta}$ ) can be found out using given equations.

$$\mathbf{u}_\rho = \begin{bmatrix} \cos \alpha \cos \delta \\ \sin \alpha \cos \delta \\ \sin \delta \end{bmatrix}, \quad (5.23)$$

$$\begin{aligned} \dot{\boldsymbol{\rho}} &= \dot{\rho} \mathbf{u}_\rho + \rho \dot{\alpha} \mathbf{u}_\alpha + \rho \dot{\delta} \mathbf{u}_\delta \\ \dot{\boldsymbol{\rho}} &= \begin{bmatrix} \dot{\rho} \cos \alpha \cos \delta - \rho \cos \alpha \sin \delta \dot{\delta} - \rho \sin \alpha \cos \delta \dot{\alpha} \\ \dot{\rho} \sin \alpha \cos \delta + \rho \cos \alpha \cos \delta \dot{\alpha} - \rho \sin \alpha \sin \delta \dot{\delta} \\ \dot{\rho} \sin \delta + \rho \cos \delta \dot{\delta} \end{bmatrix} \end{aligned} \quad (5.24)$$

In this example, the inertial position of the ground station can be calculated from the following equations. The geocentric latitude and longitude of the observer are taken

to be  $0.01259^\circ$  North and  $127^\circ$  West respectively. To account for the non-spherical shape of the Earth, both latitude and radius of Earth can be corrected.

$$\begin{aligned}\phi &= \phi' - 0.1924^\circ \sin(2\phi') \\ R &\approx 6378.14\text{km} - 21.38\text{km} \sin^2(2\phi')\end{aligned}\tag{5.25}$$

where  $\theta$  is the sidereal time of the observer and  $\phi$  is the apparent geographic latitude of the observer.

Radius and velocity of topocenter can be calculated as

$$\mathbf{R}_{topo} = \begin{bmatrix} R \cos \phi \cos \theta \\ R \sin \phi \cos \theta \\ R \sin \phi \end{bmatrix}\tag{5.26}$$

The Admissible Region is determined by setting  $\varepsilon = 0$  and solving for range-rate  $\dot{\rho}$  given values of the range,  $\rho$ . Figure 5.1 and 5.2 given below represent the Admissible Region with and without putting eccentricity constraint, respectively.

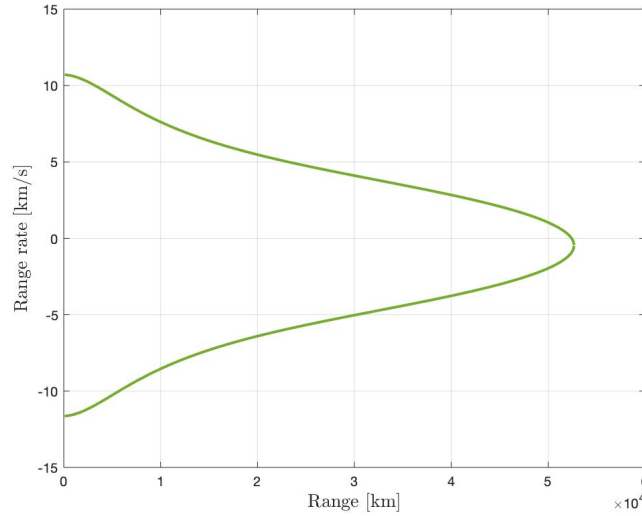


Fig. 5.1.: Region of admissible range/range-rate values given angle and angle rate data

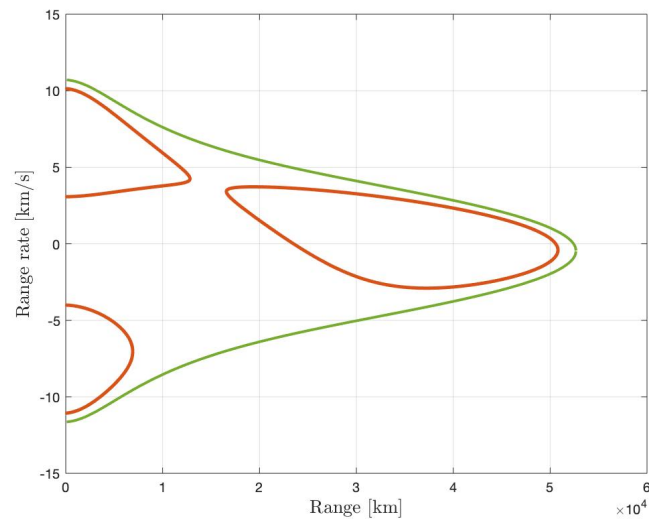


Fig. 5.2.: Region of admissible range/range-rate values given angle and angle rate data and eccentricity as 0.8

## 6. APPROXIMATING THE ADMISSIBLE REGION USING GAUSSIAN MIXTURE MODEL

In an Admissible Region, no single combination of range and range-rate is more likely than any other. Therefore, the Admissible Region can be interpreted probabilistically as describing a uniform distribution with the support defined by the boundaries of the (constrained) Admissible Region. To use a closed-form expression, a method for describing a uniform distribution via a Gaussian Mixture Model is now developed [14]. First, the problem of approximating a univariate uniform distribution is discussed, followed by generating a bivariate Gaussian mixture approximation of the Admissible Region.

A uniform distribution is given by

$$p(x) = \begin{cases} \frac{1}{b-a}, & a \leq x \leq b \\ 0, & \text{otherwise.} \end{cases} \quad (6.1)$$

and a Gaussian mixture PDF is given by

$$q(x) = \sum_{l=1}^L \alpha_l p_g(x; m_l, P_l) \quad (6.2)$$

where  $p_g(x; a; A)$  represents a Gaussian PDF for the variable  $x$  with mean  $a$  and covariance  $A$ ; that is,

$$p_g(x; a; A) = |2\pi A|^{-1/2} \exp -\frac{1}{2}(x - a)^T A^{-1}(x - a) \quad (6.3)$$

To approximate a uniform distribution using a Gaussian distribution, the distance between  $p(x)$  and  $q(x)$  is taken as the  $L_2$  norm via

$$L_2[p \parallel q] = \int_R (p(x) - q(x))^2 dx \quad (6.4)$$

The minimum distance  $L_2$  is considered along with given constraints to determine the weights, means, and variances of the components in the Gaussian mixture approximation. The  $L_2$  distance between the uniform and Gaussian mixture PDFs [25] can be simplified to get a closed-form equation

$$L_2[p \parallel q] = \frac{1}{b-a} + \sum_{i=1}^L \sum_{j=1}^L \alpha_i \alpha_j \Gamma(m_i, m_j, P_i, P_j) - \frac{1}{b-a} \sum_{l=1}^L \left[ \operatorname{erf} \left\{ \frac{b-m_l}{\sqrt{2P_l}} \right\} - \operatorname{erf} \left\{ \frac{a-m_l}{\sqrt{2P_l}} \right\} \right] \quad (6.5)$$

where

$$\Gamma(m_i, m_j, P_i, P_j) = |2\pi(P_i + P_j)^{-\frac{1}{2}}| \exp \left( \frac{-1}{2} (m_i - m_j)^T (P_i + P_j)^{-1} (m_i - m_j) \right) \quad (6.6)$$

where  $\operatorname{erf}$  is the error function. The optimization problem in the given equation is ill-conditioned due to a large number of local minima. To help reduce the number of parameters and create a better-conditioned optimization problem, the following are assumed:

- The weights are equal for all components.
- The means are evenly distributed across the support of  $p(x)$ .
- The Gaussian mixture is homoscedastic.



Taking the preceding assumptions  $L_2$  distance reduces to

$$L_2[p \parallel q] = \frac{1}{b-a} + \frac{\alpha^2}{2\sqrt{\pi}\sigma} \sum_{i=1}^L \sum_{j=1}^L \exp \left\{ \frac{-1}{4} \left( \frac{m_i - m_j}{\sigma} \right)^2 \right\} - \frac{\alpha}{b-a} \sum_{l=1}^L [\operatorname{erf}\{B_l\} - \operatorname{erf}\{A_l\}] \quad (6.7)$$

where

$$A_l = \left( \frac{a - m_l}{\sqrt{2}\sigma} \right) \quad \text{and} \quad B_l = \left( \frac{b - m_l}{\sqrt{2}\sigma} \right)$$

This equation requires optimization over only the standard deviation parameter. To find the solution, the derivative of  $L_2$  distance with respect to the standard deviation parameter is found out. If the second derivative is found to be positive, then the optimal solution is confirmed. Specifying the number of components  $L$ , a library of solutions (i.e., an optimized value of  $\sigma$  given a number of components  $L$ ) can be generated. Without loss of generality, the parameters of the univariate uniform PDF are taken as  $a = 0$  and  $b = 1$ . Therefore, means and weights can be summarized as follows

$$\tilde{\alpha}_l = \frac{1}{L} \quad \text{and} \quad \tilde{m}_l = \frac{l}{L+1} \quad \forall \quad l \in \{1, 2, \dots, L\} \quad (6.8)$$

Using the above equations for mean, weight and  $L_2$  norm, the optimal value of  $\tilde{\sigma}$  can be obtained, given the value of  $L$ . The following table shows the value of  $\tilde{\sigma}$  corresponding to a particular value of  $L$ .

## 6.1 Application To The Admissible Region

The Admissible Region obtained in the previous section represents a uniform PDF in two dimensions. To approximate the Admissible Region with a Gaussian mixture, range and range-rate distributions are approximated separately into two one-dimensional approximations. Following steps are followed to obtain a univariate

Gaussian Mixture Model from a uniform distribution and the same steps can be extended to get a bivariate Gaussian Mixture Model.

- Finding out the range marginal PDF
- Finding out the number of components by defining the maximum value of sigma for range and range-rate
- Finding out the weights since range values do not give a uniform distribution with equal weights
- Finding out the mean and covariance corresponding to each component

## 6.2 Approximating Univariate GMM For Range

If  $p_{\rho,\dot{\rho}}(\rho, \dot{\rho})$  represents the total uniform PDF of the Admissible Region, then

$$p_{\rho}(\rho) = \int_{-\infty}^{\infty} p_{\rho,\dot{\rho}}(\rho, \nu) d\nu \quad (6.9)$$

is the range-marginal PDF. To obtain the range marginal PDF, firstly the whole area under the Admissible Region is calculated using Simpson's rule. Every alternate value of range in the range array is used to find the area within those limits which are then added to get the total area. The formula for the integrated area by Simpson's rule is given by

$$\begin{aligned} I &= \frac{h}{3}(f(i) + 4f(i+1) + f(i+2)) \\ h &= \frac{b-a}{n} \end{aligned} \quad (6.10)$$

where n= number of intervals. Using the total area, the uniform probability density can be found out and then multiplied by the difference in range-rates at each range to get range marginal probability density function. To find out the number of components from pre-computed libraries, a maximum standard deviation for the range

direction,  $\sigma_{\rho, max}$  is specified and the smallest number of components that satisfies this condition is taken.

The parameters of the GMM approximation after finding out the number of components and hence  $\tilde{\sigma}$  are

$$\begin{aligned}\alpha_l &= \frac{1}{L}, & m_l &= a + \frac{(b-a)l}{L+1} \\ P_l &= ((b-a)\tilde{\sigma})^2 \quad \forall \quad l \in \{1, 2, \dots, L\}\end{aligned}\tag{6.11}$$

These parameters produce the Gaussian Mixture Model for a uniform distribution but range marginal PDF is not represented as a uniform distribution. To account for the non-uniform nature of range marginal PDF, the weights of GMM PDF are found by solving the least-squares problem. If the weights are concatenated into a vector  $\alpha$ , the L-component GMM PDF may be expressed as

$$\begin{aligned}q(x) &= \mathbf{h}^T(x)\boldsymbol{\alpha} \\ h_l(x) &= p_g(x; m_l, P_l)\end{aligned}\tag{6.12}$$

where  $\boldsymbol{\alpha} \in \mathbb{R}^L$  and  $h(x) \in \mathbb{R}^L$ . Taking M values of the range, range marginal PDF is evaluated at each value of the range. These values are then collected in a vector  $\mathbf{p}$ . Then, the weights of GMM PDF are found by solving the following equations subjected to linear equality/inequality constraints:

$$\min J = \|\mathbf{p} - \mathbf{H}\boldsymbol{\alpha}\| \quad \text{subject to} \quad \boldsymbol{\alpha} \geq 0 \quad \text{and} \quad \mathbf{1}^T \boldsymbol{\alpha} = 1 \tag{6.13}$$

where  $\mathbf{1} \in \mathbb{R}^L$  is a vector of ones, and  $H \in \mathbb{R}^{M \times L}$  with the element in the  $i$ th row and  $l$ th column given by

$$H_{i,l} = p_g(\rho_i; m_l, P_l) \tag{6.14}$$

These weights obtained after solving the least-squares problem when combined along with means and covariances produce a GMM approximation of the range

marginal PDF. This process of obtaining a GMM approximation to the range marginal PDF is illustrated in figure 6.1.

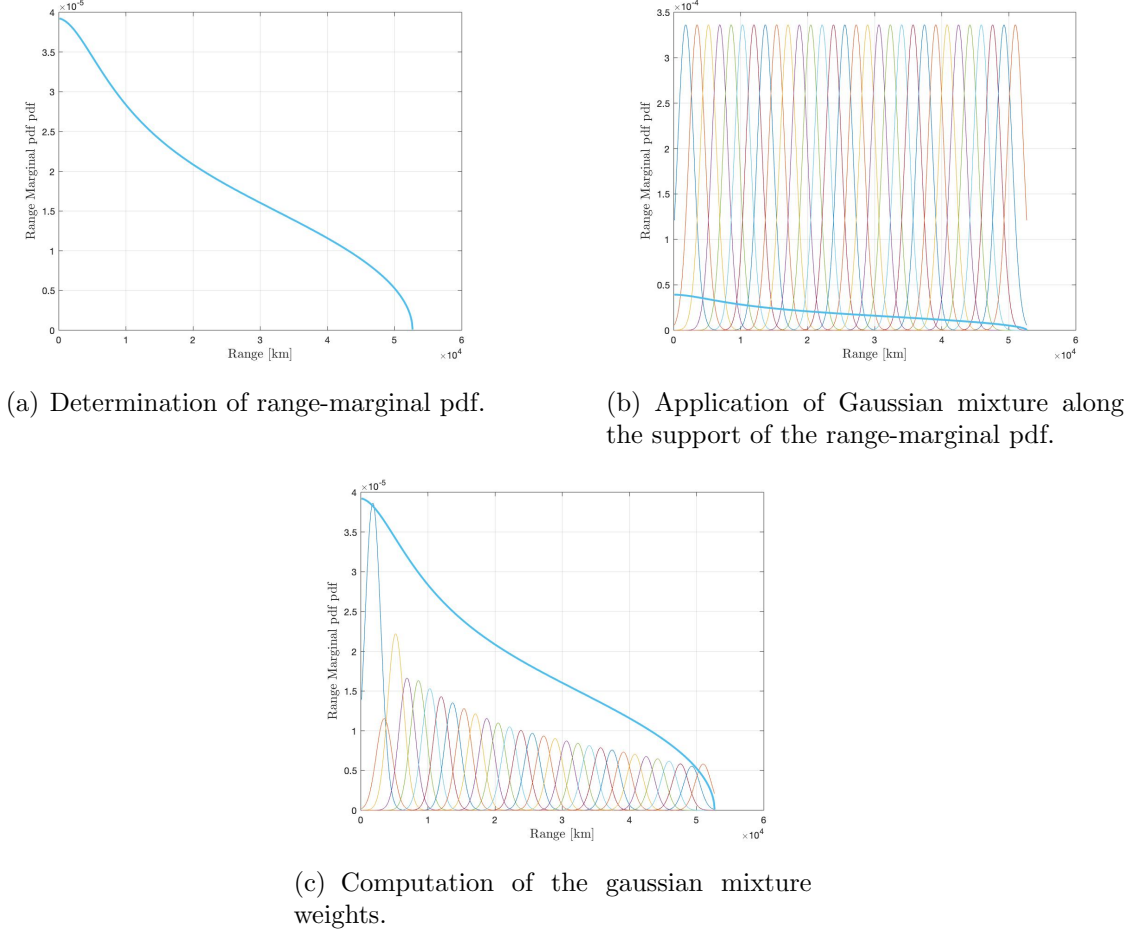


Fig. 6.1.: Illustration of the process for computing a Gaussian mixture approximation of the range-marginal PDF

### 6.3 Approximating Bivariate GMM For Range-Rate

As discussed earlier, GMM PDF approximation of the Admissible Region involves approximating range-marginal PDF and range-rate marginal PDF separately. To approximate in range-rate direction, consider a single component of the range-marginal GMM approximation. Given a value of range, no associated value of range-rate within the constrained Admissible Region is more or less likely. Therefore, the idea behind

extending the range-marginal GMM PDF to the constrained Admissible Region is to apply the previously discussed GMM approximation of the uniform PDF to the range-rate direction for each component of the range-marginal GMM approximation to develop a bivariate GMM PDF that describes the constrained Admissible Region.

A GMM approximation of the range-marginal PDF can be renamed as

$$p_\rho(\rho) \approx \sum_{l=1}^{L_\rho} \alpha_{\rho,l} p_g(\rho; m_{\rho,l}, P_{\rho,l}) \quad (6.15)$$

For each component in range, the associated range-rate values represent a uniform distribution. To determine the number of components in range-rate corresponding to the each component in range, the extremal range-rate values are computed at each range value that is dictated by the means of the range-marginal GMM.

$$a_l = \arg_{\dot{\rho}} \min p_{\rho,\dot{\rho}}(m_{\rho,l}, \dot{\rho}) \quad (6.16)$$

and

$$b_l = \arg_{\dot{\rho}} \max p_{\rho,\dot{\rho}}(m_{\rho,l}, \dot{\rho}) \quad (6.17)$$

The distance between these extremal values ( $\Delta_l = (b_l - a_l)$ ) along with predefined sigma max for range-rate gives the  $\tilde{\sigma}$ ,  $\tilde{\sigma}\Delta_l \leq \sigma_{\dot{\rho},max}$ , which can be subsequently used to find out the  $L_{\dot{\rho},l}$  from predefined libraries. Then, the total number of components of the bivariate GMM approximation of the constrained Admissible Region is given by  $L = \sum_{l=1}^{L_\rho} L_{\dot{\rho},l}$ .

After finding the number of components for range-rate direction, the GMM parameters for range-rate are as follows

$$\begin{aligned} \alpha_{\dot{\rho},k} &= \frac{1}{L_{\dot{\rho},l}}, & m_{\dot{\rho},k} &= a_l + \frac{\Delta_l k}{L_{\dot{\rho},l} + 1} \\ P_l &= (\Delta_l \tilde{\sigma})^2 \quad \forall \quad k \in \{1, 2, \dots, L_{\dot{\rho},l}\} \end{aligned} \quad (6.18)$$

Given the parameters of the  $l$ th component of the range-marginal GMM approximation and the  $k$ -associated components of the range-rate GMM approximation, the corresponding components of the bivariate GMM approximation of the constrained Admissible Region are

$$\alpha_{\rho,\dot{\rho},i_{l+k}} = \alpha_{\rho,l}\alpha_{\dot{\rho},k}, \quad m_{\rho,\dot{\rho},i_{l+k}} = \begin{bmatrix} m_{\rho,l} \\ m_{\dot{\rho},k} \end{bmatrix} \quad (6.19)$$

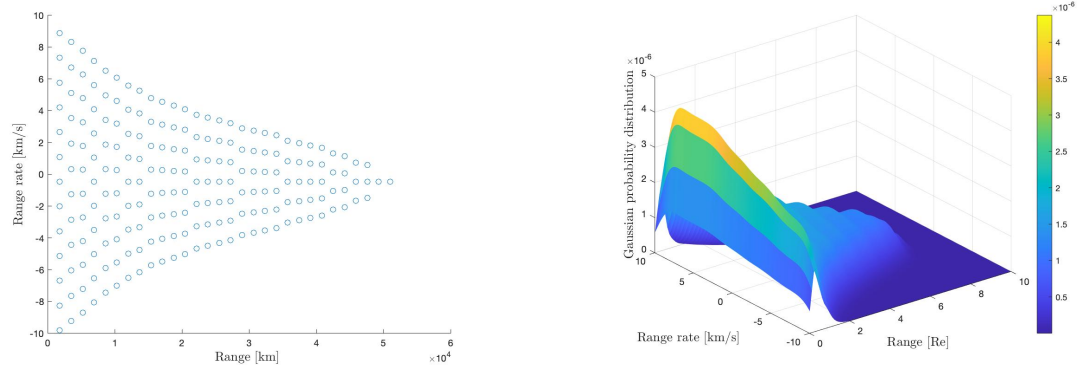
$$P_{\rho,\dot{\rho},i_{l+k}} = \begin{bmatrix} P_{\rho,l} & 0 \\ 0 & P_{\dot{\rho},k} \end{bmatrix} \quad \text{where } k \in \{1, 2, \dots, L_{\dot{\rho},l}\}$$

To approximate the whole of the Admissible Region, this procedure can be repeated for each of the component in the range marginal PDF and this can be summarized by the following equation.

$$p_{\rho,\dot{\rho}}(\rho, \dot{\rho}) \approx \sum_{l=1}^L \alpha_{\rho,\dot{\rho},i} p_g(\rho, \dot{\rho}; \mathbf{m}_{\rho\dot{\rho},i}, \mathbf{P}_{\rho\dot{\rho},i}) \quad (6.20)$$

The GMM approximation of the Admissible Region is illustrated in figure 6.2 for energy = 0 constraint. Figure (a) shows the location of mean associated with each component in range range-rate space. Y axis denotes the range-rate values and x axis denotes range values. Figure (b) shows the probability distribution of Gaussian Mixture Model. The GMM is a bivariate distribution with x axis showing range values, y axis showing range range-rate values and z axis showing Gaussian probability. On comparing this plot with figure 5.1, it is clear that the approximation is not uniform. More number of components can be taken to get a better approximation. In this thesis, about 800 components are used for creating the GMM.

The GMM approximation of the Admissible Region is illustrated in the figure 6.3 for eccentricity less than 0.8 constraint. The components more than 0.8 eccentricity have been eliminated and is demonstrated in figure (a) and (b).

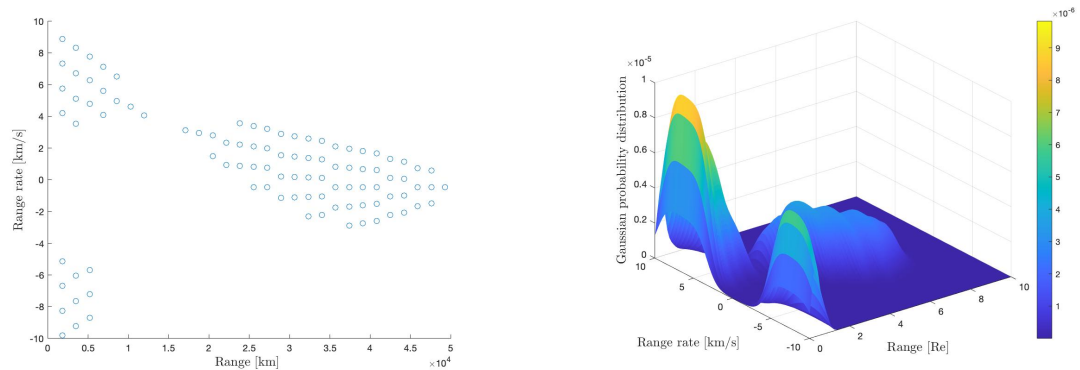


(a) Location of Gaussian mixture components.

(b) Surface plot of the Gaussian mixture.

Fig. 6.2.: Gaussian mixture representation of the constrained Admissible Region with 206 components

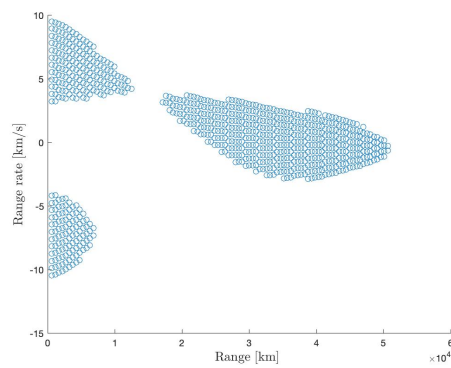
The GMM approximation of the Admissible Region with eccentricity less than 0.8 constraint is illustrated in the figure 6.3. Figure 6.4 shows the plot with 807 no of components with eccentricity constraint.



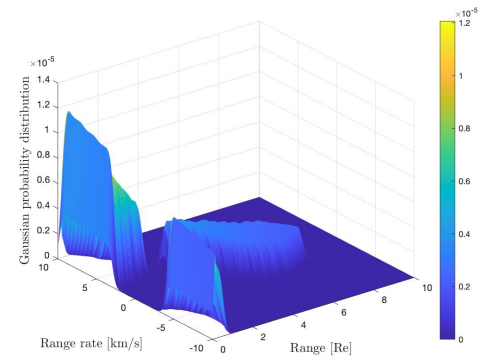
(a) Location of Gaussian mixture components.

(b) Surface plot of the Gaussian mixture.

Fig. 6.3.: Gaussian mixture representation of the constrained Admissible Region with 97 components



(a) Location of Gaussian mixture components.



(b) Surface plot of the Gaussian mixture.

Fig. 6.4.: Gaussian mixture representation of the constrained Admissible Region with 807 components



## 7. FILTERING TECHNIQUES

Filtering technique is used for the propagation of state and uncertainty of the target to get the GMM at time  $t_2$ . The filtering techniques discussed here are Kalman filter and Extended Kalman filter. They work on the principle of minimizing the mean square error estimation [17].

### 7.1 Kalman Filter

A Kalman filter [15] is a computer algorithm that is used to process error corrupted measurement data. The purpose of the processing is to better determine the parameters or variables associated with the process that generates the measurements [17]. Using the Kalman filter, one can determine the state vector of the target and also find out the uncertainty associated with that state. These filters have a wide range of application, for example, in navigation, in determining the irregularities in Earth's gravity field, and in determining the state of a chemical process.

While using the Kalman filter, the aim is to determine two things based on observations and a prior:

- An estimate  $x_{k|k}$  of the state vector of the target
- An estimate of the likely error associated with  $x_{k|k}$

The state vector contains the information about the target (e.g position and velocity) and the measure of the error in state vector is the error covariance matrix  $P_{k|k}$  [26]. There are three main steps for Kalman filter:

### 7.1.1 Kalman Filter Initialization

This step is basically to choose a good initial guess for the Kalman filter. An initial guess includes an initial state vector and an uncertainty (covariance matrix) associated with the target. If  $x_0$  and  $P_0$  are chosen poorly then the Kalman filter will not be able to acquire the target and will diverge. Initial conditions can be given as

$$\begin{aligned}\mathbf{m}_0 &= E\{\mathbf{x}(t_0)\} \\ \mathbf{P}_0 &= E\{(\mathbf{x}(t_0) - \mathbf{m}_0)(\mathbf{x}(t_0) - \mathbf{m}_0)^T\}\end{aligned}\tag{7.1}$$

Here,  $\mathbf{m}_0 = \mathbf{m}(t_0)$  is mean of the initial state and  $\mathbf{P}_0 = \mathbf{P}(t_0)$  is the covariance matrix at initial time.

### 7.1.2 Kalman Filter Prediction

This step means predicting the state of the target at a given time. The deterministic model states that the target will have state  $x_{k+1}$  at time step  $k+1$  if it had state  $x$  at time step  $k$ , where matrix  $\mathbf{F}(t)$  is called the state transition matrix. Since actual target motion is also perturbed, there is another quantity added to the equation which is nothing but the white noise providing stochastic excitation to the deterministic dynamics. The system and the measurement model dynamics is thus given by

$$\begin{aligned}\dot{\mathbf{x}}(t) &= \mathbf{F}(t)\mathbf{x}(t) + \mathbf{M}(t)\mathbf{w}(t) \\ \mathbf{z}_k &= \mathbf{H}_k\mathbf{x}_k + \mathbf{L}_k\mathbf{v}_k\end{aligned}\tag{7.2}$$

Here,  $\mathbf{w}(t)$  is white noise and  $\mathbf{M}(t)$  is a shape matrix that maps the noise into the dynamics. The measurement noise is represented by  $\mathbf{v}_k$ , which is assumed to be a zero-mean white-noise sequence with covariance  $\mathbf{R}_k$ .

Mean and covariance can be propagated using the following equations

$$\begin{aligned}\dot{\mathbf{m}}(t) &= \mathbf{F}(t)\mathbf{m}(t) \\ \dot{\mathbf{P}}(t) &= \mathbf{F}(t)\mathbf{P}(t) + \mathbf{P}(t)\mathbf{F}^T(t) + \mathbf{M}(t)\mathbf{Q}_s(t)\mathbf{M}^T(t)\end{aligned}\tag{7.3}$$

Here,  $\mathbf{Q}_s(t)$  is power spectral density and is constant for white-noise processes.

### 7.1.3 Kalman Filter Update

After getting the state at time step  $k+1$ , correction of this predicted state is performed by using the actual observation at time  $k+1$  which is given in the following equations

$$\begin{aligned}\hat{\mathbf{z}}_k &= \mathbf{H}_k\mathbf{m}_k^- \\ \mathbf{W}_k &= \mathbf{H}_k\mathbf{P}_k^-\mathbf{H}_k^T + \mathbf{L}_k\mathbf{R}_k\mathbf{L}_k^T \\ \mathbf{C}_k &= \mathbf{P}_k^-\mathbf{H}_k \\ \mathbf{K}_k &= \mathbf{C}_k\mathbf{W}_k^{-1} \\ \mathbf{m}_k^+ &= \mathbf{m}_k^- + \mathbf{K}_k(\mathbf{z}_k - \hat{\mathbf{z}}_k) \\ \mathbf{P}_k^+ &= \mathbf{P}_k^- - \mathbf{C}_k\mathbf{K}_k^T - \mathbf{K}_k\mathbf{C}_k^T + \mathbf{K}_k\mathbf{W}_k\mathbf{K}_k^T\end{aligned}\tag{7.4}$$

Here,  $\mathbf{K}_k$  is the gain matrix,  $\mathbf{C}_k$  is the cross-covariance (with the measurement) and  $\mathbf{W}_k$  is the measurement covariance.

Some assumptions and properties associated with the Kalman filter are

- The state is not correlated with the measurement noise
- It makes no requirement that the distribution be Gaussian
- It makes no requirement that the measurement function be linear
- It works with first and second-moment statistics

- It employs a linear update law, i.e. a linear gain
- It forces an unbiased posterior estimate (can be relaxed)
- It minimizes the posterior mean square error (minimum variance)

## 7.2 Extended Kalman Filter

The main difference between the Kalman filter and the Extended Kalman filter is that the Kalman filter operates on linear dynamical systems and Extended Kalman filter operates on non-linear system dynamics, non linear measurements, or both. Examples of such non-linear system dynamics are - an object under the influence of two-body dynamics, and all objects in orbits. Often, the actual state of the object cannot be observed but quantities which are a non-linear function of state like range can be observed. Therefore, the Kalman filter is modified to handle these non-linearities. The Extended Kalman filter (EKF) handles non-linearities through the use of linearization. Similar to the Kalman filter, this filter is comprised of three steps: initiation, prediction and update.

### 7.2.1 Extended Kalman Filter Initialization

This step is the same as the Kalman filter and requires to choose a good initial guess for the Extended Kalman filter. An initial guess includes an initial state vector and an uncertainty (covariance matrix) associated with the target. If  $x_0$  and  $P_0$  are chosen poorly then the Extended Kalman filter will not be able to acquire the target and will diverge. Initial conditions can be given as

$$\begin{aligned}\mathbf{m}_0 &= E\{\mathbf{x}(t_0)\} \\ \mathbf{P}_0 &= E\{(\mathbf{x}(t_0) - \mathbf{m}_0)(\mathbf{x}(t_0) - \mathbf{m}_0)^T\}\end{aligned}\tag{7.5}$$

Here,  $\mathbf{m}_0 = \mathbf{m}(t_0)$  is mean of the initial state and  $\mathbf{P}_0 = \mathbf{P}(t_0)$  is the covariance matrix at initial time.

### 7.2.2 Extended Kalman Filter Prediction

This step means predicting/propagating the state of the target at a given time. In this case, the state follows a non-linear dynamical system model. The system and the measurement model dynamics is thus given by

$$\begin{aligned}\dot{\mathbf{x}}(t) &= \mathbf{f}(\mathbf{x}(t)) + \mathbf{M}(t)\mathbf{w}(t) \\ \mathbf{z}_k &= \mathbf{h}(\mathbf{x}_k) + \mathbf{L}_k\mathbf{v}_k\end{aligned}\tag{7.6}$$

Here,  $\mathbf{w}(t)$  is white noise and  $\mathbf{M}(t)$  is a shape matrix that maps the noise into the dynamics. The measurement noise is represented by  $\mathbf{v}_k$ , which is assumed to be a zero-mean white-noise sequence with covariance  $\mathbf{R}_k$ .

Mean and covariance can be propagated using following equations

$$\begin{aligned}\dot{\mathbf{m}}(t) &= \mathbf{f}(\mathbf{m}(t)) \\ \dot{\mathbf{P}}(t) &= \mathbf{F}(\mathbf{m}(t))\mathbf{P}(t) + \mathbf{P}(t)\mathbf{F}^T(\mathbf{m}(t)) + \mathbf{M}(t)\mathbf{Q}_s(t)\mathbf{M}^T(t)\end{aligned}\tag{7.7}$$

Here,  $\mathbf{Q}_s(t)$  is the power spectral density and is constant for white-noise processes.

### 7.2.3 Extended Kalman Filter Update

After getting the state at time step  $k+1$ , correction of this predicted state is performed by taking the actual observation at time  $k+1$  which is given in the following equations

$$\begin{aligned}
\hat{\mathbf{z}}_k &= \mathbf{h}(\mathbf{m}_k^-) \\
\mathbf{W}_k &= \mathbf{H}(\mathbf{m}_k^-) \mathbf{P}_k^- \mathbf{H}^T(\mathbf{m}_k^-) + \mathbf{L}_k \mathbf{R}_k \mathbf{L}_k^T \\
\mathbf{C}_k &= \mathbf{P}_k^- \mathbf{H}^T(\mathbf{m}_k^-) \\
\mathbf{K}_k &= \mathbf{C}_k \mathbf{W}_k^{-1} \\
\mathbf{m}_k^+ &= \mathbf{m}_k^- + \mathbf{K}_k (\mathbf{z}_k - \hat{\mathbf{z}}_k) \\
\mathbf{P}_k^+ &= \mathbf{P}_k^- - \mathbf{C}_k \mathbf{K}_k^T - \mathbf{K}_k \mathbf{C}_k^T + \mathbf{K}_k \mathbf{W}_k \mathbf{K}_k^T
\end{aligned} \tag{7.8}$$

where the dynamics jacobian,  $\mathbf{F}(\mathbf{m}(t))$  is defined as

$$\mathbf{F}(\mathbf{m}(t)) = \left[ \frac{\partial \mathbf{f}(\mathbf{x}(t))}{\partial \mathbf{x}(t)} \right]_{\mathbf{x}(t)=\mathbf{m}(t)} \tag{7.9}$$

Here,  $\mathbf{K}_k$  is the gain matrix,  $\mathbf{C}_k$  is the cross-covariance (with the measurement) and  $\mathbf{W}_k$  is the measurement covariance.

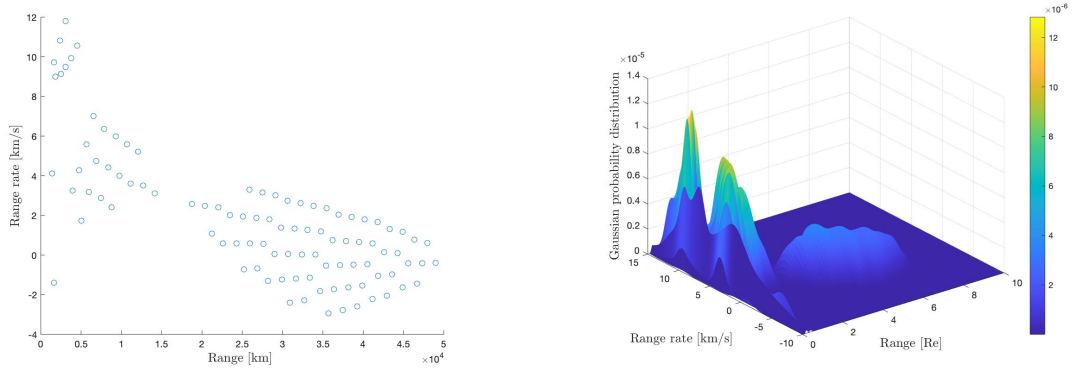
Some assumptions and properties associated with the Kalman filter are

- The state is not correlated with the measurement noise
- It makes no requirement that the distribution be Gaussian
- It makes no requirement that the measurement function be linear
- The state is not correlated with the measurement noise
- It propagates and updates only the first and second moment statistics
- It employs a linear update law, i.e. a linear gain
- It forces an unbiased posterior estimate (can be relaxed)
- It minimizes the posterior mean square error (minimum variance)

## Extended Kalman Filtering For GMM Generated From The Admissible Region

As discussed in chapter 6, the Admissible Region can be approximated by Gaussian Mixture Model. Now for propagating the mean and covariance associated with the Gaussian Mixture Model, one can use the Extended Kalman filter as the system has non-linear dynamics. For propagation, two-body dynamics is assumed without any perturbation or process noise. The state of the object is propagated in Cartesian coordinates (Geocentric Equatorial system) therefore the mean and covariance in range range-rate is approximated to geocentric coordinates. This is discussed in detail in section 3.2. After the transformation, the mean and covariance are propagated using Extended Kalman filter to a given time. The propagated mean and covariance is back-transformed to range range-rate for getting the GMM in measurement space.

Figure 7.1 shows the GMM obtained from the propagated mean and covariance and the respective position of these propagated means. It can be observed that the Admissible Region has changed shape after the propagation. This is because the orbits from the initial Admissible Region land in a different range range-rate region at a later time due to orbital evolution. An additional, undesired, effect are errors introduced by linearization.



(a) Location of Gaussian mixture components.

(b) Surface plot of the Gaussian mixture.

Fig. 7.1.: Gaussian mixture representation of the constrained Admissible Region

In all the previous chapters, the discussion has been centred on how to approximate Admissible Region using Gaussian Mixture Model and further about the propagation of these Gaussian Mixture Models (state and uncertainty) using Extended Kalman filter. The question which now arises is how to capture the information contained in these Gaussian Mixture Models for finding the overlap between two TSAs. The concepts developed in information theory can be used to find such information which is discussed in the next chapter.

#### 7.2.4 Numerical Error Build-up During EKF

The limitation of using numerical integration is the build-up of numerical errors. One way to check numerical error is by checking the volume of covariance matrix before and after propagation without any process noise. The volume (determinant) of the covariance matrix before and after propagation remains the same if no process noise is taken into account. This happens because the shape of the matrix changes but the total volume remains the same so if the numerical error is building up then that will be reflected in the determinant of the covariance matrix.

$$|\mathbf{P}_0| = |\mathbf{P}(t)| \quad (7.10)$$

To minimize the numerical error, two ways of covariance propagation can be tested. One is the classical approach mentioned above.

$$\dot{\mathbf{P}}(t) = \mathbf{F}(\mathbf{m}(t))\mathbf{P}(t) + \mathbf{P}(t)\mathbf{F}^T(\mathbf{m}(t)) + \mathbf{M}(t)\mathbf{Q}_s(t)\mathbf{M}^T(t) \quad (7.11)$$



The other method uses the propagation of state transition matrix.

$$\begin{aligned}
\Phi(t_{k-1}, t_{k-1}) &= \mathbf{I} \\
\dot{\Phi}(t, t_{k-1}) &= \mathbf{F}(\mathbf{m}(t))\Phi(t, t_{k-1}) \\
\dot{\mathbf{Q}}_c(t) &= \mathbf{F}(\mathbf{m}(t))\mathbf{Q}_c(t) + \mathbf{Q}_c(t)\mathbf{F}^T(\mathbf{m}(t)) + \mathbf{M}(t)\mathbf{Q}_s(t)\mathbf{M}^T(t) \\
\mathbf{P}(t) &= \Phi(t_{k-1}, t_{k-1})\mathbf{P}(t_{k-1})\Phi^T(t_{k-1}, t_{k-1}) + \mathbf{Q}_c(t)
\end{aligned} \tag{7.12}$$

During the EKF propagation, there is an accumulation of numerical errors, which eventually affects the rank of the covariance matrix. For finding the overlap using Kullback-Leibler divergence, the inverse of the covariance is needed to be well defined but due to numerical error, the covariance matrices become rank deficient. Therefore, different ways of covariance propagation have been tested to get less numerical error. Choosing between these two formulations of covariance propagation can play a major role in numerical integration as numerical errors propagate differently in both of these methods for a longer time duration. If one has a better-scaled initial state transition matrix and badly scaled initial covariance matrix then it would be better to use the latter method because numerical error will be less in state transition matrix propagation whereas if one has better scaled covariance matrix and a badly scaled state transition matrix then it would be better to use direct covariance propagation to minimize numerical errors.

To demonstrate this, the table below shows the error build using both methods of covariance propagation. Determinant of covariance matrix of one component of the GMM before EKF is 8.1742e-11.

Table 7.1.: Comparison of volume of uncertainty between classical and state transition matrix method for covariance propagation

Propagation time	Difference in determinants of covariance before and after EKF using classical method	Difference in determinants of covariance before and after EKF using state transition matrix method
100 minutes	1.2960e-12	1.0000e-15
500 minutes	7.6601e-08	1.1620e-12
1000 minutes	7.6601e-08	2.6780e-12

These numerical errors can also play a role in making the covariance matrix rank deficient. The rank of a matrix is defined as the maximum number of linearly independent column or row vectors in a matrix. The concept of rank, though clear in the exact arithmetic context, is tricky in the presence of round-off error. If a matrix is rank deficient, then the inverse of the matrix is not defined as the determinant is zero. Therefore, to solve the problem of rank deficiency for finding the matrix inverse, different methods can be employed:

- **Singular value decomposition (SVD)** [27]: SVD helps in handling the matrix rank problem. It introduces the practical notion of numerical rank. In SVD, an  $m$  by  $n$  matrix  $G$  is factored into

$$G = USV^T \quad (7.13)$$

where,  $U$  is an  $m$  by  $n$  orthogonal matrix with columns that are unit basis vectors spanning the data space,  $R^m$ ,  $V$  is an  $n$  by  $n$  orthogonal matrix with columns that are basis vectors spanning the model space,  $R^n$  and  $S$  is an  $m$  by  $n$  diagonal matrix with non-negative diagonal elements called singular values. The SVD can be used to compute a generalized inverse of  $G$ , called the Moore–Penrose pseudo inverse because it has desirable inverse properties originally identified by Moore and Penrose.

$$G^\dagger = V_p S_p^{-1} U_p^T \quad (7.14)$$

Numerical rank deficiency are nicely characterized in terms of SVD because the singular values indicate how near a given matrix is to the matrix of lower rank.

- **Cholesky decomposition [27]:** It is a decomposition of a positive definite matrix into the product of a lower triangular matrix and its conjugate transpose. Matrix inversion based on the Cholesky decomposition is numerically stable for well-conditioned matrices.

$$A = LL^T \quad (7.15)$$

The inverse using Cholesky decomposition can be defined as

$$A^{-1} = [L^T]^{-1} L^{-1} \quad (7.16)$$

The Cholesky decomposition is unique when A is positive definite; there is only one lower triangular matrix L with strictly positive diagonal entries such that  $A = LL^T$

In this thesis, Cholesky decomposition has been used to find the inverse of rank deficient matrices because inverse using Cholesky decomposition when multiplied with the matrix itself gave the resultant matrix close to the identity matrix.

## 8. INFORMATION MEASURES

This chapter introduces the basic definitions required for the development of information theory [28]. For any probability distribution, there are multiple ways in which information can be obtained from it. Entropy is one such quantity which is the self-information of a random variable. The entropy  $N(X)$  of a discrete random variable  $X$  is defined as

$$N(X) = - \sum_{x \in \mathcal{X}} p(x) \log p(x) \quad (8.1)$$

Here, the log is to the base two. This entropy is similar to the definition of entropy in thermodynamics. Some important properties associated with entropy are as follows: (1) it is always greater than or equal to zero; (2) the base of the logarithm in the definition can be changed which can also change the entropy of a random variable. The joint entropy  $N(X,Y)$  of a pair of discrete random variables  $(X,Y)$  with a joint distribution  $p(x,y)$  is defined as

$$N(X,Y) = - \sum_{x \in \mathcal{X}} \sum_{y \in \mathcal{Y}} p(x,y) \log p(x,y) \quad (8.2)$$

Similar to entropy, mutual information is a measure of the amount of information one random variable contains about another. It is a special case of relative entropy, which is a measure of the distance between two probability distributions. The mutual information  $I(X;Y)$  is the relative entropy between the joint distribution and the product distribution  $p(x)p(y)$ .

$$I(X; Y) = - \sum_{x \in \mathcal{X}} \sum_{y \in \mathcal{Y}} p(x, y) \log \frac{p(x, y)}{p(x)p(y)} \quad (8.3)$$

Relationship between entropy and mutual information is defined as:

$$I(X; Y) = N(X) - N(X|Y) \quad (8.4)$$

It is the reduction in uncertainty of  $X$  due to knowledge of  $Y$ . The mutual information of a random variable with itself is the entropy of a random variable, also sometimes referred to as self-information.

The relative entropy is also referred to as the Kullback-Leibler divergence. The Kullback-Leibler (KL) [16] divergence is a widely used tool in statistics and pattern recognition. It is not a true distance between distributions since it is not symmetric and does not satisfy the triangular inequality.

The KL-divergence or the relative entropy, between two probability density functions  $f(x)$  and  $g(x)$  is given as,

$$D(f||g) = \int f(x) \log \frac{f(x)}{g(x)} dx \quad (8.5)$$

For two Gaussians  $f$  and  $g$ , the KL divergence has a closed formed expression,

$$D(\hat{f}||\hat{g}) = \frac{1}{2} \left[ \log \frac{|\Sigma_{\hat{g}}|}{|\Sigma_{\hat{f}}|} + Tr[|\Sigma_{\hat{g}}|^{-1}|\Sigma_{\hat{f}}|] - d + (\mu_{\hat{f}} - \mu_{\hat{g}})^T |\Sigma_{\hat{g}}|^{-1} (\mu_{\hat{f}} - \mu_{\hat{g}}) \right] \quad (8.6)$$

where, mean is defined as

$$\mu_f = E\{x\} = \int_{-\infty}^{\infty} x f(x) dx \quad (8.7)$$

and  $\sigma^2$  is defined as

$$\sigma_f^2 = \int_{-\infty}^{\infty} (x - E\{x\})^2 f(x) dx \quad (8.8)$$

$$= E\{(x - E\{x\})^2\} \quad (8.9)$$

The divergence satisfies three properties which are as follows:

- Self similarity:  $D(f \parallel f) = 0$

This means that the KL divergence of a normal distribution with itself is zero.

- Self identification:  $D(f \parallel g) = 0$  only if  $f = g$

This means that if KL divergence of one distribution with other distribution is zero then it means that the other distribution is simply the same distribution.

- Positivity:  $D(f \parallel g) \geq 0$  for all f, g

This means that the KL divergence between any two distributions is always zero or positive.

## 8.1 KL Divergence Between Gaussian Mixture Models

The KL divergence between two Gaussian Mixture Models (GMMs) is frequently needed in the fields of speech and image recognition. Unfortunately, no such closed-form exists for the KL divergence between two GMMs, nor does any efficient computational algorithm exist. In that case, to calculate the KL divergence between two Gaussian Mixture Models different strategies can be employed. For example, KL divergence can be calculated by taking all component from one GMM with all component from the other GMM or by correlating one component from one GMM to any one of the components in the other GMM.

In this work, KL divergence is calculated in the range range-rate space, Geocentric Equatorial frame, Keplerian orbital elements space and Delaunay orbital elements space to draw a comparison in different spaces. The difference in KL divergence can

arise from the fact that in different element spaces, the mean and covariance differ because of non-linear dynamics employed for transformation.

For finding out the Kullback-Leibler divergence between two Gaussian Mixture Models, two strategies have been developed which are given below.

### 8.1.1 All Components

In this approach, each mean from one Gaussian Mixture Model is correlated with all the means in another Gaussian Mixture Model taken one at a time (refer 8.1). This way total value of divergence is taken as the sum of KL divergence calculated using all of these combinations. For example, if a GMM has two components and another has three components, then two components from GMM one are correlated with all the three components of GMM two. Therefore, there are a total of six combinations possible and all of these are taken for finding KL divergence which is then divided by the number of such combinations. The KL divergence value of a component with itself is zero as it is the same distribution. But in this case, all the combinations of components are taken which results in non-zero value of KL divergence even for the GMM with itself. This happens because even for the same GMM, the components are separated from each other and therefore KL divergence gives us an average of how far each component is from other components in the same GMM.

### 8.1.2 Using Optimized Matching

This approach is based on the principle of the linear assignment problem. The linear assignment problem is a way of assigning rows to columns such that each row is assigned to a column and the total cost of the assignments is minimized (or maximized). The cost of assigning each row to each column is captured in a cost matrix. The entry  $\text{cost}(i,j)$  is the cost of assigning row  $i$  to column  $j$ . Therefore, each mean from one GMM distribution is matched with one mean from the other GMM such that the total of the distance between all matched means is minimized (refer 8.2.

This implementation is done using *matchpairs* function in Matlab. If KL divergence is calculated for a GMM with itself, then *matchpairs* associates the component with itself because it is closest to itself. Therefore, each component is associated with itself. This gives KL divergence value as zero because it is calculating the average of KL divergence between two same distributions. Whereas when two different GMMs are selected, for example before and after the EKF propagation, the position of mean has shifted and also the shape of the uncertainty has changed, therefore KL divergence gives a non-zero value.

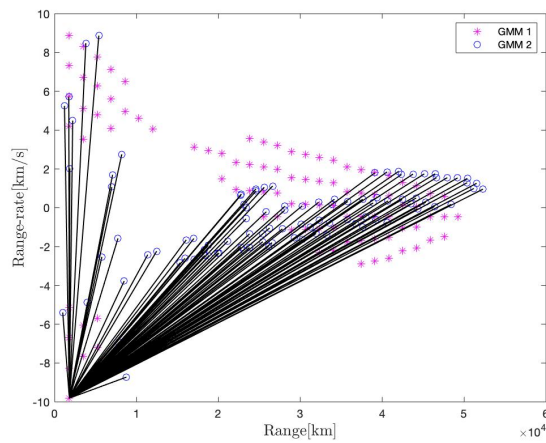


Fig. 8.1.: All components with all components for two GMMs

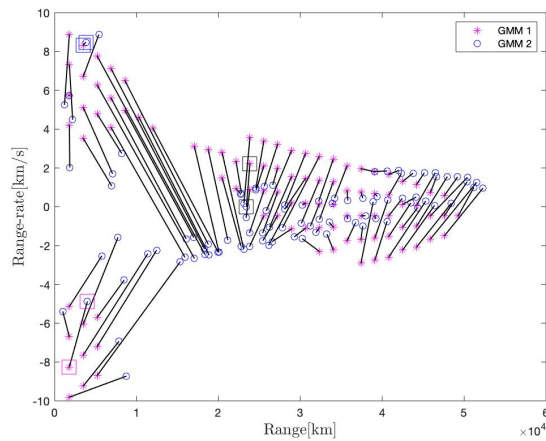


Fig. 8.2.: Optimized matching of components for two GMMs



## 9. MONTE-CARLO SIMULATIONS

In a non-linear transformation, Gaussianity is not preserved. For such transformations, the linearization using Jacobians is employed for approximating the probability distributions and in turn, the new obtained distribution is not Gaussian in nature. Since state and uncertainty associated with an object are transformed within several coordinate systems and orbital element spaces, Monte-Carlo simulation is performed to check if the transformation between these spaces/coordinate systems can be approximated as linear. A random number generator is used to generate measurements (range, range-rate) around each mean in the Topocentric Equatorial system. These measurements are then transformed to the Geocentric Equatorial coordinate system using the equations in section 3.2. The corresponding mean and covariance are also transformed from Topocentric Equatorial coordinate system to Geocentric Equatorial coordinate system. The location of the state vector of these points with respect to the corresponding mean will provide a true representation of uncertainty transformation from measurement to state space.

If this transformation is well approximated as linear, then state vector associated with generated points will be well aligned with the standard deviation intervals of transformed covariance.

Mathematically, this can be illustrated by calculating Mahalanobis distance (MD) [29], which is the measure of the distance between a point and a distribution in terms of standard deviations of that distribution.

$$MD = (\mathbf{X} - \tilde{\mathbf{X}}).(P_X).(\mathbf{X} - \tilde{\mathbf{X}})^T \quad (9.1)$$

If the transformation from one space to another is linear then the average MD of all the points will be equal to the dimension of the state:

$$\tilde{M}D = \frac{1}{N_p} \sum_{j=1}^{N_p} MD_j = 6 \quad (9.2)$$

where,  $N_p$  denotes the number of Monte-Carlo points.

### **Geocentric Equatorial Coordinate System To Keplerian Orbital Element Space**

Mean, covariance and Monte-Carlo points are transformed from Geocentric Equatorial Coordinate system to Keplerian orbital element space using the equations from section 4.1. Mahalanobis distance is then calculated using these transformed points, means and covariances.

### **Keplerian Orbital Element Space to Delaunay Orbital Element Space**

Mean, covariance and Monte-Carlo points are transformed from Keplerian orbital element space to Delaunay orbital element space using the equations from section 4.2. Mahalanobis distance is then calculated using these transformed points, means and covariances.

To check how well does the linearization work, a GEO object with given angular measurements is taken

$$\alpha = 1.6542 \quad \dot{\alpha} = 7.3055e - 05 \quad (9.3)$$

$$\delta = 0.0240 \quad \dot{\delta} = -4.6598e - 06 \quad (9.4)$$

These measurements are then used to create the admissible region which is further approximated as GMM. The mean and covariance associated with GMM are in the Topocentric Equatorial coordinate system. As shown in this chapter,  $N_p = 10000$  points are generated around these means which are further transformed to Cartesian coordinates, Keplerian orbital elements and Delaunay orbital elements subsequently.

Further, Mahalanobis distance is calculated using these points and the associated mean to see how far these points are located from the distribution in terms of its standard deviation. Figure 9.1 shows the distribution of points in range and range-rate space generated using random number generator. Figure 9.2 shows the position of Monte-Carlo points and mean transformed to Keplerian orbital elements. Figure 9.3 shows the position of Monte-Carlo points and mean transformed to Delaunay orbital elements.

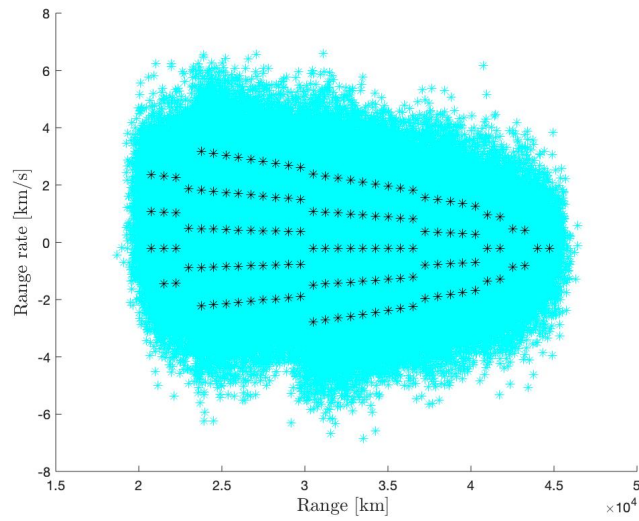
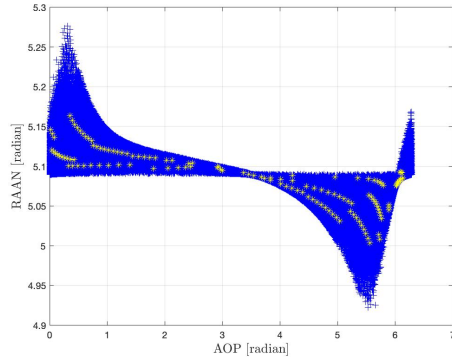
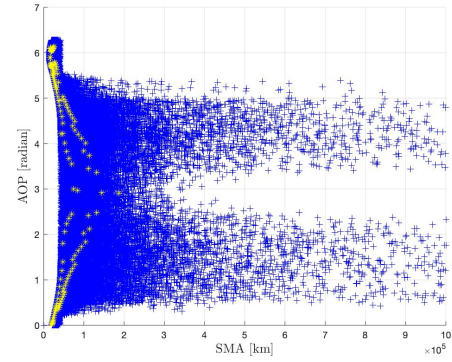


Fig. 9.1.: Position of Monte-Carlo points and mean in range range-rate space



(a) RAAN vs argument of periapsis



(b) Argument of periapsis vs semimajor axis

Fig. 9.2.: Position of Monte-Carlo points and mean transformed to Keplerian orbital elements

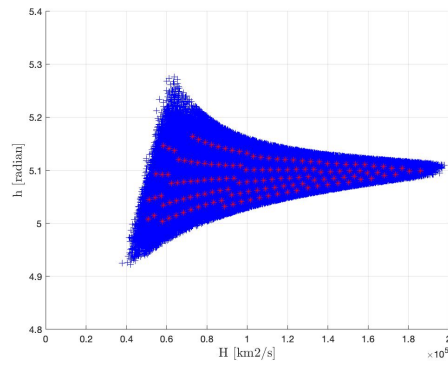
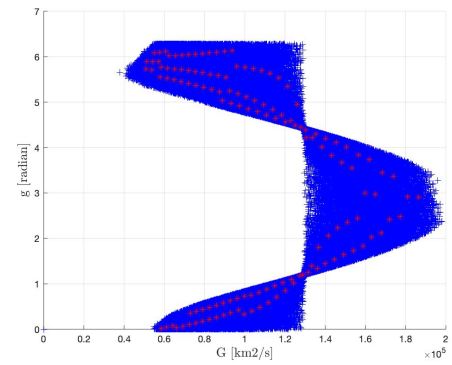
(a)  $h$  vs  $H$ (b)  $g$  vs  $G$ 

Fig. 9.3.: Position of Monte-Carlo points and mean transformed to Delaunay orbital elements

Table 9.1.: Mahalanobis distance in different frames

Coordinate frame/Orbital element space	Mahalanobis distance
Range range-rate	1.9971
Cartesian coordinates	1.9971
Keplerian orbital element space	2.1487e+21
Delaunay orbital element space	6.2982e+11

The Mahalanobis distance in range range-rate frame comes out to be 1.9971 which is approximately equal to the dimension of covariance matrices in range range-rate space. This is because no transformation is done for calculating MH distance here. The value of MH distance in Cartesian coordinates is 1.9971, in Keplerian orbital elements is  $2.1487\text{e}+21$  and in Delaunay orbits elements is  $6.2982\text{e}+11$ . These values are not close to dimension six of covariance matrices in the respective frames. This happens because the transformation is non-linear and Jacobians is just a way of linearizing the non-linear transformation.

## 10. SIMULATION MODEL

All the previous chapters have provided the necessary background to implement our method for solving the linkage problem. This chapter discusses the overall flow of simulations done for this work. It includes a sensor measurement model, target motion model and simulation procedure.

### 10.1 Sensor Measurement Model

Sensor measurements are observed using optical sensors in the Topocentric Equatorial system. The measurements consist of right ascension ( $\alpha$ ), declination ( $\delta$ ), rate of change of right ascension with time ( $\dot{\alpha}$ ) and rate of change of declination angle ( $\dot{\delta}$ ). The error in the measurements angles is taken to be 2.5 arc second in  $\alpha$ , 2.3 arc second in  $\delta$ , 0.5 arc second per second in  $\dot{\alpha}$  and 0.4 arc second per second in  $\dot{\delta}$ . Using Topocentric Equatorial position and velocity,  $\alpha$ ,  $\delta$ ,  $\dot{\alpha}$  and  $\dot{\delta}$  can be found out using equation 3.3 and the ones given below.

$$\dot{\alpha} = \frac{x\dot{y} - y\dot{x}}{\tilde{r}^2} \quad (10.1)$$

$$\dot{\delta} = \frac{\tilde{r}}{r^2} \left( \dot{z} - \frac{z(x\dot{x} + y\dot{y})}{\tilde{r}^2} \right) \quad (10.2)$$

$$\text{Therefore, } z = [\alpha, \dot{\alpha}, \delta, \dot{\delta}] \quad (10.3)$$

## 10.2 Target Motion Model

The target motion model is assumed to be the Two-body motion model where the central body is the Earth and the other body is the object. The equation of motion of the object with respect to Earth can be given as

$$\ddot{\vec{r}} = -\frac{\mu\vec{r}}{|\vec{r}|^3} \quad (10.4)$$

where,  $\vec{r} = x\hat{e}_x + y\hat{e}_y + z\hat{e}_z$   $|\vec{r}| = \sqrt{x^2 + y^2 + z^2}$

where  $\vec{r}$  is the position vector of the object in the Geocentric Equatorial coordinate system (section 3.1),  $\mu$  is the Gravitational parameter of Earth.

For finding the dynamics Jacobian (refer equation 7.9), let the state of the object be denoted by  $X = [x, y, z, \dot{x}, \dot{y}, \dot{z}]$  which is nothing but the geocentric position and velocity of the object. Therefore, the dimension of the state  $n_x = 6$ . Then, the dynamic state equation can be given by:

$$\dot{X} = \mathbf{F}(X)X \quad (10.5)$$

$$\mathbf{F}(X) = \begin{bmatrix} \frac{\partial \dot{x}}{\partial x} & \frac{\partial \dot{x}}{\partial y} & \frac{\partial \dot{x}}{\partial z} & \frac{\partial \dot{x}}{\partial \dot{x}} & \frac{\partial \dot{x}}{\partial \dot{y}} & \frac{\partial \dot{x}}{\partial \dot{z}} \\ \frac{\partial \dot{y}}{\partial x} & \frac{\partial \dot{y}}{\partial y} & \frac{\partial \dot{y}}{\partial z} & \frac{\partial \dot{y}}{\partial \dot{x}} & \frac{\partial \dot{y}}{\partial \dot{y}} & \frac{\partial \dot{y}}{\partial \dot{z}} \\ \frac{\partial \dot{z}}{\partial x} & \frac{\partial \dot{z}}{\partial y} & \frac{\partial \dot{z}}{\partial z} & \frac{\partial \dot{z}}{\partial \dot{x}} & \frac{\partial \dot{z}}{\partial \dot{y}} & \frac{\partial \dot{z}}{\partial \dot{z}} \\ \frac{\partial \ddot{x}}{\partial x} & \frac{\partial \ddot{x}}{\partial y} & \frac{\partial \ddot{x}}{\partial z} & \frac{\partial \ddot{x}}{\partial \dot{x}} & \frac{\partial \ddot{x}}{\partial \dot{y}} & \frac{\partial \ddot{x}}{\partial \dot{z}} \\ \frac{\partial \ddot{y}}{\partial x} & \frac{\partial \ddot{y}}{\partial y} & \frac{\partial \ddot{y}}{\partial z} & \frac{\partial \ddot{y}}{\partial \dot{x}} & \frac{\partial \ddot{y}}{\partial \dot{y}} & \frac{\partial \ddot{y}}{\partial \dot{z}} \\ \frac{\partial \ddot{z}}{\partial x} & \frac{\partial \ddot{z}}{\partial y} & \frac{\partial \ddot{z}}{\partial z} & \frac{\partial \ddot{z}}{\partial \dot{x}} & \frac{\partial \ddot{z}}{\partial \dot{y}} & \frac{\partial \ddot{z}}{\partial \dot{z}} \end{bmatrix} \quad (10.6)$$

$$\begin{bmatrix} \dot{x} \\ \dot{y} \\ \dot{z} \end{bmatrix} = \begin{bmatrix} 0 & 0 & 0 & 1 & 0 & 0 \\ 0 & 0 & 0 & 0 & 1 & 0 \\ 0 & 0 & 0 & 0 & 0 & 1 \\ -\frac{\mu x}{|r|^3} & 0 & 0 & 0 & 0 & 0 \\ 0 & -\frac{\mu y}{|r|^3} & 0 & 0 & 0 & 0 \\ 0 & 0 & -\frac{\mu z}{|r|^3} & 0 & 0 & 0 \end{bmatrix} \begin{bmatrix} x \\ y \\ z \\ \dot{x} \\ \dot{y} \\ \dot{z} \end{bmatrix} \quad (10.7)$$

### 10.3 Simulation Procedure

Given a set of TSAs, these simulations aim to solve the correlation problem. These TSAs are generated from the TLE set of the catalogued GEO and LEO objects from space-track.org. The TLE, when propagated through SGP4 propagator, gives the geocentric position and velocity at a given epoch. This position and velocity is used to generate the measurement angles  $z = [\alpha, \dot{\alpha}, \delta, \dot{\delta}]$  or the TSA. These measurement angles when combined with the range and range-rate values, give all the possible orbits related to these angles and the region obtained is called the Admissible Region. Consider a set of measurement angles belonging to object one obtained at time  $t_1$ . This measurement is used to generate the Admissible Region, which in turn is approximated using a Gaussian Mixture Model. The output of this process is a GMM obtained from object one at time  $t_1$ . The measurement from object one is tested against measurement taken from object two at time  $t_2$ . Therefore, the same process is followed to get GMM from object two at time  $t_2$ . To bring both the measurements at the same time, GMM from the measurement of object one is propagated to time  $t_2$  using the Extended Kalman filter. This step brings the GMM of both objects at the same time  $t_2$ . Thereafter, the overlap between two GMMs can be calculated using KL divergence. To test which coordinate frame or orbital elemental space work better, KL divergence can be calculated by range range-rate space, Cartesian coordinates, Keplerian orbital elements and Delaunay elements by transforming the GMMs to these spaces. The state of an object changes continuously in range range-rate and



Cartesian coordinates so it is expected that the KL divergence values may not show less overlap even if it is the same object. In the case of Keplerian orbital elements, five out of six orbital elements remain fixed for the same object even after propagation using two-body dynamics and therefore it is expected that the KL divergence will be able to distinguish better in this frame. The same is true for Delaunay orbital elements as only the mean anomaly of an object changes with time.

### 10.3.1 GEO Objects

In this model, Geocentric Equatorial positions and velocities are used to obtain a set of measurements,  $z = [\alpha, \dot{\alpha}, \delta, \dot{\delta}]$ . These positions and velocities are generated from SGP4 propagator by using Two-line element data. The Two-line data is publicly available at [space-track.org](http://space-track.org). The TLE set of the catalogued GEO and LEO objects are taken.

### Admissible Region

Once the angular measurement data is obtained, an Admissible Region can be created if the position and velocity of topocenter are known. These measurements along with a set of range values are used to create an Admissible Region. The range of range values is taken from 20000 km to 47000 km for Geostationary orbits.

The epoch for generating all these measurements is taken to be 8<sup>th</sup> April, 2019. The geographical latitude and longitude of the observer is taken to be 0.01259° North and 127° West, respectively. The radius of Earth is taken to be 6378.14 km and the angular velocity of Earth is taken to be 7.2921159e-5. Refer section 5.1 for more details.

## Creating Bivariate GMM From Admissible Region

The created Admissible Region can be approximated using bivariate GMM for its probabilistic analysis. Given values for  $\sigma_{\rho,max}$  and  $\sigma_{\dot{\rho},max}$ , number of components in both range and range-rate direction can be found out. Each set of measurement will produce different Admissible Region, which in turn will give a different number of components with fixed  $\sigma_{\rho,max}$  and  $\sigma_{\dot{\rho},max}$ . To maintain the uniformity for all cases, the number of components is fixed for each object. Here, each Admissible Region is approximated using 800 components. Finally, GMM will comprise of mean and covariances associated with these 800 components. Refer chapter 6 for more details.

## Propagation Mean and Covariance Using Extended Kalman Filter

The mean and covariance obtained in the previous step are in the Topocentric Equatorial coordinate system. So, firstly these mean and covariances are transformed into the state vector and the covariance matrix in the Geocentric Equatorial coordinate system (refer 3.2). These transformed mean and covariance are propagated through Runge-Kutta of order 45 numerical integrator using Extended Kalman filter (refer 7.2). The time of propagation is varied for testing the KL divergence with time. For this propagation, the model is taken without any process noise. These propagated mean and covariance is then transformed to various orbital element spaces for evaluating KL divergence.

## Calculating Kullback-Leibler Divergence

The propagated mean and covariance in the Geocentric Equatorial coordinate system are transformed back to the Topocentric Equatorial system. They are also transformed to Keplerian orbital element (refer 4.1) space and Delaunay orbital element space (refer 4.2). The KL divergence is calculated in the following spaces using (1) all components (refer 8.1.1) and (2) optimized pair matching (refer 8.1.2).

- Topocentric Equatorial coordinate system
- Geocentric Equatorial coordinate system
- Keplerian Orbital element space
- Delaunay Orbital element space

The flow chart given below show how KL divergence is calculated

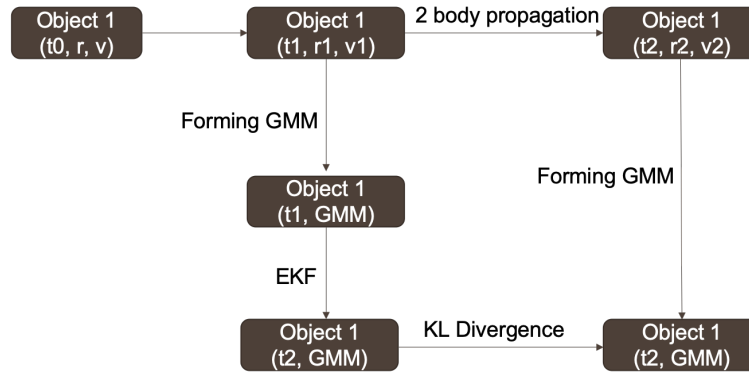


Fig. 10.1.: Flowchart for finding KL divergence of object 1 with itself after EKF

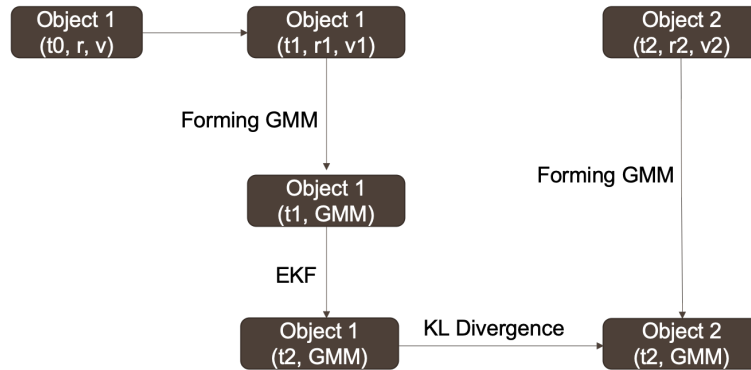


Fig. 10.2.: Flowchart for finding KL divergence of object 1 with object 2

### 10.3.2 LEO Objects

For LEO objects, the same procedure is followed for finding the overlap between two TSAs. The range of range values is taken from 100 km to 3000 km for Low earth

orbits. The geographical latitude and longitude of the observer is taken to be  $40.4237^\circ$  North and  $86.9212^\circ$  West, respectively. All the other parameters are taken the same as for GEO objects.

## 11. RESULTS

Simulations for GEO object are divided into three scenarios: (1) visible GEO objects are taken from TLE data and these are then propagated in Cartesian coordinates during Extended Kalman filter; (2) visible GEO are sorted with respect to one single object so as the behaviour of KL divergence can be studied if the orbits are close together; (3) visible GEO objects are taken from TLE data and these are then propagated in Keplerian orbital elements during Extended Kalman filter. This is done because for a two-body dynamics, the propagation in Keplerian orbital elements will only change mean anomaly keeping other quantities as constant and also the transformation from Cartesian coordinates to Keplerian orbital elements after EKF can be eliminated. All of these three scenarios are propagated for 10 minutes, 30 minutes and 500 minutes to see the change in behavior of KL divergence with respect to time.

For the LEO orbits, the visibility of an object from a topocenter keeps changing because the position of LEO objects with respect to the position of the topocenter doesn't remain fixed. This is because both of them move at different rates. The LEO objects are also propagated for two scenarios: (1) visible GEO objects are taken from TLE data and these are then propagated in Cartesian coordinates during Extended Kalman filter; (2) objects are taken irrespective of their visibility but those objects which have magnitude of position less than the radius of the Earth after Extended Kalman filter are eliminated. Scenario 1 is propagated for 3 minutes and 10 minutes. Scenario 2 is propagated for 3 minutes and 10 minutes.

### 11.1 GEO Unsorted And Propagated In Cartesian Coordinates

This section presents results for variation of KL divergence when 50 objects are taken at random and then these 50 objects are paired to make 25 cases. The only

criteria used for selecting these 50 objects is that they are visible from the topocenter for the whole duration of propagation. These 25 cases are propagated for 10 minutes, 30 minutes and 500 minutes each to see how KL divergence changes with time. The KL values are also calculated in different frames to draw more information about its behaviour. The main difference in this section and section 11.3 is the way Extended Kalman filter is being initiated and propagated. In this section, the propagation in EKF takes place in Cartesian coordinates i.e geocentric position and velocity. For section 11.3, the propagation in EKF takes place in Keplerian orbital elements. Figure 11.1 shows the orbits of the objects taken for finding the overlap.

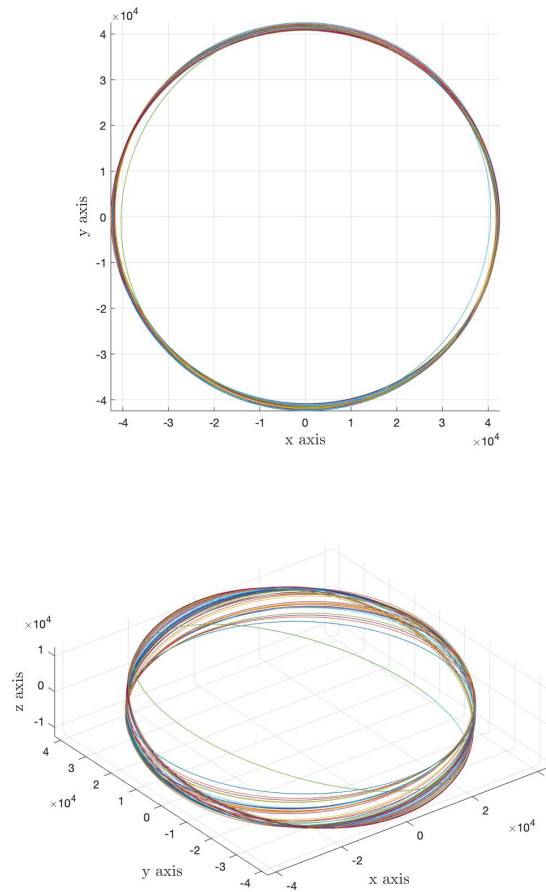
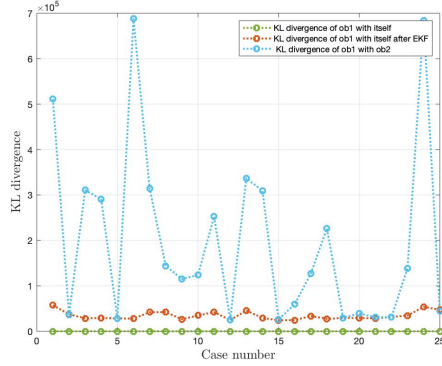
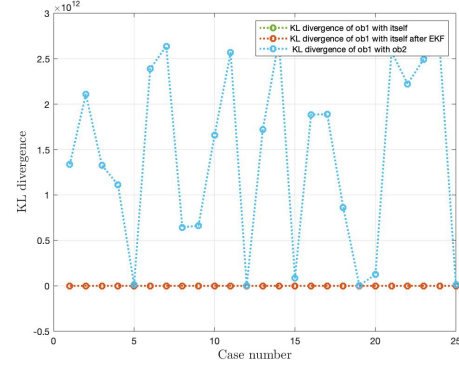


Fig. 11.1.: Plot of GEO objects

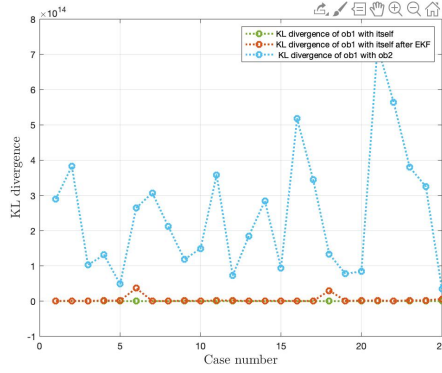
### GEO scenario 1: Propagation Time-10 minutes



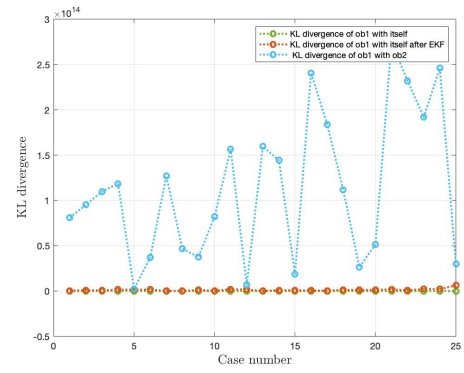
(a) in range range-rate space



(b) in Cartesian coordinates



(c) in Keplerian orbital elements



(d) in Delaunay orbital elements

Fig. 11.2.: Plot for KL divergence vs case number. a) in range range-rate space b) in Cartesian coordinates c) in Keplerian orbital elements d) in Delaunay orbital elements for 10 minutes propagation time using optimized matching of components

Figure 11.2 shows the plot for KL divergence (y-axis) for different frames with respect to each case (x-axis) for 10 minutes propagation time. For each case, optimized matching of components is used for calculation of KL divergence as discussed in section 8.1.2. Here, the green line represents KL divergence between GMM of object 1 with itself obtained from TSA at time  $t_2$ . The red line represents KL divergence between two GMMs of object 1 obtained from TSA at time  $t_2$  and GMM propagation from time  $t_1$  to  $t_2$  using Extended Kalman filter. The red line, hence, represents a correct or true correlation, when both TSAs stem indeed from the same object. For

the correlation in range-rate, one can see that nevertheless, the KL divergence is not exactly zero (compare with green, when the AR is correlated with itself directly). The reason for this is that the shape of the Admissible Region, even over short time intervals is not constant. The orbits that fall into the Admissible Region at time  $t_1$  are different ones than at time  $t_2$  even for the very same object. This is because the Admissible Region is an observer to orbit geometry dependent. Lastly, the blue line represents the KL divergence between GMM of object 2 obtained from TSA at time  $t_2$  and GMM of object 1 obtained from uncertainty propagation from time  $t_1$  to  $t_2$  using Extended Kalman filter. In 11.2 part b), the red line represents again the KL between the TSAs of object 1. Here, it can be seen that the line is right on top of the green line. For a two-body orbit, the Cartesian coordinates are indeed reproducing from time  $t_1$  propagated to time  $t_2$ . Linearization effects are negligible over this very short propagation time. In c), the same TSA correlation is shown in Keplerian orbital elements. Here, it can be seen that except in two cases the red line is right on top of the green line. The low KL divergence is expected as orbital elements are constant for the same orbit. The two cases, case 6 and 18 may be attributed to linearization errors. In Delaunay orbital elements, part d) of the figure, as the elements are reproducing for the same orbit in the two-body assumption, the expected correlation is shown: the red line is right on top of the green one. The numeric difference between them is not zero but of the order  $10e+11$ .



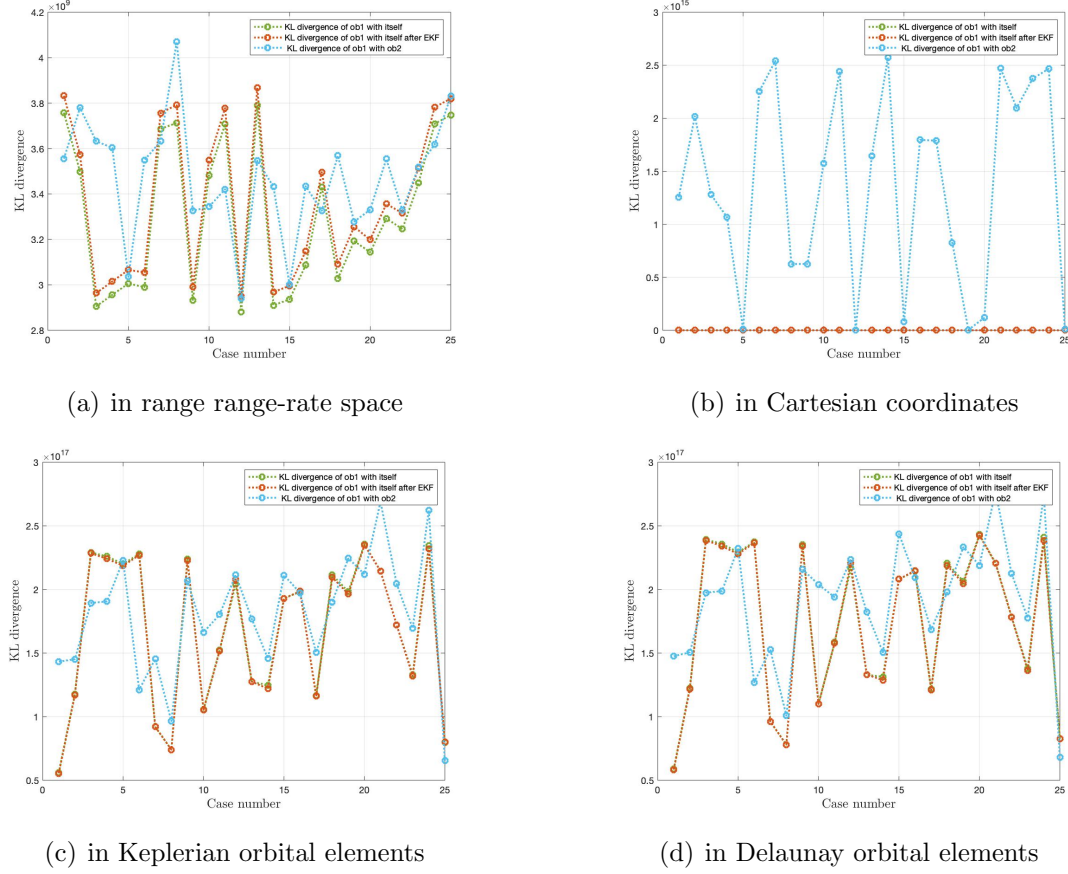
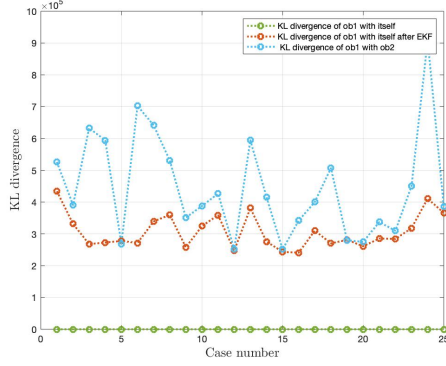


Fig. 11.3.: Plot for KL divergence vs case number. a) in range range-rate space b) in Cartesian coordinates c) in Keplerian orbital elements d) in Delaunay orbital elements for 10 minutes propagation time using all components

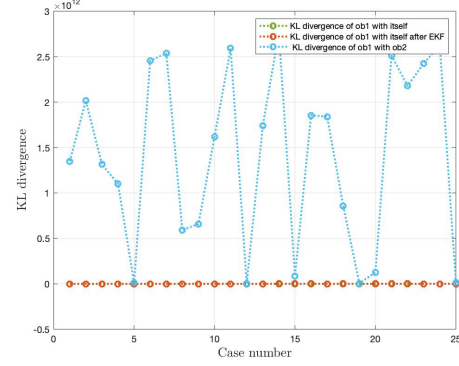
Figure 11.3 shows the plot for KL divergence for different frames with respect to each case for 10 of minutes propagation time. For each case, all components are used for the calculation of KL divergence as discussed in section 8.1.1. Here, the green line represents KL divergence between GMM of object 1 with itself obtained from TSA at time  $t_2$ . Here, the KL divergence of an object with itself is not zero because a combination of all the components is used for calculation of KL divergence (green line). The red line represents KL divergence between two GMMs of object 1 obtained from TSA at time  $t_2$  and GMM propagation from time  $t_1$  to  $t_2$  using Extended Kalman filter. In the figure (a), (c) and (d), green line and red line are still closely following each other in the pattern but the overall value of KL divergence

has increased since all the components are used for evaluation. Lastly, the blue line represents the KL divergence between GMM of object 2 obtained from TSA at time  $t_2$  and GMM of object 1 obtained from uncertainty propagation from time  $t_1$  to  $t_2$  using Extended Kalman filter. As the value of KL divergence has increased, the blue line also lies in the same range of KL divergence values as the green and red line do for the figure (a),(c) and (d). This means that the differences are exacerbated rather than the similarities. No clear criterion of KL level can be found to discriminate the correct and the wrong correlation. Whereas, for the figure (b) in Cartesian coordinates, the red and the green lie close to each other and are easily distinguishable from the blue line. This is because the GMM after EKF has not undergone any linearization for transformation to other space and therefore shows the expected trend.

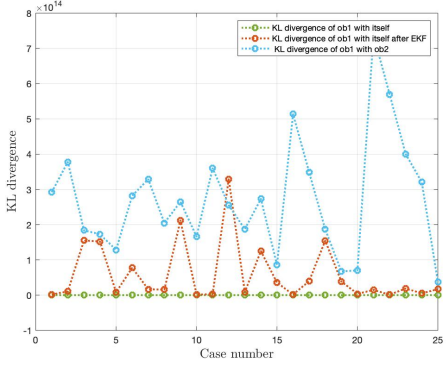
### GEO scenario 1: Propagation time-30 minutes



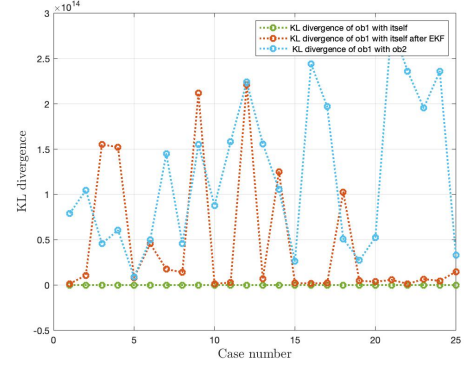
(a) in range range-rate space



(b) in Cartesian coordinates



(c) in Keplerian orbital elements



(d) in Delaunay orbital elements

Fig. 11.4.: Plot for KL divergence vs case number. a) in range range-rate space b) in Cartesian coordinates c) in Keplerian orbital elements d) in Delaunay orbital elements for 30 minutes propagation time using optimized matching of components

Figure 11.4 shows the plot for KL divergence for different frames with respect to each case for 30 minutes of propagation time. For each case, optimized matching of components is used for calculation of KL divergence as discussed in section 8.1.2. Here, the green line represents KL divergence between GMM of object 1 with itself obtained from TSA at time  $t_2$ . Each point on the green line is zero because optimized matching between the same GMM associates the same component with itself, therefore, there is no divergence for all 4 cases. The red line represents KL divergence between two GMMs of object 1 obtained from TSA at time  $t_2$  and GMM propagation

from time  $t_1$  to  $t_2$  using Extended Kalman filter. For 30 minutes, there is an increase in the level of KL as compared to 10 minutes propagation time. This happens because the Admissible Region has changed even more for 30 minutes duration as compared to 10 minutes duration in the previous case because of an observer to orbit geometry change with time. Therefore, the Admissible Region at time  $t_2$  now encompasses more different orbits. In figure (a), the green and red line show more difference in KL values in the range range-rate frame because the Admissible Region changes its shape with the observer to orbit geometry. In figure (c) and (d), the red line is much closer to the green line because most of the orbital elements in the Keplerian and Delaunay orbital element space remain fixed with time for a two-body motion. In the figure (d), it is clear that the KL values of points on the red line which are farther than the green line in Keplerian orbital element have further increased. This is due to the linearization arising due to the transformation from frame to another. In figure (b), the green line still is closely followed by the red line because for 30 minutes propagation in GEO the object hasn't travelled too far.

Lastly, the blue line represents the KL divergence between GMM of object 2 obtained from TSA at time  $t_2$  and GMM of object 1 obtained from uncertainty propagation from time  $t_1$  to  $t_2$  using Extended Kalman filter. For figure (a), there is a significant difference in blue and green line but due to increased level of KL values for the red line, it is difficult to comment on correlation based on KL values for some cases like 5 and 15. The same happens with case 13 of figure (c). In figure (d), as KL values on red line have increased further, more cases with KL values are higher for the red line as compared with blue line can be found. However, in figure (b), the blue line has a higher level of KL values as compared with the red and green line. Therefore, the correlation can be easily done for all cases except 5, 13, 15, 19 and 25.

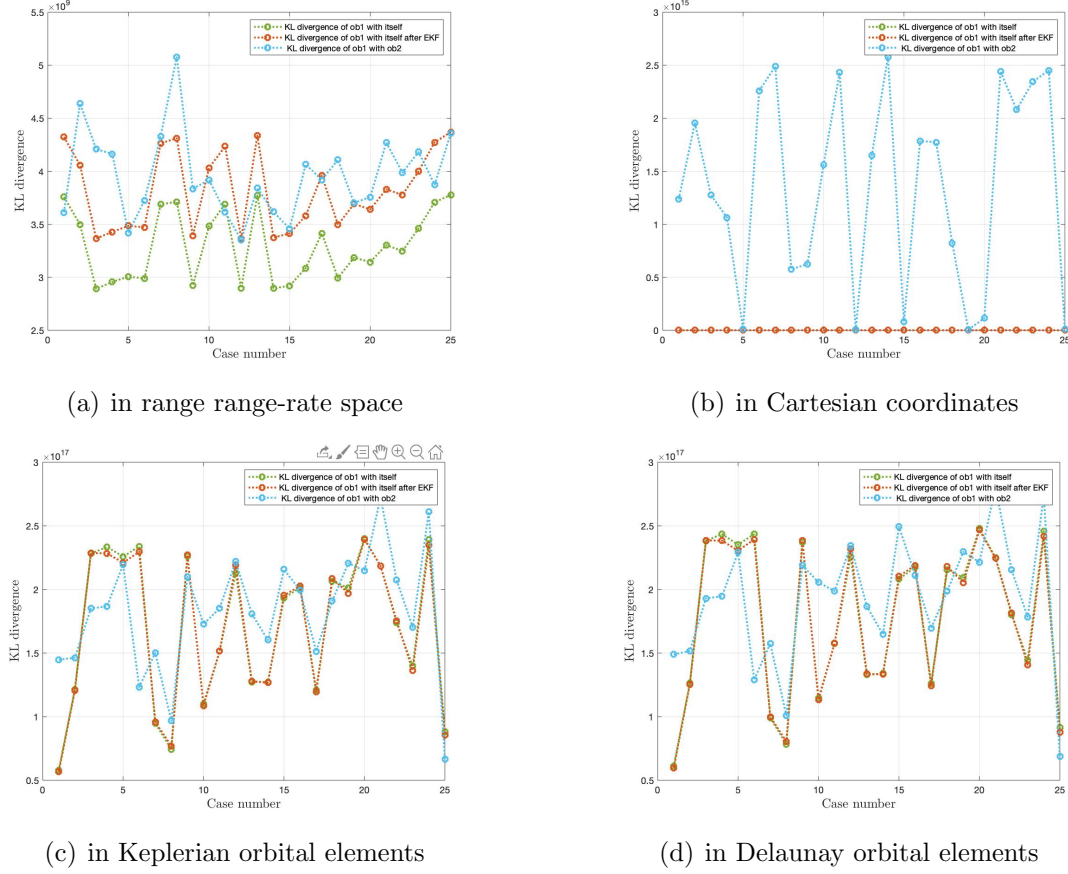


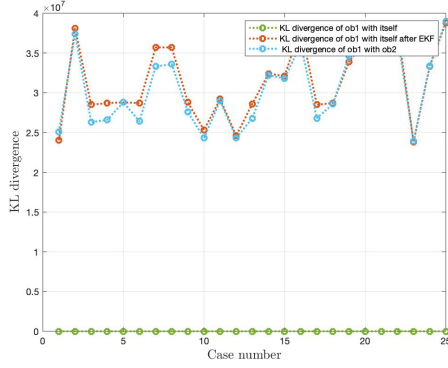
Fig. 11.5.: Plot for KL divergence vs case number. a) in range range-rate space b) in Cartesian coordinates c) in Keplerian orbital elements d) in Delaunay orbital elements for 30 minutes propagation time using all components

Figure 11.5 shows the plot for KL divergence for different frames with respect to each case for 30 minutes propagation of time. For each case, all components are used for the calculation of KL divergence as discussed in section 8.1.1. Here, the green line represents KL divergence between GMM of object 1 with itself obtained from TSA at time  $t_2$ . As seen previously, the KL values on the green line are not zero because a combination of all the components is used for the calculation of KL divergence. The red line represents KL divergence between two GMMs of object 1 obtained from TSA at time  $t_2$  and GMM propagation from time  $t_1$  to  $t_2$  using Extended Kalman filter. For part (a), as the Admissible Region has changed more for 30 minutes propagation time with respect to the Admissible Region for 10 minutes propagation time, the

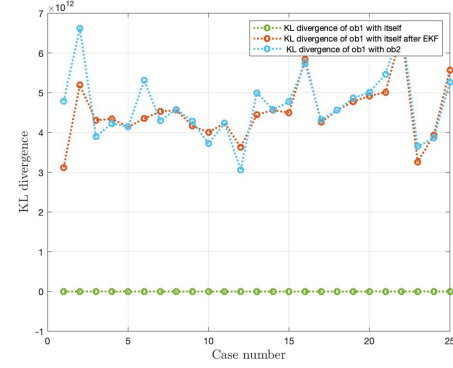
difference in KL values of green and red line has increased. For part (b), the green line is still closely followed by the red line. For part (c) and (d), the KL values for some cases on green line become higher than the red line. This might be because of a combination of two things: the object has travelled for a longer time as compared to 10 minutes, and transformation to other spaces has affected the KL values due to linearization.

Lastly, the blue line represents the KL divergence between GMM of object 2 obtained from TSA at time  $t_2$  and GMM of object 1 obtained from uncertainty propagation from time  $t_1$  to  $t_2$  using Extended Kalman filter. Using all components has increased the level of KL values. In part (a), the KL values for the blue line are still higher than the red and green line for more than half the cases. In part (b), the KL values on the blue line can be easily distinguished from the green and red line. This is because KL divergence is calculated in Cartesian coordinates which is the same frame used for EKF propagation. In part (c) and (d), the KL values for green, red and blue line lie close to each other, therefore, making it hard to comment on the correlation.

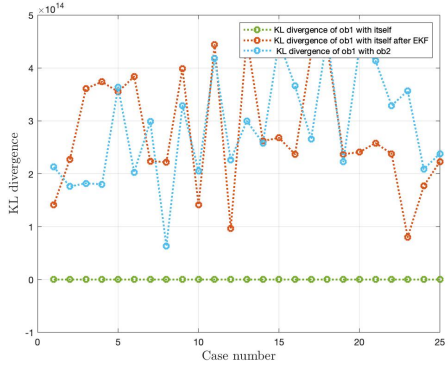
### GEO scenario 1: Propagation Time-500 minutes



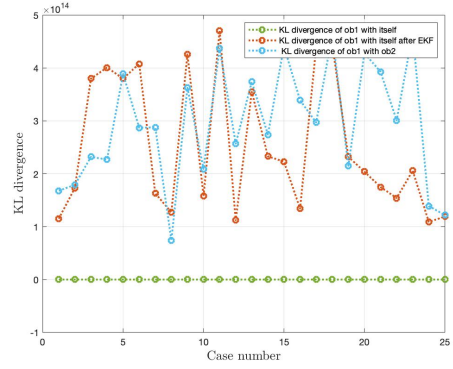
(a) in range range-rate space



(b) in Cartesian coordinates



(c) in Keplerian orbital elements



(d) in Delaunay orbital elements

Fig. 11.6.: Plot for KL divergence vs case number. a) in range range-rate space b) in Cartesian coordinates c) in Keplerian orbital elements d) in Delaunay orbital elements for 500 minutes propagation time using optimized matching of components

Figure 11.6 shows the plot for KL divergence for different frames with respect to each case for 500 minutes of propagation time. For each case, optimized matching of components is used for calculation of KL divergence as discussed in section 8.1.2. Here, the green line represents KL divergence between GMM of object 1 with itself obtained from TSA at time  $t_2$ . For all parts, the KL values for all cases are equal to zero as *matchpairs* function maps the component with itself if the same GMM is given. The red line represents KL divergence between two GMMs of object 1 obtained from TSA at time  $t_2$  and GMM propagation from time  $t_1$  to  $t_2$  using Extended Kalman

filter. For part (a), the red line is far apart from the green line as the Admissible Region has changed a lot for 500 minutes propagation time due to observer to orbit geometry. For part (b), a similar trend is seen for the red curve as the object has moved too far in Cartesian coordinates as well. For part (c) and (d), the red line is far from the green line as mean anomaly has changed significantly in these orbital element spaces. Lastly, the blue line represents the KL divergence between GMM of object 2 obtained from TSA at time  $t_2$  and GMM of object 1 obtained from uncertainty propagation from time  $t_1$  to  $t_2$  using Extended Kalman filter. For part (a) and (b), the blue line is closely followed by the red line. For part (c) and (d), the KL values for less than half cases show higher for the blue line as compared to the red line. This is again due to two reasons: linearization of the non-linear system of equations for transformation; longer time for propagation.



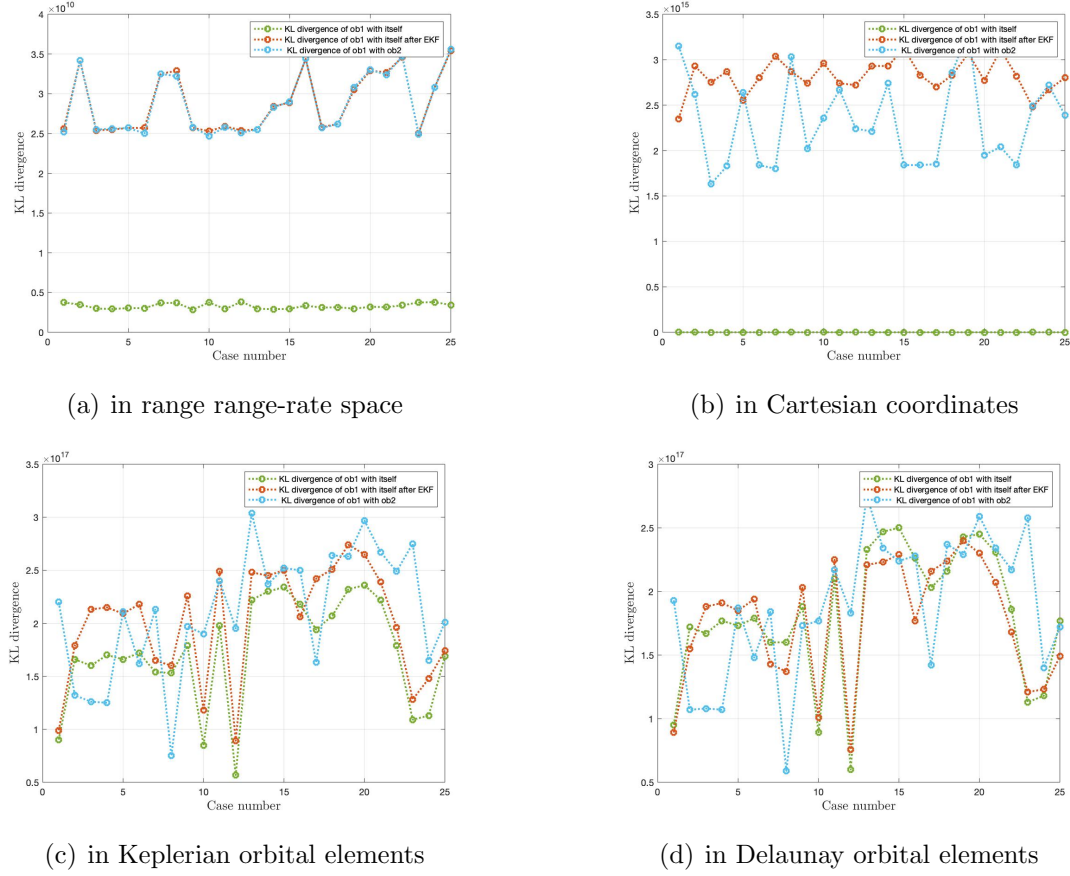


Fig. 11.7.: Plot for KL divergence vs case number. a) in range range-rate space b) in Cartesian coordinates c) in Keplerian orbital elements d) in Delaunay orbital elements for 500 minutes propagation time using all components

Figure 11.7 shows the plot for KL divergence for different frames with respect to each case for 500 minutes of propagation time. For each case, all components are used for the calculation of KL divergence as discussed in section 8.1.1. Here, the green line represents KL divergence between GMM of object 1 with itself obtained from TSA at time  $t_2$ . For all parts, the KL values on the green line are non zero as all components are used. In part (b), the green line looks close to x-axis because the green line is of order  $10^7$  whereas the KL values on the red and blue line are of order  $10^{15}$ . The red line represents KL divergence between two GMMs of object 1 obtained from TSA at time  $t_2$  and GMM propagation from time  $t_1$  to  $t_2$  using Extended Kalman filter. For 500 minutes, the Admissible Region has much more different orbits as compared to

the original Admissible Region. Therefore, the gap between green and red line has increased much more for part (a) and (b). For part (c) and (d), the green and red line are close to each other because the orbital elements in Keplerian and Delaunay orbital elements remain fixed except for mean anomaly. So, there is more overlap in GMMs of the same object. Lastly, the blue line represents the KL divergence between GMM of object 2 obtained from TSA at time  $t_2$  and GMM of object 1 obtained from uncertainty propagation from time  $t_1$  to  $t_2$  using Extended Kalman filter. For part (a), the blue line is close to the red line for all cases. For part (b), the red line is farther from the green line as compared to the blue line for most cases. This is because, for a longer duration, the Gaussian components have moved far for the same object after EKF. For part (c) and (d), KL values on green, red and blue line do not show any correlation trend for the majority of cases because the propagation over longer periods, worsens the linearization errors that are accumulated.

## 11.2 GEO Sorted And Propagated In Cartesian Coordinates

In the previous section, the GEO objects visible from the topocenter have been taken at random for each case. For this section, the objects are sorted such that all the cases have object 1 as common and it is linked with other objects after selecting the closest objects from the Two-line element data. The first 5 cases have objects which lie in the following tolerances of first object's Keplerian orbital elements: semi-major axis-10 km, eccentricity-0.1, angle of inclination-1°, the argument of periapsis-15° and right ascension of ascending node-10°. Similarly, the rest 15 objects lie within tolerances as follows: semi major axis-400 km, eccentricity-0.2, angle of inclination-15°, the argument of periapsis-40° and right ascension of ascending node-40°. These results can give an estimate of how KL divergence behaves if the objects are close to each other for 10 minutes, 30 minutes and 500 minutes. Figure 11.8 shows the plot for 21 GEO objects which are taken with orbits close to each other.

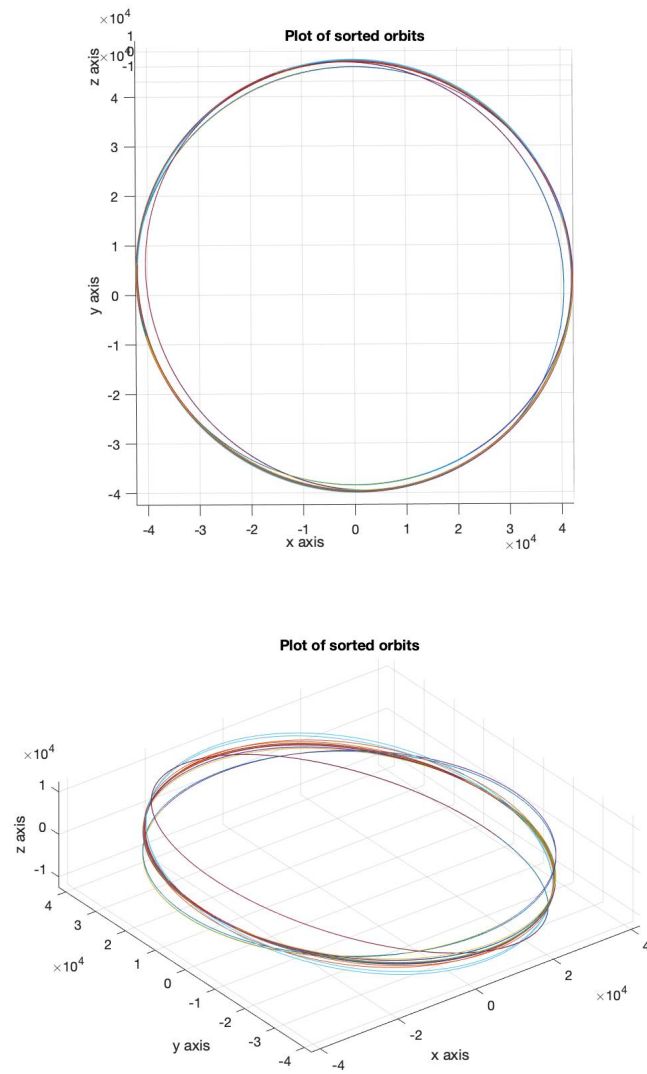


Fig. 11.8.: Plot of GEO objects with orbits close to each other

## GEO Scenario 2: Propagation Time-10 minutes

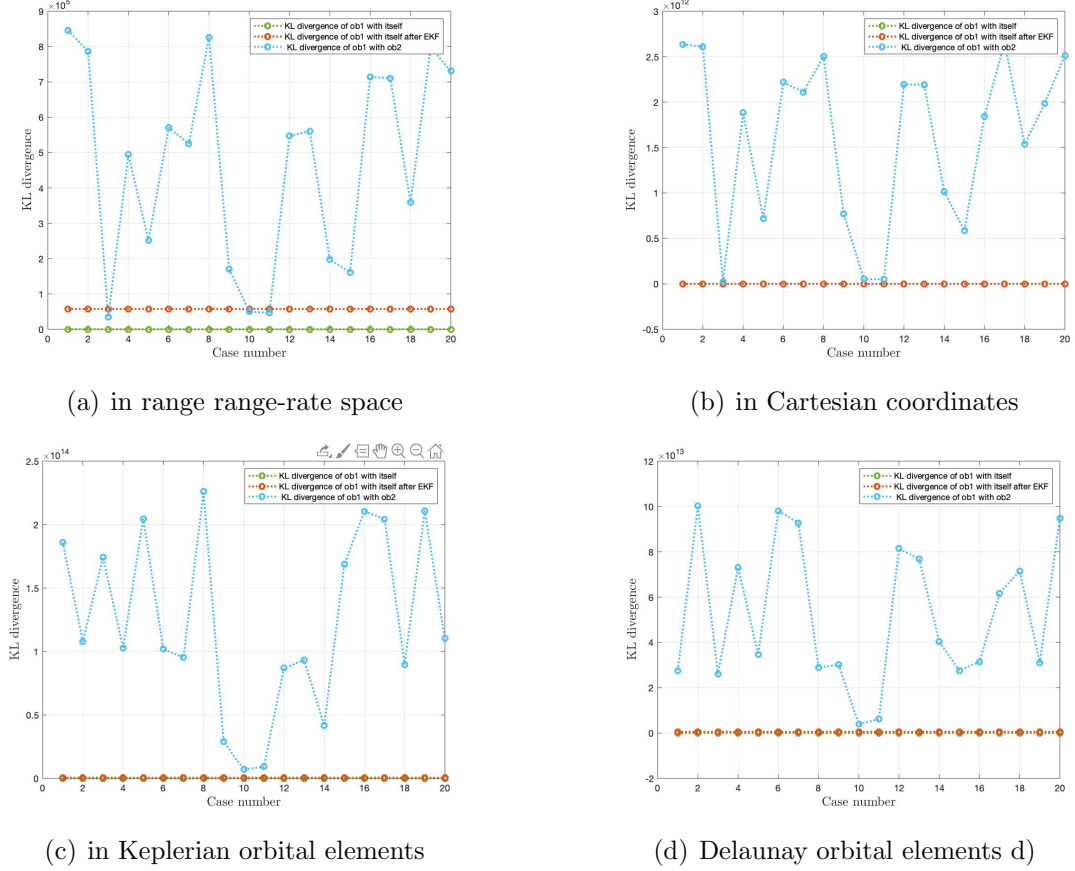
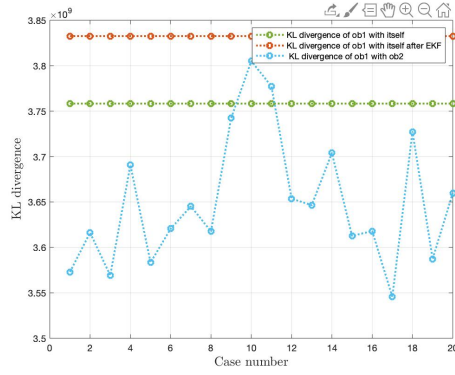


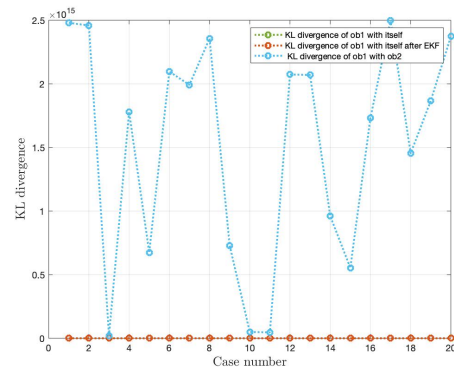
Fig. 11.9.: Plot for KL divergence vs case number. a) in range range-rate space b) in Cartesian coordinates c) in Keplerian orbital elements d) in Delaunay orbital elements for 10 minutes propagation time using optimized matching of components

Figure 11.9 shows the plot for KL divergence for different frames with respect to each case for 10 minutes of propagation time. For each case, optimized matching of components is used for calculation of KL divergence as discussed in section 8.1.2. Here, the green line represents KL divergence between GMM of object 1 with itself obtained from TSA at time  $t_2$ . In all parts, the green line has zero KL values because *matchpairs* associates the component with itself for the same GMM. The red line represents KL divergence between two GMMs of object 1 obtained from TSA at time  $t_2$  and GMM propagation from time  $t_1$  to  $t_2$  using Extended Kalman filter. For all

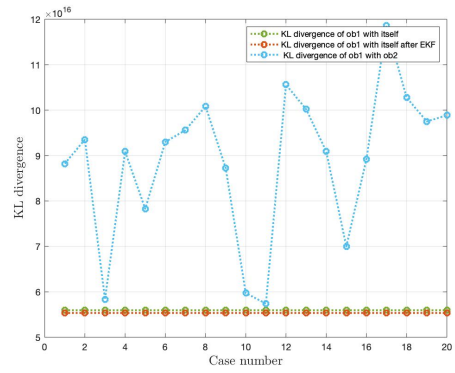
parts, the value of KL divergence for the red line is equal for all cases because, for all the cases, object 1 is fixed. In part (a), the red line is located at close to green line because the object hasn't moved too far, therefore, the Admissible Region hasn't changed much in range range-rate space. In part (b) also the same trend is followed for red and green curve because the object has travelled less for 10 minutes. Along with this, the linearization error accumulated is also less here for part (c) and (d), so green and red line lie close to each other. Lastly, the blue line represents the KL divergence between GMM of object 2 obtained from TSA at time  $t_2$  and GMM of object 1 obtained from uncertainty propagation from time  $t_1$  to  $t_2$  using Extended Kalman filter. In parts (a) and (b), the KL values for the blue line are much higher than red line except for 3, 10 and 11. This is because for these cases the objects lie very close to each other. For part (c) and (d), the blue line is still very higher than the red line. This is because all orbital elements are constant for the same object except mean anomaly and errors accumulated due to linearization are less too. Therefore, correlating the same object is possible in all spaces.



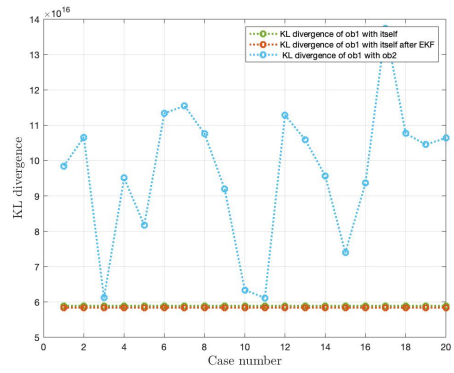
(a) in range range-rate space



(b) in Cartesian coordinates



(c) in Keplerian orbital elements



(d) in Delaunay orbital elements

Fig. 11.10.: Plot for KL divergence vs case number. a) in range range-rate space b) in Cartesian coordinates c) in Keplerian orbital elements d) in Delaunay orbital elements for 10 minutes propagation time using all components

Figure 11.10 shows the plot for KL divergence for different frames with respect to each case for 10 minutes of propagation time. For each case, all components are used for the calculation of KL divergence as discussed in section 8.1.1. Here, the green line represents KL divergence between GMM of object 1 with itself obtained from TSA at time  $t_2$ . For all components, the green line has non-zero KL values as each component is associated with all the other components for calculating KL divergence. The red line represents KL divergence between two GMMs of object 1 obtained from TSA at time  $t_2$  and GMM propagation from time  $t_1$  to  $t_2$  using Extended Kalman filter. In part (a), the KL values for the red line are higher than the green line because even for a small duration of time the Admissible Region has changed after

EKF. For part (b), the value of KL divergence for green and red line differ by order of magnitude one, therefore, these two lines are fall close to each other. For part (c) and (d), as the object has just travelled 10 minutes, the mean anomaly has changed very little (nearly  $2.5^\circ$  for a circular orbit). Therefore, both red and green line nearly overlap the green line. Lastly, the blue line represents the KL divergence between GMM of object 2 obtained from TSA at time  $t_2$  and GMM of object 1 obtained from uncertainty propagation from time  $t_1$  to  $t_2$  using Extended Kalman filter. For part (a), the KL values for the blue line are smaller than the KL values on the red line for all cases. This is because as the objects are very close to each, the overlap between Admissible Regions of object 1 with object 2 using all components is more than with object 1 itself after EKF propagation. Therefore, correlation using KL values will lead to the wrong correlation of second TSA of with object 2 with object 1. For part (b), the blue line is well above the green and red line for all cases except 3, 10 and 11. This is because these cases have objects very close to each other. For part (c) and (d), the KL values of blue lines are still higher than the green and red line for all cases except 3, 10 and 11 because of orbits being very close to each other.

## GEO Scenario 2: Propagation Time-30 minutes

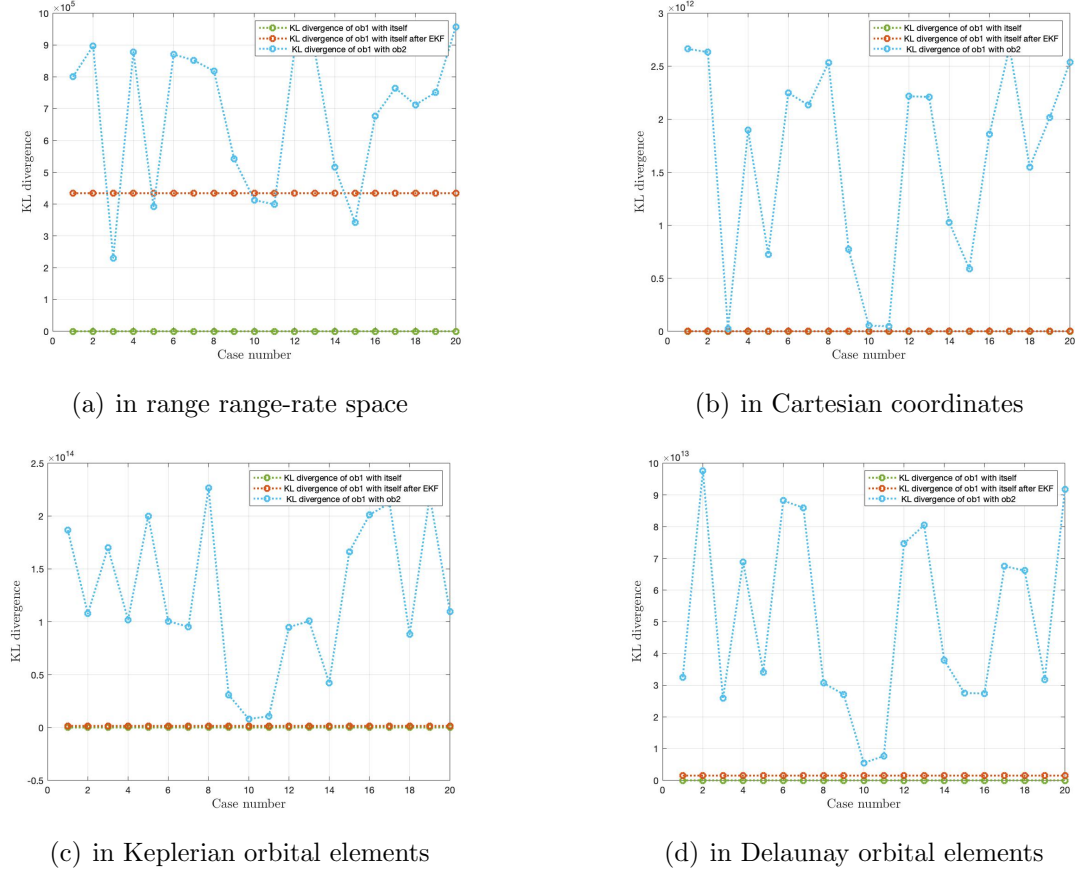
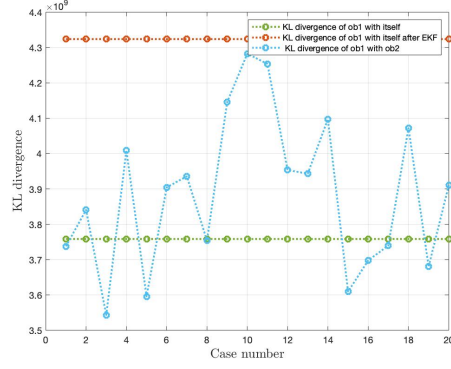


Fig. 11.11.: Plot for KL divergence vs case number. a) in range range-rate space b) in Cartesian coordinates c) in Keplerian orbital elements d) in Delaunay orbital elements for 30 minutes propagation time using optimized matching of components

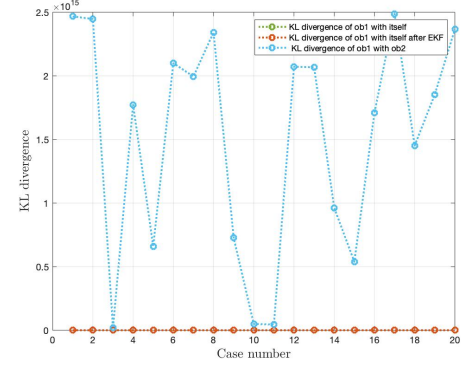
Figure 11.11 shows the plot for KL divergence for different frames with respect to each case for 30 minutes of propagation time. For each case, optimized matching of components is used for calculation of KL divergence as discussed in section 8.1.2. Here, the green line represents KL divergence between GMM of object 1 with itself obtained from TSA at time  $t_2$ . For all parts, the KL values on the green line are zero as each component in the GMM of the Admissible Region is associated with itself by *matchpairs*. The red line represents KL divergence between two GMMs of object 1 obtained from TSA at time  $t_2$  and GMM propagation from time  $t_1$  to  $t_2$



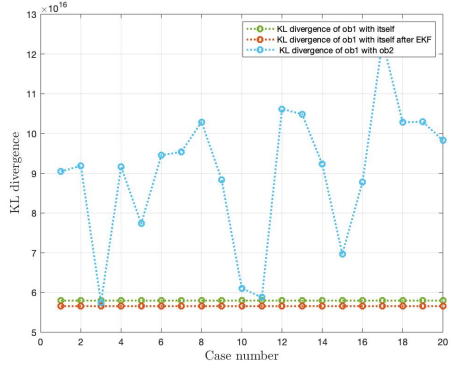
using Extended Kalman filter. The value of KL divergence on the red line and green line are of the same order with an increased gap in between them as compared to figure 11.9 part (a). This is because the Admissible Region has changed more for 30 minutes of propagation time as compared to 10 minutes propagation time. In part (b), the trend is similar to figure 11.9 part (b) with an increased value of KL on the red line. For part (c) and (d), the KL value on the red line has increased by an order of magnitude one compared to figure 11.9 part (c) and part (d). Lastly, the blue line represents the KL divergence between GMM of object 2 obtained from TSA at time  $t_2$  and GMM of object 1 obtained from uncertainty propagation from time  $t_1$  to  $t_2$  using Extended Kalman filter. For part (a), the KL values on the blue line are higher for all cases except for cases 3, 5, 11, 12 and 15. This is because of more change in observer to orbit geometry which leads to some points on the red line giving higher value than the blue line. For part (b), the blue line shows higher KL divergence as compared to the red line. This is because in Cartesian coordinates, the object has moved less even for 30 minutes and thereby causing less change in GMM in Cartesian coordinates. For part (c) and (d), the KL values for the blue line is still higher than red line even after the transformation to these spaces which is because the errors accumulated due to linearization is less.



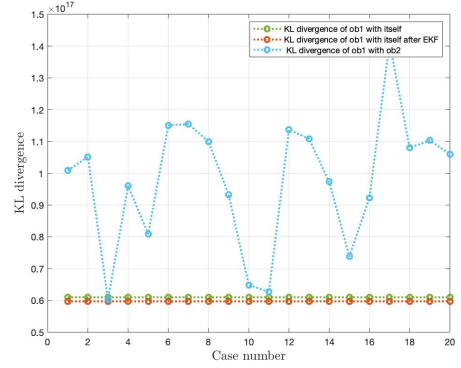
(a) in range range-rate space



(b) in Cartesian coordinates



(c) in Keplerian orbital elements



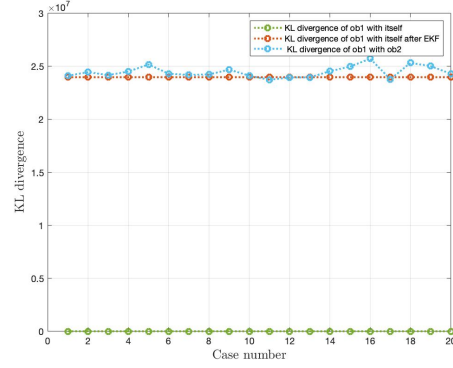
(d) in Delaunay orbital elements

Fig. 11.12.: Plot for KL divergence vs case number. a) in range range-rate space b) in Cartesian coordinates c) in Keplerian orbital elements d) in Delaunay orbital elements for 30 minutes propagation time using all components

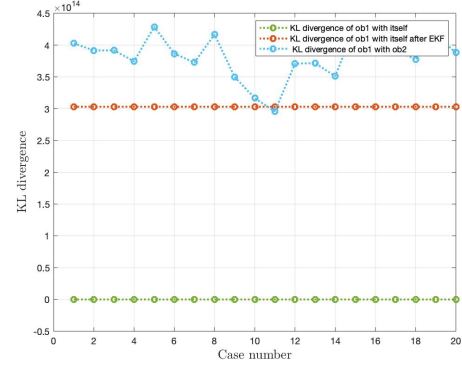
Figure 11.12 shows the plot for KL divergence for different frames with respect to each case for 30 minutes of propagation time. For each case, all components are used for the calculation of KL divergence as discussed in section 8.1.1. Here, the green line represents KL divergence between GMM of object 1 with itself obtained from TSA at time  $t_2$ . For all parts, the KL values on the green line are non-zero as all components are used. The red line represents KL divergence between two GMMs of object 1 obtained from TSA at time  $t_2$  and GMM propagation from time  $t_1$  to  $t_2$  using Extended Kalman filter. For part (a), the gap between red and green line has increased even more compared to the figure 11.10 part (a), because the Admissible Region has changed more for 30 minutes as compared to 10 minutes due to observer

to orbit geometry change. For part (b), the KL values for the red line are higher than the green line by order of magnitude two. For part (c) and (d), the value of KL on green and red line are of the same order of magnitude with KL values on green being higher than the ones on the red line. This is because orbital elements in these space do not change much for a short duration of time and this is accompanied by linearization errors adding up due to transformation to these spaces. Lastly, the blue line represents the KL divergence between GMM of object 2 obtained from TSA at time  $t_2$  and GMM of object 1 obtained from uncertainty propagation from time  $t_1$  to  $t_2$  using Extended Kalman filter. For part (a), the KL divergence for blue line lies in between green and red line for 12 cases. This happens because the Admissible Region has changed more for 30 minute propagation time. As these cases have objects which are close to each other in orbits, it is not easily distinguishable by KL values to determine the correlation between two same objects. For part (b), the KL values on the blue line are still higher than KL values on red line by at least an order of magnitude two. This is because the object has not travelled far for 30 minutes duration time in Cartesian coordinates. For part (c) and (d), the KL values on the red, green and blue line are nearly the same order. The blue line still has higher KL values and therefore can easily determine correlation in these spaces except for case 3, 15 and 15.

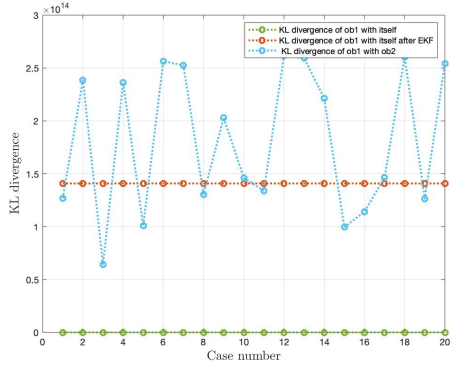
## GEO Scenario 2: Propagation Time-500 minutes



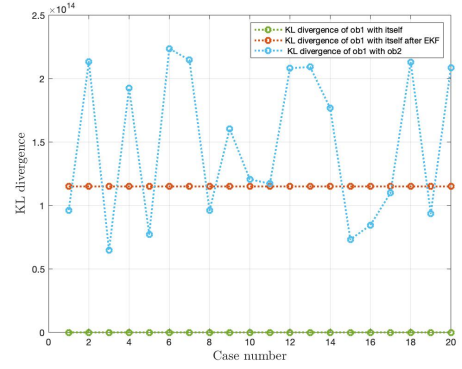
(a) in range range-rate space



(b) in Cartesian coordinates



(c) in Keplerian orbital elements



(d) in Delaunay orbital elements

Fig. 11.13.: Plot for KL divergence vs case number. a) in range range-rate space b) in Cartesian coordinates c) in Keplerian orbital elements d) in Delaunay orbital elements for 500 minutes propagation time using optimized matching of components

Figure 11.13 shows the plot for KL divergence for different frames with respect to each case for 500 minutes of propagation time. For each case, optimized matching of components is used for the calculation of KL divergence as discussed in section 8.1.2. Here, the green line represents KL divergence between GMM of object 1 with itself obtained from TSA at time  $t_2$ . For all parts, the KL values on the green line are zero as the *matchpairs* matches the component with itself. The red line represents KL divergence between two GMMs of object 1 obtained from TSA at time  $t_2$  and GMM propagation from time  $t_1$  to  $t_2$  using Extended Kalman filter. For part (a), the

gap between KL values of green and red line has increased even more as compared to figure 11.11 part (a). This is because the Admissible Region has changed and now has more new orbits for 500 minutes of propagation time as compared to the 30 minutes propagation time due to changes in observation geometry. In part (b), as the propagation time has significantly increased, the KL level has also gone up for the red line. There is a difference of 8 in the order of magnitude of the green and red line. This is because the Cartesian coordinates of the objects are way far from the original coordinates. For part (c) and (d), the same trend is observed for the red line as compared to the green line. Lastly, the blue line represents the KL divergence between GMM of object 2 obtained from TSA at time  $t_2$  and GMM of object 1 obtained from uncertainty propagation from time  $t_1$  to  $t_2$  using Extended Kalman filter. For part (a), the blue line is closely followed by the red line in range range-rate space. In part (b), the KL values on blue line have higher values as compared to the red line except for case 11. Therefore, KL values can still be used to show the correlation with the same object. In part (c) and (d), there is still a significant difference in KL values of the blue line and red line for about half the cases. Although, there are more cases for which KL divergence does not show the right correlation. This is because of the accumulation of more numerical error during transformation over the period of time.

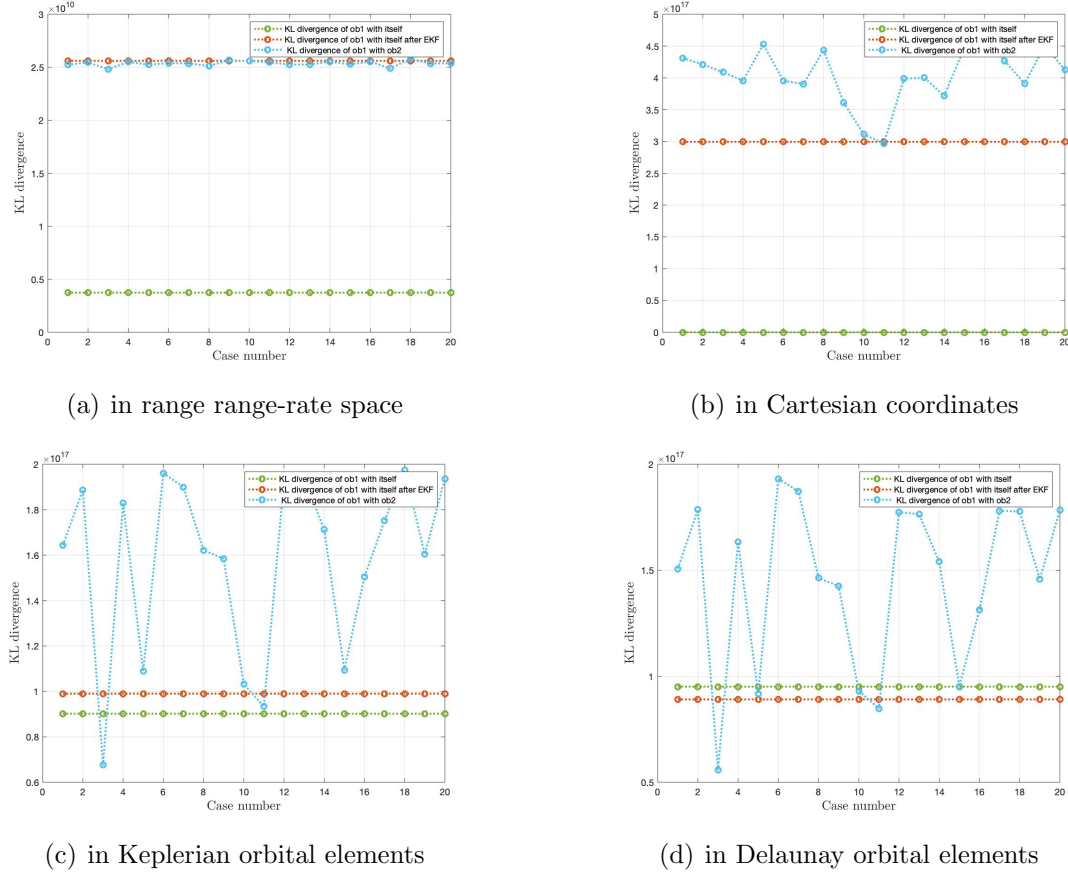


Fig. 11.14.: Plot for KL divergence vs case number. a) in range range-rate space b) in Cartesian coordinates c) in Keplerian orbital elements d) in Delaunay orbital elements for 500 minutes propagation time using all components

Figure 11.14 shows the plot for KL divergence for different frames with respect to each case for 500 minutes of propagation time. For each case, all components are used for the calculation of KL divergence as discussed in section 8.1.1. Here, the green line represents KL divergence between GMM of object 1 with itself obtained from TSA at time  $t_2$ . For all plots, the KL values on the green line are non-zero as all the components are used for finding the KL divergence. The red line represents KL divergence between two GMMs of object 1 obtained from TSA at time  $t_2$  and GMM propagation from time  $t_1$  to  $t_2$  using Extended Kalman filter. For part (a), the difference between KL values on the red line and the green line is of order one. For part (b), the difference in the order of magnitude of green and red line is two for figure

11.12 part (b) but for this case, it has increased to the order of eight. This happens because the object has moved far in the orbit and therefore, the corresponding GMM in Cartesian coordinates has changed too. For part (c) and (d), the same trend is followed but both the green and red line are of the same order. This is because, in the orbital element space, all the orbital elements except mean anomaly do not change for two-body dynamics therefore the GMMs are close to each other. Lastly, the blue line represents the KL divergence between GMM of object 2 obtained from TSA at time  $t_2$  and GMM of object 1 obtained from uncertainty propagation from time  $t_1$  to  $t_2$  using Extended Kalman filter. For part (a), the blue line closely follows the red line with higher values of KL for red line in most cases. This happens because, for a longer duration, the object 1's GMM has more overlap with object 2's GMM due to non-linear propagation of GMM during EKF. For part (b), the KL values on the blue line are higher than the red line except for case 11 and therefore making it easy to correlate two TSAs from object 1 for most cases. This happens because the KL divergence is calculated in the same frame as used for EKF propagation so no transformation to other spaces is taking place. For part (c) and (d), the KL divergence for the blue line is higher than the KL values on the red line for all cases except 3 and 11. These exceptions are arising as orbits are very close to each other.

### 11.3 GEO Unsorted And Propagated In Keplerian Orbital Elements

As mentioned previously, this section shows results for variation of KL divergence values when the propagation is done in Keplerian orbital elements. The propagation has been done for 10 minutes, 30 minutes and 500 minutes. The geocentric position and velocity of an object changes continuously whereas, in the Keplerian orbital elements, only the mean anomaly of an object change continuously and all the other elements remain fixed. Therefore, it is expected that KL divergence values between two objects should give higher values as compared to the object itself. The transfor-

mation to Keplerian orbital elements from Cartesian coordinates after EKF is also eliminated and this will be reflected by a change in KL divergence values.

### GEO Scenario 3: Propagation Time-10 minutes

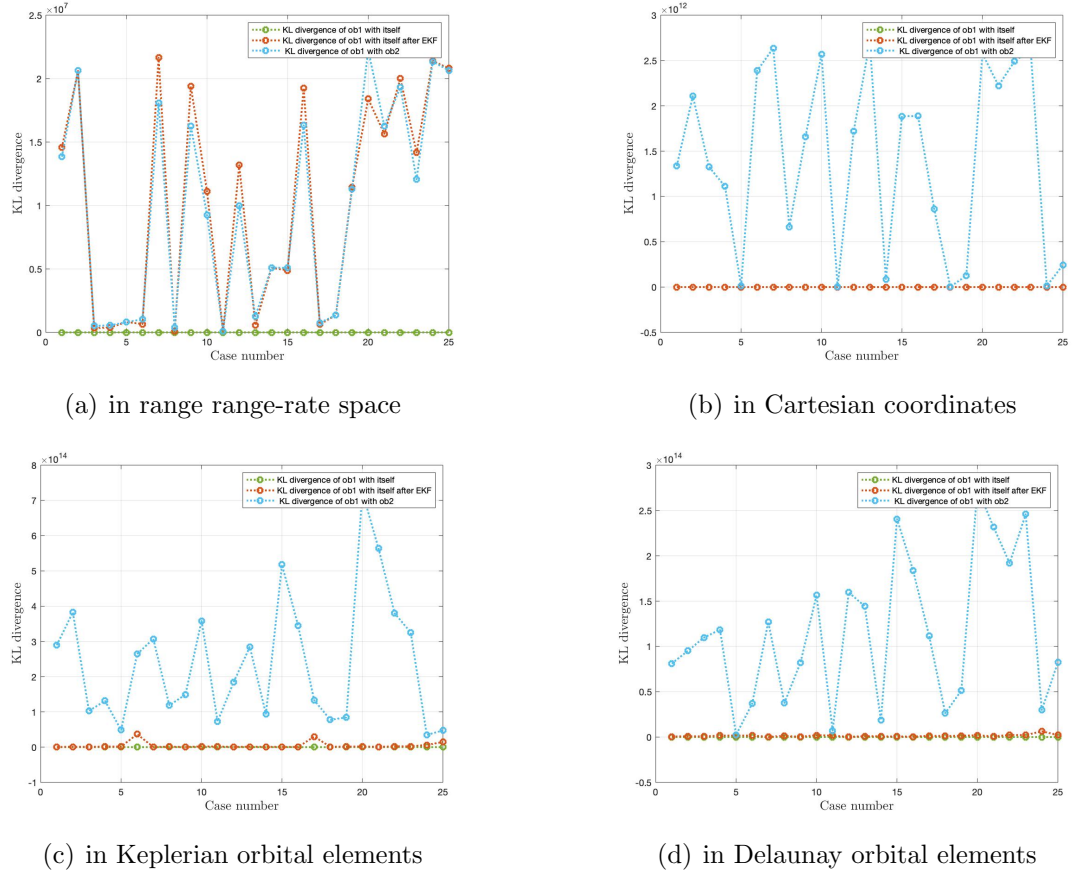


Fig. 11.15.: Plot for KL divergence vs case number. a) in range range-rate space b) in Cartesian coordinates c) in Keplerian orbital elements d) in Delaunay orbital elements for 10 minutes propagation (in Keplerian orbital elements) time using optimized matching of components

Figure 11.15 shows the plot for KL divergence for different frames with respect to each case for 10 minutes of propagation time. For each case, optimized matching of components is used for calculation of KL divergence as discussed in section 8.1.2. Here, the green line represents KL divergence between GMM of object 1 with itself



obtained from TSA at time  $t_2$ . For all parts, KL values on the green line are zero as *matchpairs* associates the component with itself for the same GMM. The red line represents KL divergence between two GMMs of object 1 obtained from TSA at time  $t_2$  and GMM propagation from time  $t_1$  to  $t_2$  using Extended Kalman filter in Keplerian orbital elements. For part (a), the red and green line are separated by an order of magnitude at least four for all cases. The reason for this is because the Admissible Region changes even for a short duration and therefore, the association by *matchpairs* also changes. For part (b), the KL divergence for the red and green line has a difference of about  $10^7$ . This is because the GMM in Cartesian coordinates has changed its shape even for a small duration of time. For part (c) and (d), the KL values for red and green line show a similar trend as part (a) and (b). Lastly, the blue line represents the KL divergence between GMM of object 2 obtained from TSA at time  $t_2$  and GMM of object 1 obtained from uncertainty propagation from time  $t_1$  to  $t_2$  using Extended Kalman filter Keplerian orbital elements. For part (a), the KL values for blue and red line are very close to each other therefore making it difficult to correlate TSAs. For part (b), the KL values for the blue line are higher than the red line for all cases except 5, 11, 18 and 24. The same is true for part (d) in Delaunay elements. This is because the propagation time is less and both the Cartesian coordinates and Delaunay orbital elements have not changed much in this duration of time. For part (c), all the cases have higher KL values of the blue line as compared to the red line. This is because there is no transformation done after propagation as the EKF is propagated in Keplerian orbital elements.

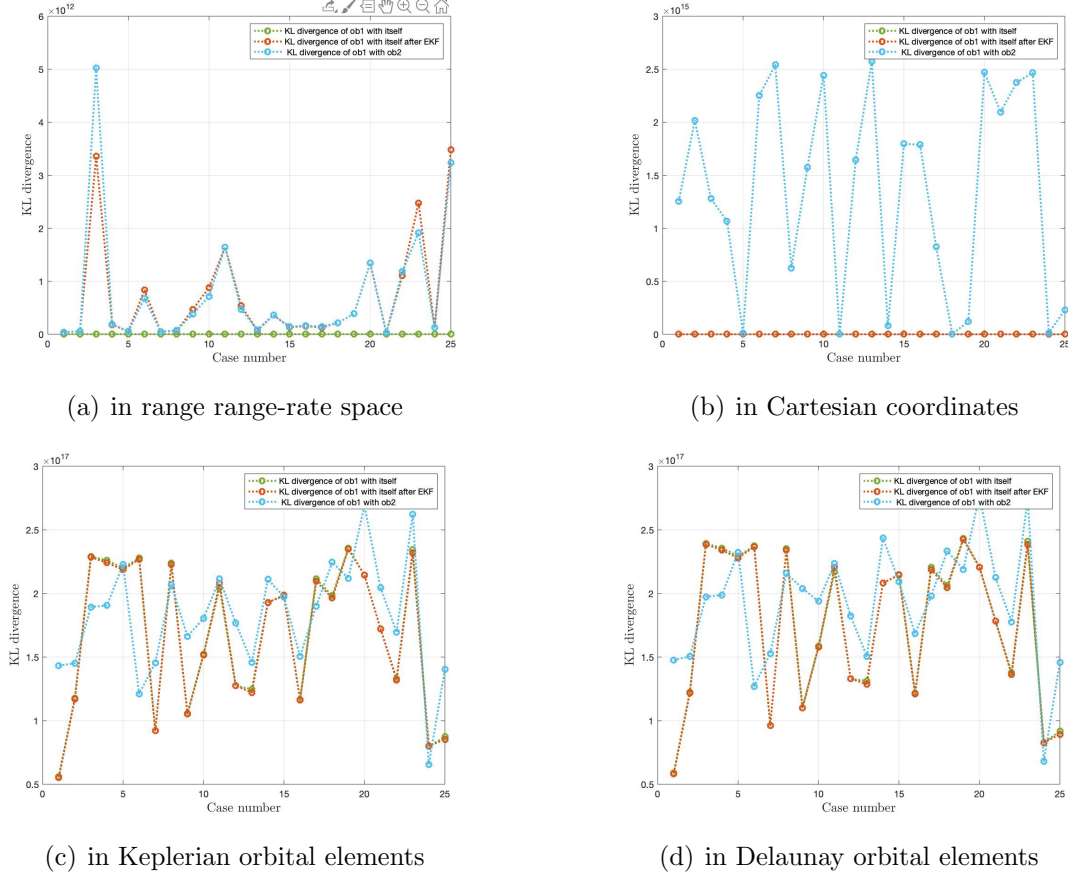


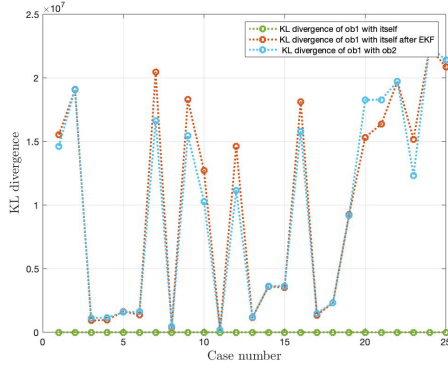
Fig. 11.16.: Plot for KL divergence vs case number. a) in range range-rate space b) in Cartesian coordinates c) in Keplerian orbital elements d) in Delaunay orbital elements for 10 minutes propagation (in Keplerian orbital elements) time using all components

Figure 11.16 shows the plot for KL divergence for different frames with respect to each case for 10 minutes of propagation time. For each case, all components are used for the calculation of KL divergence as discussed in section 8.1.1. Here, the green line represents KL divergence between GMM of object 1 with itself obtained from TSA at time  $t_2$ . In all parts, the KL value on the green line is non-zero as all components are used for finding the KL divergence.

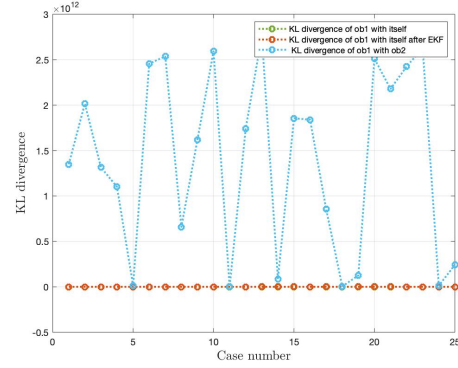
The red line represents KL divergence between two GMMs of object 1 obtained from TSA at time  $t_2$  and GMM propagation from time  $t_1$  to  $t_2$  using Extended Kalman filter in Keplerian orbital elements. For part (a), the KL values on the red line are

more than green line as the Admissible Region has shifted for 10 minutes propagation time. For part (b), in Cartesian coordinates, the red line still lies close to the green line because for two-body dynamics, the GMM in Cartesian coordinates has shifted but not too much. For part (c) and (d), the KL divergence values using all the components for the green and red line are close to each other because only mean anomaly is changing a little for two-body dynamics. Lastly, the blue line represents the KL divergence between GMM of object 2 obtained from TSA at time  $t_2$  and GMM of object 1 obtained from uncertainty propagation from time  $t_1$  to  $t_2$  using Extended Kalman filter Keplerian orbital elements. For part (a), the KL value on the blue line is higher than the red line for 19 cases. But these KL values lie very close to each other because the linearization takes place twice in this case for all components, hence, the errors also increase. For part (b), the KL values for blue line show a clear difference and hence can be used to correlate TSAs. In part (c) and (d), no such trend is followed by KL values on blue line because of using all components.

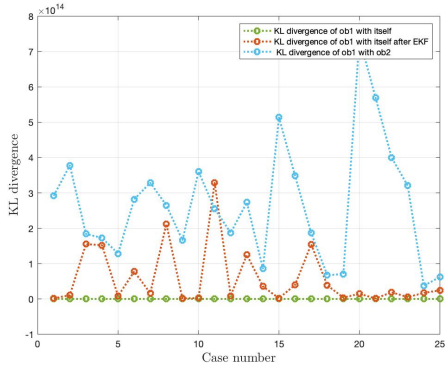
### GEO Scenario 3: Propagation Time-30 minutes



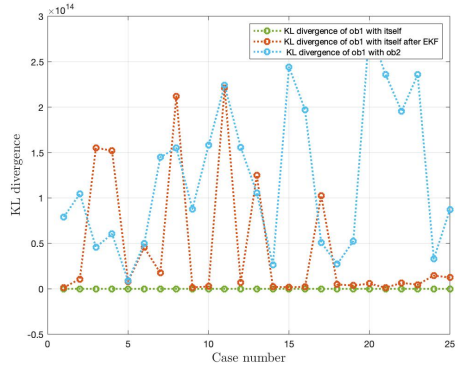
(a) in range range-rate space



(b) in Cartesian coordinates



(c) in Keplerian orbital elements



(d) in Delaunay orbital elements

Fig. 11.17.: Plot for KL divergence vs case number. a) in range range-rate space b) in Cartesian coordinates c) in Keplerian orbital elements d) in Delaunay orbital elements for 30 minutes propagation (in Keplerian orbital elements) time using optimized matching of components

Figure 11.17 shows the plot for KL divergence for different frames with respect to each case for 30 minutes of propagation time. For each case, optimized matching of components is used for calculation of KL divergence as discussed in section 8.1.2. Here, the green line represents KL divergence between GMM of object 1 with itself obtained from TSA at time  $t_2$ . For all parts, the green line shows zero value as *matchpairs* associates component with itself for the same GMM. The red line represents KL divergence between two GMMs of object 1 obtained from TSA at time  $t_2$

and GMM propagation from time  $t_1$  to  $t_2$  using Extended Kalman filter in Keplerian orbital elements. For part (a), the red line is higher than the green line by order of magnitude five at least. This happens because *matchpairs* associates with the nearest component for GMM which is not the same component anymore because the GMM has been propagated. For part (b), green line and red line are separated by an order of eight. For part (c) and (d), the KL values for the red line are more than green line because the GMM has changed even for a shorter period time. Lastly, the blue line represents the KL divergence between GMM of object 2 obtained from TSA at time  $t_2$  and GMM of object 1 obtained from uncertainty propagation from time  $t_1$  to  $t_2$  using Extended Kalman filter Keplerian orbital elements. In part (a), the KL values on the blue line are close to the red line because the Admissible Regions of both the objects lie close to each other. This could be because of the transformation from Keplerian orbital elements. For part (b), the blue line shows a higher value of KL divergence as compared to the red line because for 30 minutes the GMM in Cartesian coordinates still hasn't changed much. For part (c), all cases except for case 11 show higher values for the blue line as compared to the red line. Therefore, a correlation between two TSAs from the same object is still possible. For part (d), more points on the red line have a higher value than blue line as compared to part (c) because of numerical errors due to linearization encountered in this case.

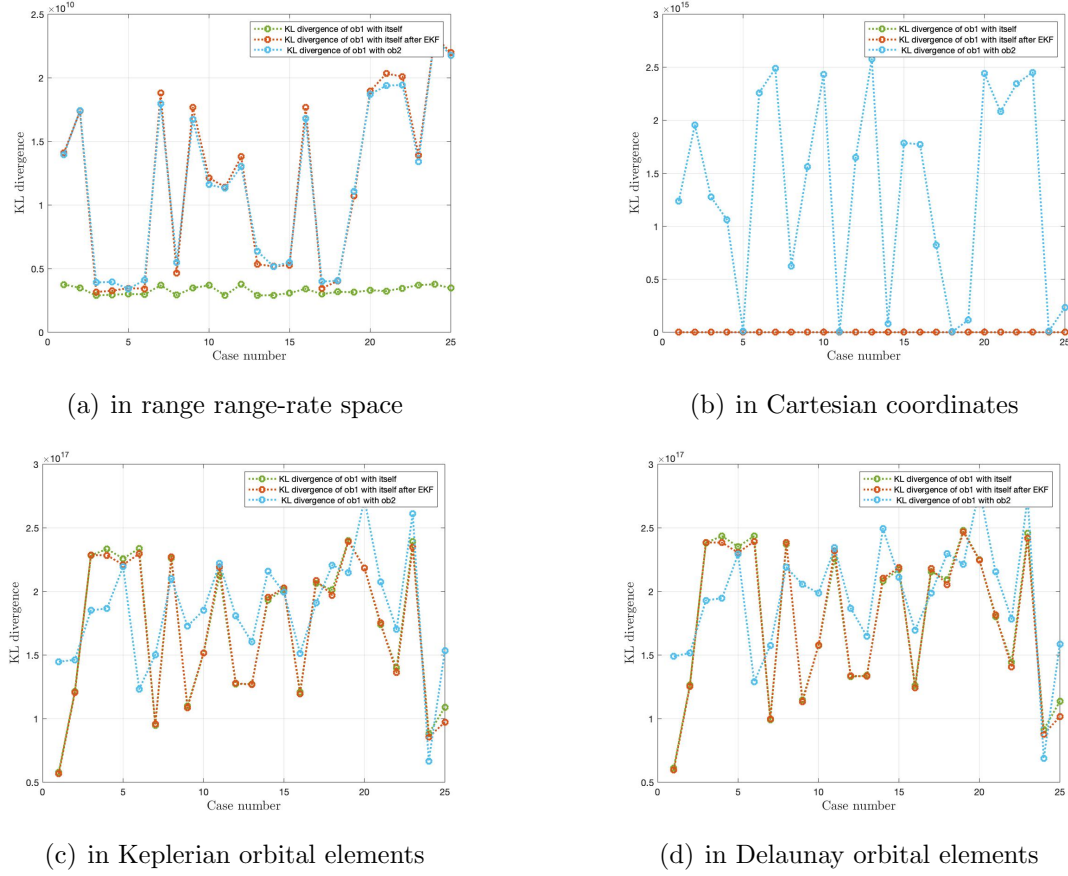


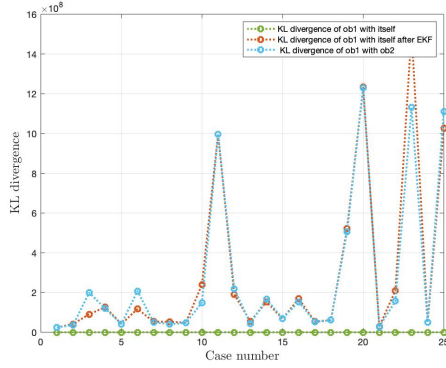
Fig. 11.18.: Plot for KL divergence vs case number. a) in range range-rate space b) in Cartesian coordinates c) in Keplerian orbital elements d) in Delaunay orbital elements for 30 minutes propagation (in Keplerian orbital elements) time using all components

Figure 11.18 shows the plot for KL divergence in different frames with respect to each case for 30 minutes of propagation time. For each case, all components are used for the calculation of KL divergence as discussed in section 8.1.1. Here, the green line represents KL divergence between GMM of object 1 with itself obtained from TSA at time  $t_2$ . The KL values for the green line are non-zero for all parts as all components are used to find the KL divergence. The red line represents KL divergence between two GMMs of object 1 obtained from TSA at time  $t_2$  and GMM propagation from time  $t_1$  to  $t_2$  using Extended Kalman filter in Keplerian orbital elements. For part (a), KL values are nearly the same order for the green and red line as the Admissible

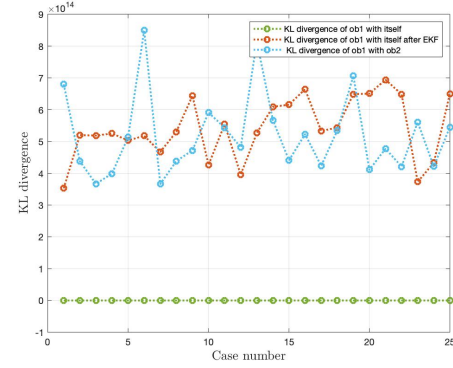
Region hasn't changed for 30 minutes. For part (b), the trend is the same as seen in figure 11.16 part (b). For part (c) and (d), the KL values on red and green line are of the same order. The GMMs in both these spaces are very close to each other as orbital elements have not changed much for 30 minutes propagation time.

Lastly, the blue line represents the KL divergence between GMM of object 2 obtained from TSA at time  $t_2$  and GMM of object 1 obtained from uncertainty propagation from time  $t_1$  to  $t_2$  using Extended Kalman filter Keplerian orbital elements. For part (a), the blue and red line closely follow each other. This is because of the observer to orbit changing in this space along with numerical errors due to linearization. For part (b), the blue line still has KL values which are much higher than the red line and therefore, a correlation between two TSAs from the same object can be seen easily. For part (c) and (d), using all components is bringing all the lines together and therefore, correlation is not possible here.

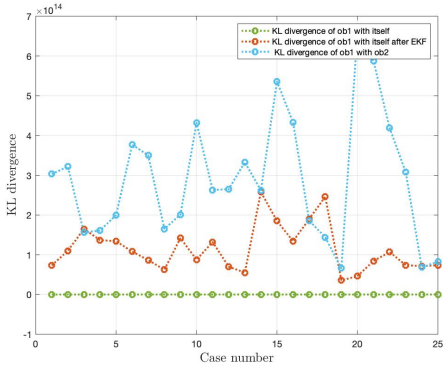
### GEO Scenario 3: Propagation Time-500 minutes



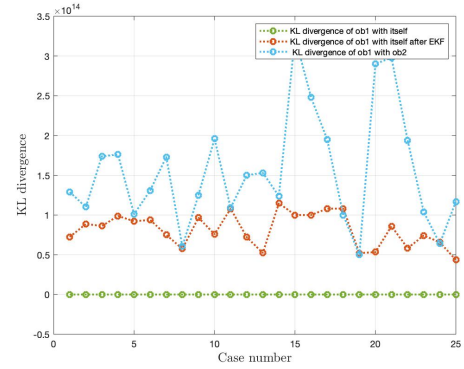
(a) in range range-rate space



(b) in Cartesian coordinates



(c) in Keplerian orbital elements



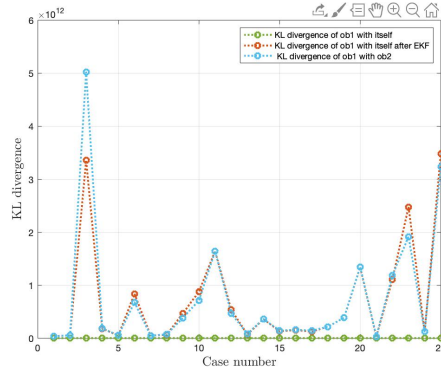
(d) in Delaunay orbital elements

Fig. 11.19.: Plot for KL divergence vs case number. a) in range range-rate space b) in Cartesian coordinates c) in Keplerian orbital elements d) in Delaunay orbital elements for 500 minutes propagation (in Keplerian orbital elements) time using optimized matching of components

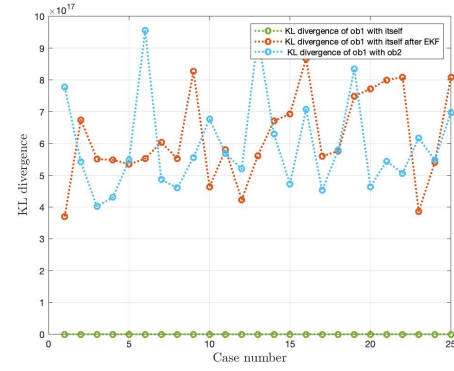
Figure 11.19 shows the plot for KL divergence in different frames with respect to each case for 500 minutes of propagation time. For each case, optimized matching of components is used for the calculation of KL divergence as discussed in section 8.1.2. Here, the green line represents KL divergence between GMM of object 1 with itself obtained from TSA at time  $t_2$ . The KL value on the green line for all parts are zero because optimized matching of components is used. The red line represents KL divergence between two GMMs of object 1 obtained from TSA at time  $t_2$  and



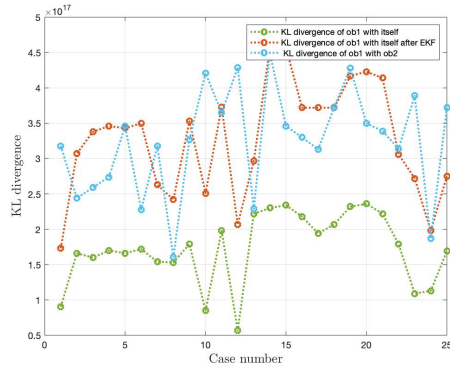
GMM propagation from time  $t_1$  to  $t_2$  using Extended Kalman filter in Keplerian orbital elements. For part (a), the red and green line have a difference of an order of magnitude 7 in them. This arises due to a change in the Admissible Region after EKF propagation. The same happens in part (b), (c) and (d) where red and green lines are separated by order of magnitude 14 for KL values. Lastly, the blue line represents the KL divergence between GMM of object 2 obtained from TSA at time  $t_2$  and GMM of object 1 obtained from uncertainty propagation from time  $t_1$  to  $t_2$  using Extended Kalman filter Keplerian orbital elements. For part (a), there is not much difference in KL values of blue and red line, therefore, making this space a difficult choice for finding correlation. For part (b), the object has travelled significantly for 500 minutes thereby changing the GMM after EKF such that the red line has higher points as compared to the blue line for about more than half of the cases. For part (c), as the propagation is done in Keplerian orbital elements in which the orbital elements of the same object should remain same only except mean anomaly, the KL values for the blue line has higher values since it is a different object except for case 3 and 18. The same is true for part (d), as Delaunay elements too are constant for a two-body dynamics of the same object except for mean anomaly. Therefore, even for a longer duration, Keplerian and Delaunay element space give a better correlation between TSAs of the same object.



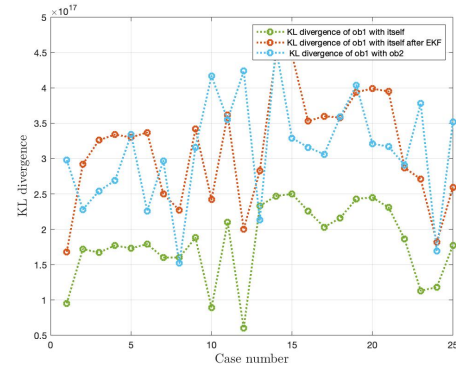
(a) in range range-rate space



(b) in Cartesian coordinates



(c) in Keplerian orbital elements



(d) in Delaunay orbital elements

Fig. 11.20.: Plot for KL divergence vs case number. a) in range range-rate space b) in Cartesian coordinates c) in Keplerian orbital elements d) in Delaunay orbital elements for 500 minutes propagation (in Keplerian orbital elements) time using all components

Figure 11.20 shows the plot for KL divergence in different frames with respect to each case for 500 minutes of propagation time. For each case, all components are used for the calculation of KL divergence as discussed in section 8.1.1. Here, the green line represents KL divergence between GMM of object 1 with itself obtained from TSA at time  $t_2$ . For all parts, KL values on green line are non-zero as all components are used for finding KL divergence. The red line represents KL divergence between two GMMs of object 1 obtained from TSA at time  $t_2$  and GMM propagation from time  $t_1$  to  $t_2$  using Extended Kalman filter in Keplerian orbital elements. In part (a), the KL values on the red line are of the two orders of magnitude higher than the green line

because of change in the Admissible Regions. In part (b), the KL values for the red line are an order of magnitude six higher than the green line because for 500 minutes, the GMM has changed significantly in Cartesian coordinates. In part (c) and (d), the red and green line are of the same order in both the frames as these orbital elements do not change much with time except for mean anomaly in two-body dynamics regime. Lastly, the blue line represents the KL divergence between GMM of object 2 obtained from TSA at time  $t_2$  and GMM of object 1 obtained from uncertainty propagation from time  $t_1$  to  $t_2$  using Extended Kalman filter Keplerian orbital elements. For part (a), the KL values on green and red line are close to each other and therefore making it hard to distinguish if the TSAs are from the same object. In part (b), due to longer duration of propagation, the GMM in Cartesian coordinate has changed considerably and therefore, for some cases, the red line has a higher value of KL as compared to the blue line. For part (c) and (d), more than half the points on the blue line show a lower value than the red line using all components. This worsens the correlation by making it hard to distinguish whether the TSAs are from the same object.

#### 11.4 LEO Scenario 1

As mentioned previously, there are two ways in which objects in LEO have been propagated. In LEO scenario 1, only those objects are taken which are visible before and after the time of propagation i.e angle of elevation is greater than zero at both times. The time of propagation is taken to be 3 minutes and 10 minutes. The EKF propagation is done in Cartesian coordinates for all the cases. Figure 11.21 shows the orbits of the objects taken for finding the overlap.

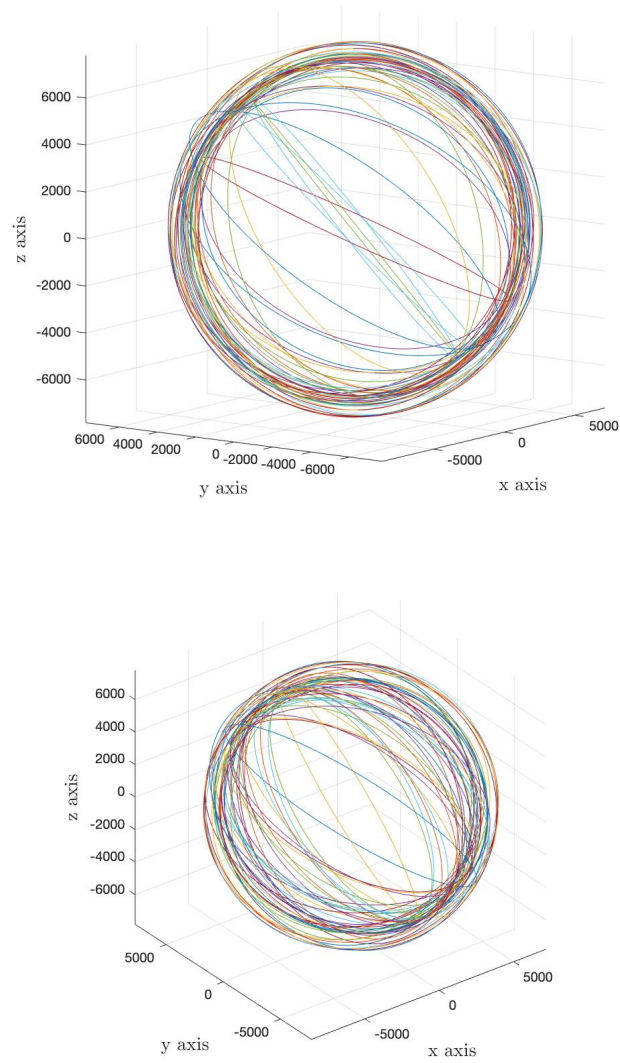


Fig. 11.21.: Plot of LEO objects for scenario 1

### LEO Scenario 1: Propagation Time-3 minutes

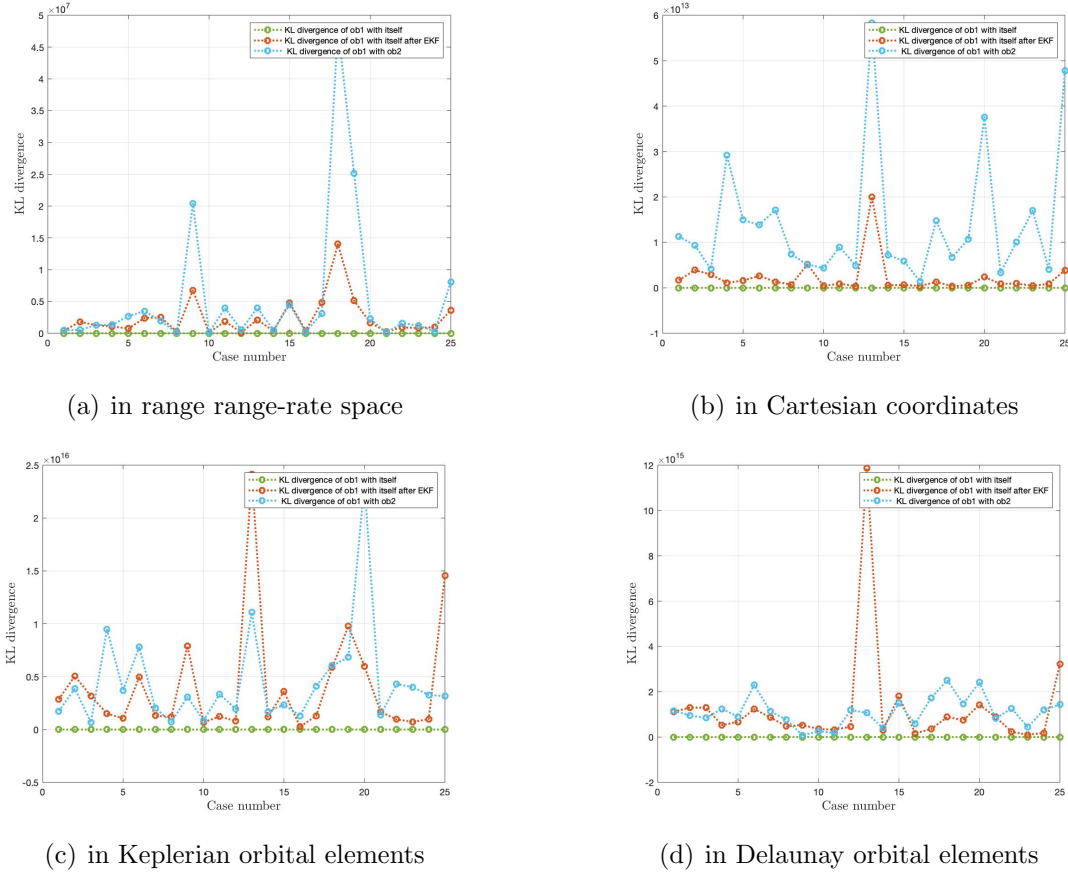
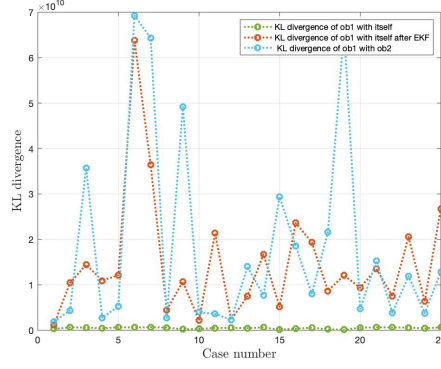


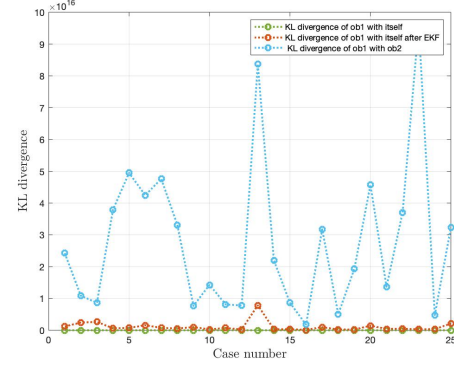
Fig. 11.22.: Plot for KL divergence vs case number. a) in range range-rate space b) in Cartesian coordinates c) in Keplerian orbital elements d) in Delaunay orbital elements for 3 minutes propagation time using optimized matching of components

Figure 11.22 shows the plot for KL divergence in different frames with respect to each case for 3 minutes of propagation time. For each case, optimized matching of components is used for the calculation of KL divergence as discussed in section 8.1.2. Here, the green line represents KL divergence between GMM of object 1 with itself obtained from TSA at time  $t_2$ . For all parts, the KL value associated with the green line is zero as optimized matching of components is used. The red line represents KL divergence between two GMMs of object 1 obtained from TSA at time  $t_2$  and GMM propagation from time  $t_1$  to  $t_2$  using Extended Kalman filter. For part (a), the red

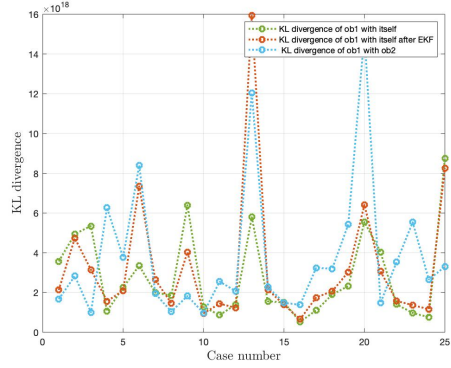
and green lines are separated by the order of magnitude six. This happens because the Admissible Region changes its shape after EKF in range range-rate space due to observer to orbit geometry change. For part (b), the green and red lines differ by an order of magnitude 12 but still lie close to each other since the object hasn't moved too far in 3 minutes. For part (c) and (d), the green and red line differ by an order of 14 because of change in GMM after EKF propagation for 3 minutes. The numerical error due to linearization also creep in here and make few points on the red line very high. Lastly, the blue line represents the KL divergence between GMM of object 2 obtained from TSA at time  $t_2$  and GMM of object 1 obtained from uncertainty propagation from time  $t_1$  to  $t_2$  using Extended Kalman filter. For part (a), the KL divergence values on the blue line are higher in most cases because the propagation time is very less. For part (b), the KL values on the blue line are higher than the ones on the red line and can be easily distinguished from the red line as compared to the range range-rate part. For part (c) and (d), the blue and red line are close to each other and the value of the red line is higher for more cases due to linearization effect. Therefore, no correlation criteria can be defined here.



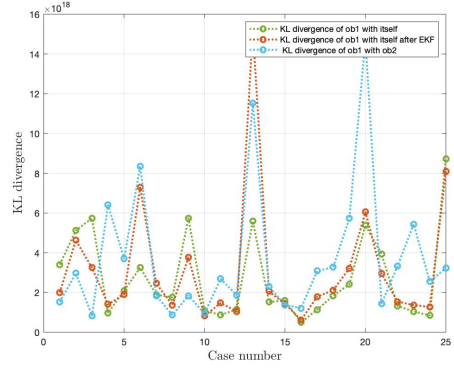
(a) in range range-rate space



(b) in Cartesian coordinates



(c) in Keplerian orbital elements



(d) in Delaunay orbital elements

Fig. 11.23.: Plot for KL divergence vs case number. a) in range range-rate space b) in Cartesian coordinates c) in Keplerian orbital elements d) in Delaunay orbital elements for 3 minutes propagation time using all components

Figure 11.23 shows the plot for KL divergence in different frames with respect to each case for 3 minutes of propagation time. For each case, all components are used for the calculation of KL divergence as discussed in section 8.1.1. Here, the green line represents KL divergence between GMM of object 1 with itself obtained from TSA at time  $t_2$ . For all plots, the KL value on the green line is non-zero as all the components are used for calculating KL divergence. The red line represents KL divergence between two GMMs of object 1 obtained from TSA at time  $t_2$  and GMM propagation from time  $t_1$  to  $t_2$  using Extended Kalman filter. For part (a), the red line now has a higher value than green because of the shift in the Admissible Region and using all components with all components. For part (b), the red and green lie

close to each other as the GMM in Cartesian coordinates for 3 minutes still has more overlap with the same TSA. For part (c) and (d), the KL values for the green and red line are close to each other but due to linearization, some points on the green line have even lesser values than the red line. Lastly, the blue line represents the KL divergence between GMM of object 2 obtained from TSA at time  $t_2$  and GMM of object 1 obtained from uncertainty propagation from time  $t_1$  to  $t_2$  using Extended Kalman filter. For part (a), the blue and red line have KL values close to each other due to change in the Admissible Regions. For part (b), the blue line has a higher value of KL as compared with KL values on the red line. This is because the duration of propagation is very less. For part (c) and (d), there is an increase in the KL value of green line due to using all components. The blue line shows KL values higher than red and green line only for about 12 cases because of the higher level of KL values for the green and red line. Therefore, correlation in these two spaces is difficult for associating two TSAs.



### LEO Scenario 1: Propagation Time-10 minutes

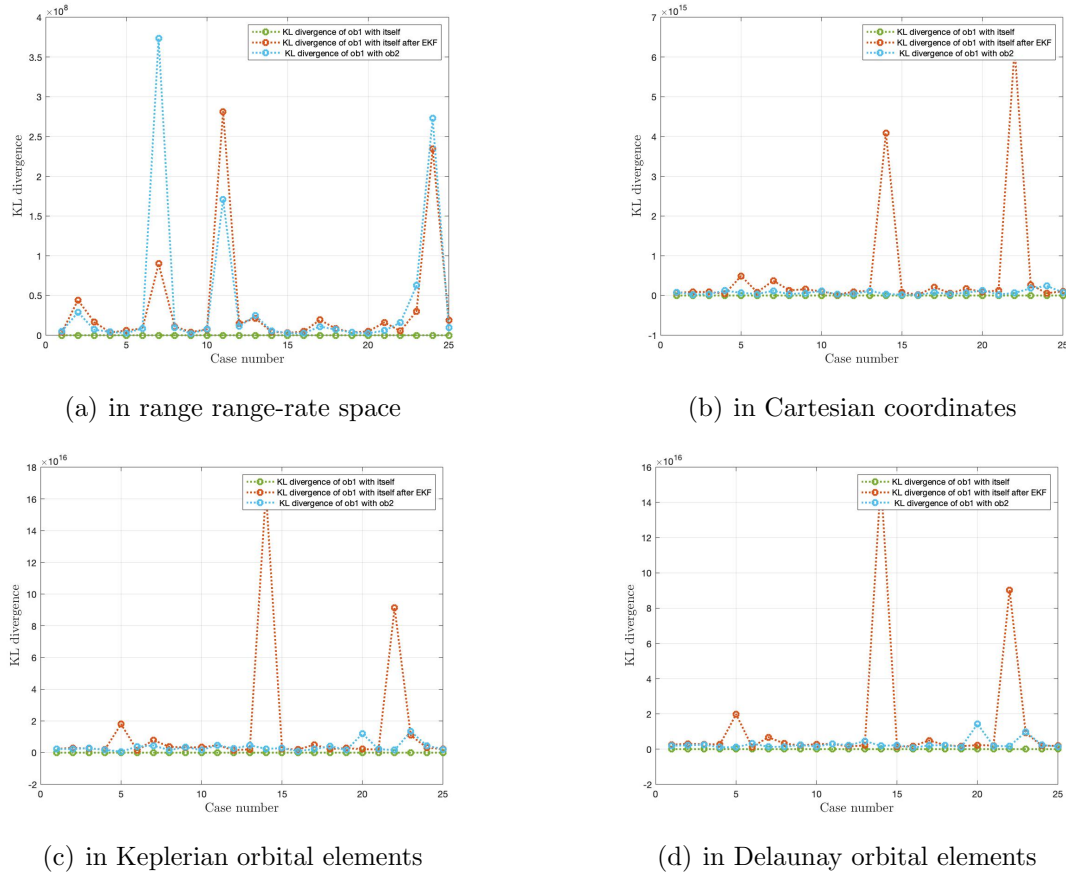


Fig. 11.24.: Plot for KL divergence vs case number. a) in range range-rate space b) in Cartesian coordinates c) in Keplerian orbital elements d) in Delaunay orbital elements for 10 minutes propagation time using optimized matching of components

Figure 11.24 shows the plot for KL divergence in different frames with respect to each case for 3 minutes of propagation time. For each case, optimized matching of components is used for the calculation of KL divergence as discussed in section 8.1.2. Here, the green line represents KL divergence between GMM of object 1 with itself obtained from TSA at time  $t_2$ . For all parts, the KL value associated with the green line is zero as optimized matching of components is used. The red line represents KL divergence between two GMMs of object 1 obtained from TSA at time  $t_2$  and GMM propagation from time  $t_1$  to  $t_2$  using Extended Kalman filter. For part (a),

the red and green line lie close to each other except for few cases with more gap between them. This happens because the Admissible Region changes its shape more for 10 minutes after EKF in range range-rate space due to observer to orbit geometry change. For part (b), the green and red line differ by an order of magnitude 13 but still lie close to each other since the object hasn't moved too far in 3 minutes. For part (c) and (d), the green and red line differ by an order of 15 because of change in GMM after EKF propagation for 10 minutes. The numerical error due to linearization also creep in here and make few points on the red line very high. Lastly, the blue line represents the KL divergence between GMM of object 2 obtained from TSA at time  $t_2$  and GMM of object 1 obtained from uncertainty propagation from time  $t_1$  to  $t_2$  using Extended Kalman filter. For part (a), the KL divergence values on the blue line have fewer points higher than the red line as compared to 3 minutes case because of more shift in Admissible Region. For part (b), (c) and (d), the KL values on the blue line are very close to points on the red line, therefore, it is difficult to comment on correlation based on KL values.

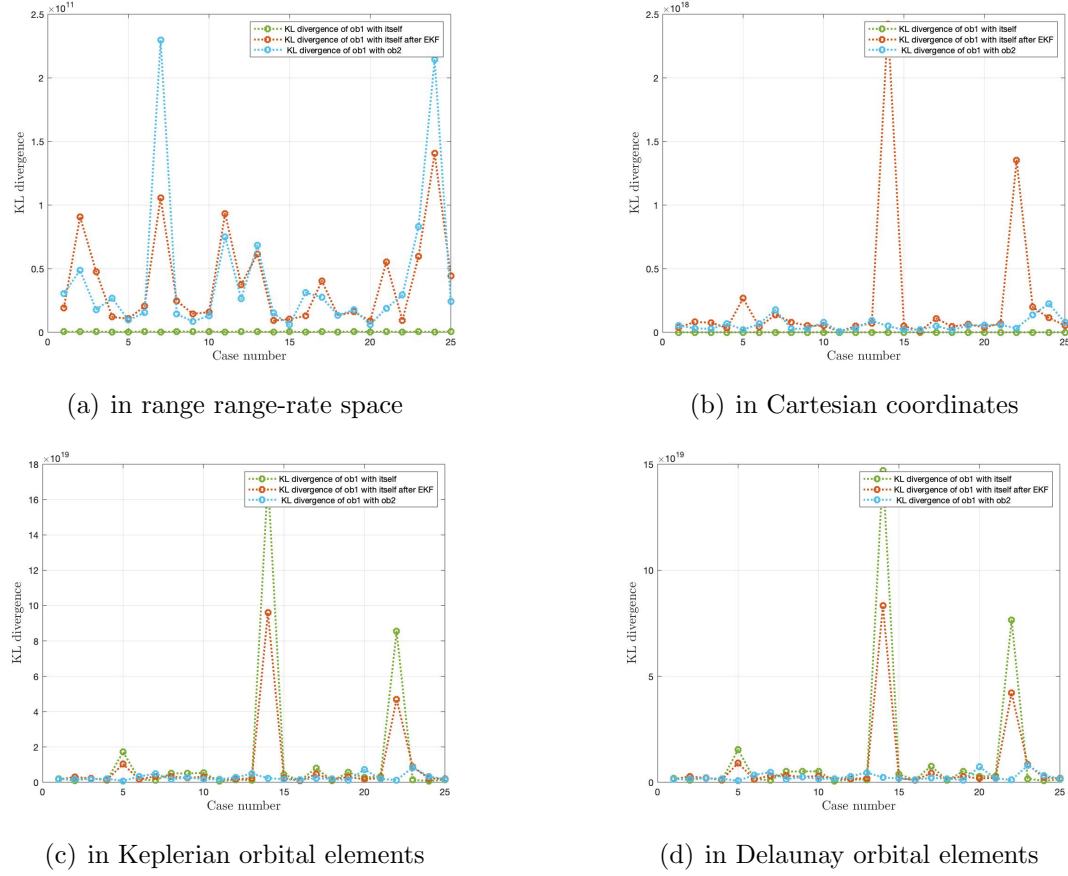


Fig. 11.25.: Plot for KL divergence vs case number. a) in range range-rate space b) in Cartesian coordinates c) in Keplerian orbital elements d) in Delaunay orbital elements for 10 minutes propagation time using all components

Figure 11.25 shows the plot for KL divergence in different frames with respect to each case for 3 minutes of propagation time. For each case, all components are used for the calculation of KL divergence as discussed in section 8.1.1. Here, the green line represents KL divergence between GMM of object 1 with itself obtained from TSA at time  $t_2$ . For all plots, the KL value on the green line is non-zero as all the components are used for calculating KL divergence. The red line represents KL divergence between two GMMs of object 1 obtained from TSA at time  $t_2$  and GMM propagation from time  $t_1$  to  $t_2$  using Extended Kalman filter. For part (a), the red line now has a higher value than green because of the shift in the Admissible Region and using all components with all components. For part (b), the red and green lie

close to each other as the GMM in Cartesian coordinates for 10 minutes still has more overlap with the same TSA except for case 5, 14 and 22. For part (c) and (d), the KL values for the green and red line are close to each other but due to linearization, some points on the green line have even lesser values than the red line. Lastly, the blue line represents the KL divergence between GMM of object 2 obtained from TSA at time  $t_2$  and GMM of object 1 obtained from uncertainty propagation from time  $t_1$  to  $t_2$  using Extended Kalman filter. For part (a), the blue and red line have KL values close to each other due to change in the Admissible Regions. For part (b), the blue line has KL values very close to the red line or much smaller for case 5, 14 and 22. For part (c) and (d), there is an increase in the KL value of green line due to using all components. The blue line shows KL values very close to red line and in some cases even smaller than the green line. This is because of the linearization effect along with using all components. Therefore, correlation in these three spaces is difficult for associating two TSAs.

### 11.5 LEO Scenario 2

For LEO scenario 2, objects are taken without taking visibility in the account. The state and uncertainty related to these objects are propagated using Extended Kalman filter in Cartesian coordinates. After the propagation, components having a position of object less than the radius of the Earth are eliminated and the remaining ones are used for finding the KL divergence analysis. Figure 11.26 shows the orbits of the objects taken for finding the overlap.

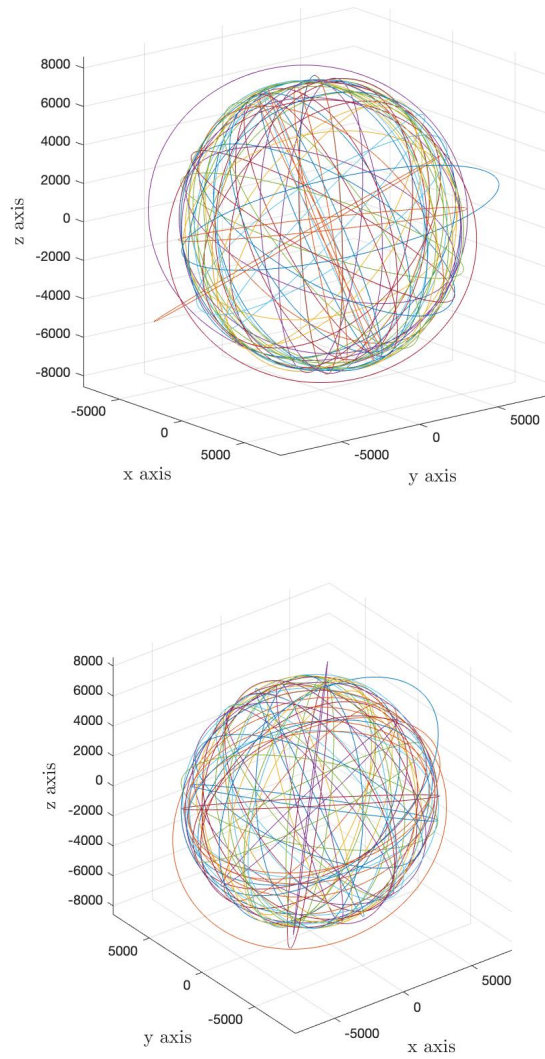
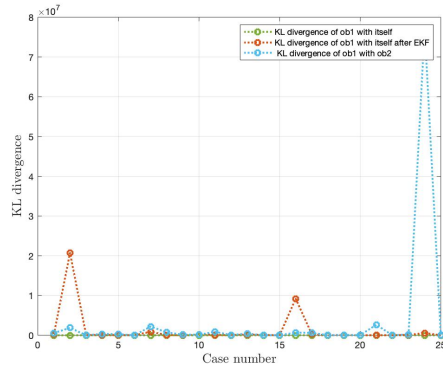
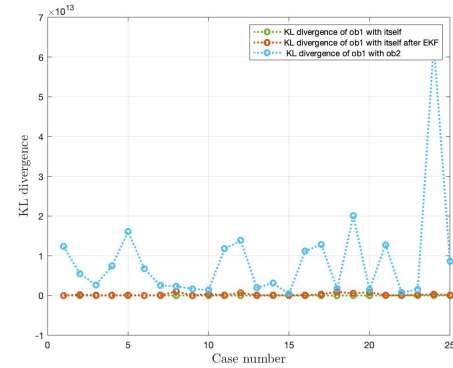


Fig. 11.26.: Plot of LEO objects for scenario 2

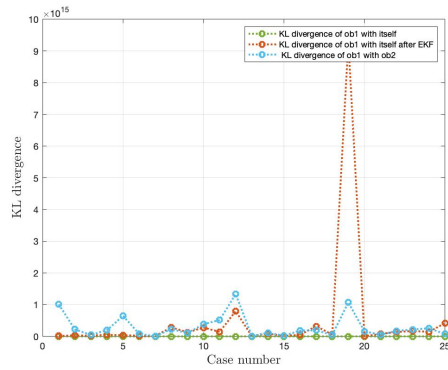
## LEO Scenario 2: Propagation Time-3 minutes



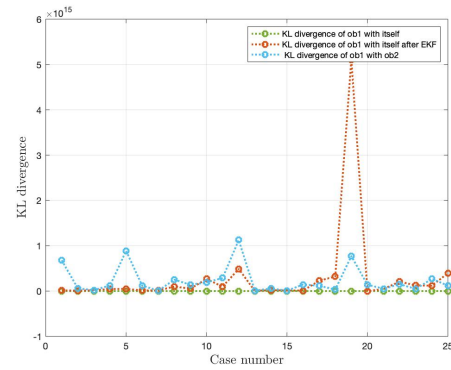
(a) in range range-rate space



(b) in Cartesian coordinates



(c) in Keplerian orbital elements



(d) in Delaunay orbital elements

Fig. 11.27.: Plot for KL divergence vs case number. a) in range range-rate space b) in Cartesian coordinates c) in Keplerian orbital elements d) in Delaunay orbital elements for 3 minutes propagation time using optimized matching of components

Figure 11.27 shows the plot for KL divergence in different frames with respect to each case for 3 minutes of propagation time. For each case, optimized matching of components is used for the calculation of KL divergence as discussed in section 8.1.2. Here, the green line represents KL divergence between GMM of object 1 with itself obtained from TSA at time  $t_2$ . For all parts, the KL values for green lines are zero as optimized matching of components is used. The red line represents KL divergence between two GMMs of object 1 obtained from TSA at time  $t_2$  and GMM propagation from time  $t_1$  to  $t_2$  using Extended Kalman filter. For part (a), the red line is closely

aligned with the green line as the Admissible Region has not changed much for 3 minutes propagation time. For part (b), (c) and (d), the red line is close to green line except for case 19 in part (c) and (d). This is because the GMM in these spaces too hasn't changed much over the propagation time. Lastly, the blue line represents the KL divergence between GMM of object 2 obtained from TSA at time  $t_2$  and GMM of object 1 obtained from uncertainty propagation from time  $t_1$  to  $t_2$  using Extended Kalman filter. For part (a), the KL values for the blue line are higher but are very close to red line except for cases 2 and 16. This is because the Admissible Region of second TSA is close to the Admissible Region of first TSA. For part (b), the blue line gives a higher value of KL as compared to the red line for all cases. For part (c) and (d), the blue line shows a similar trend with higher KL values for all cases except case 19 and 25. Even though KL values are higher than the red and green line, it is difficult to comment on the correlation criteria as they are very close to each other.

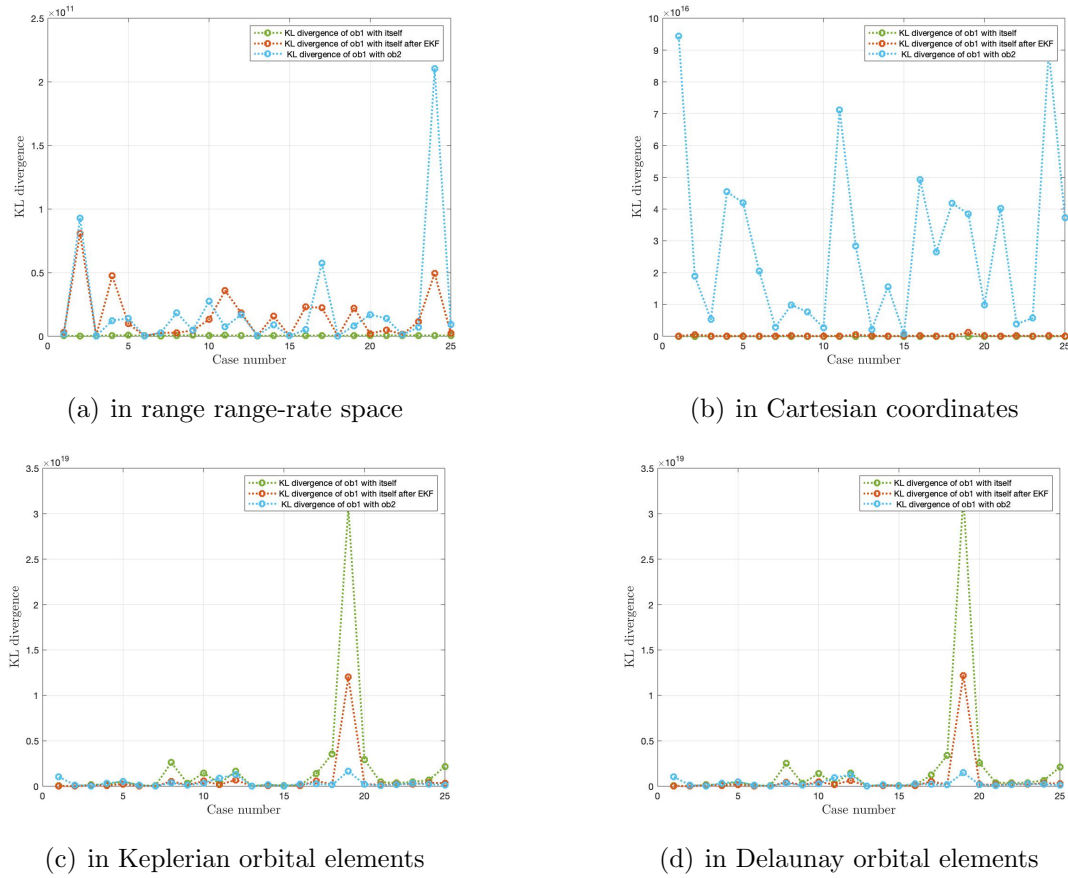


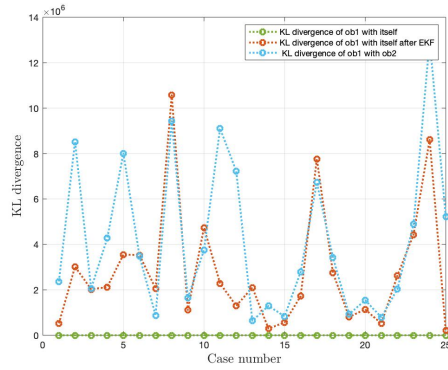
Fig. 11.28.: Plot for KL divergence vs case number. a) in range range-rate space b) in Cartesian coordinates c) in Keplerian orbital elements d) in Delaunay orbital elements for 3 minutes propagation time using all components

Figure 11.28 shows the plot for KL divergence in different frames with respect to each case for 3 minutes of propagation time. For each case, all components are used for the calculation of KL divergence as discussed in section 8.1.1. Here, the green line represents KL divergence between GMM of object 1 with itself obtained from TSA at time  $t_2$ . The KL value of the green line for all parts is non-zero as all the components are used for finding the KL divergence. The red line represents KL divergence between two GMMs of object 1 obtained from TSA at time  $t_2$  and GMM propagation from time  $t_1$  to  $t_2$  using Extended Kalman filter. For part (a) and (b), the green line still is close to the red line even after using all components. For part (c) and (d), the KL values for green line go even higher than the red line and this can

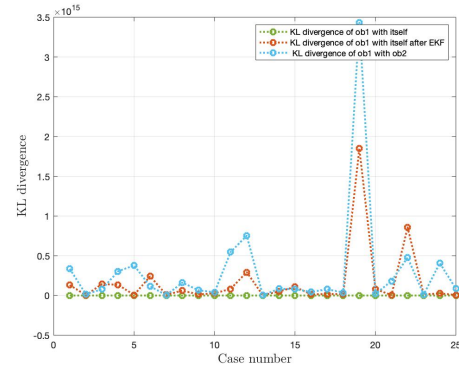


be attributed to the numerical errors accumulated due to linearization. Lastly, the blue line represents the KL divergence between GMM of object 2 obtained from TSA at time  $t_2$  and GMM of object 1 obtained from uncertainty propagation from time  $t_1$  to  $t_2$  using Extended Kalman filter. For part (a), only a few points on the blue line have a higher value as compared to the red and green line because of using all components. For part (b), the KL values for the blue line are much higher using all components and can be used to associate TSAs. For part (c) and (d), the KL value for the blue line is either too close or are smaller than the green and red line. This is because of using all components along with linearization for transformation to these spaces.

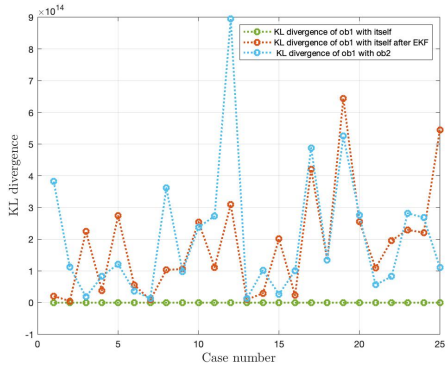
## LEO Scenario 2: Propagation Time-10 minutes



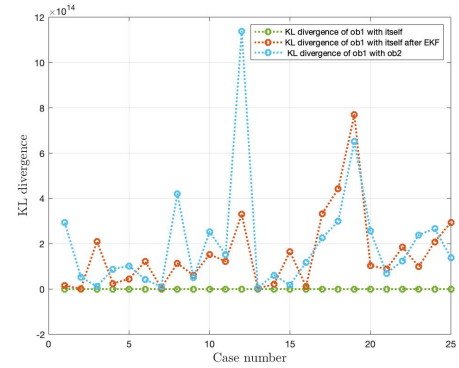
(a) in range range-rate space



(b) in Cartesian coordinates



(c) in Keplerian orbital elements



(d) in Delaunay orbital elements

Fig. 11.29.: Plot for KL divergence vs case number. a) in range range-rate space b) in Cartesian coordinates c) in Keplerian orbital elements d) in Delaunay orbital elements for 10 minutes propagation time using optimized matching of components

Figure 11.29 shows the plot for KL divergence in different frames with respect to each case for 10 minutes of propagation time. For each case, optimized matching of components is used for the calculation of KL divergence as discussed in section 8.1.2. Here, the green line represents KL divergence between GMM of object 1 with itself obtained from TSA at time  $t_2$ . For all parts, the KL values for the green line are zero as optimized matching of components is used which associated the component with itself for the same GMM. The red line represents KL divergence between two GMMs of object 1 obtained from TSA at time  $t_2$  and GMM propagation from time  $t_1$  to  $t_2$

using Extended Kalman filter. For part (a), there is an increase in the gap between the red and green line because the Admissible Region has changed even more for 10 minutes. Similarly, for part (b), the GMM after EKF has changed thereby increasing the gap between red and green line. For part (c) and (d), the red line is still higher than the green line due to change in GMMs. Lastly, the blue line represents the KL divergence between GMM of object 2 obtained from TSA at time  $t_2$  and GMM of object 1 obtained from uncertainty propagation from time  $t_1$  to  $t_2$  using Extended Kalman filter. For part (a), the blue line has KL values which are close to KL values for the red line for more than half the cases. For part (b), the KL value for blue line are higher than red line except for 4 cases. For part (c) and (d), no such trend exists for KL values on blue which can be generalized to correlate two TSAs. This happens because of the transformation to the orbital element spaces.

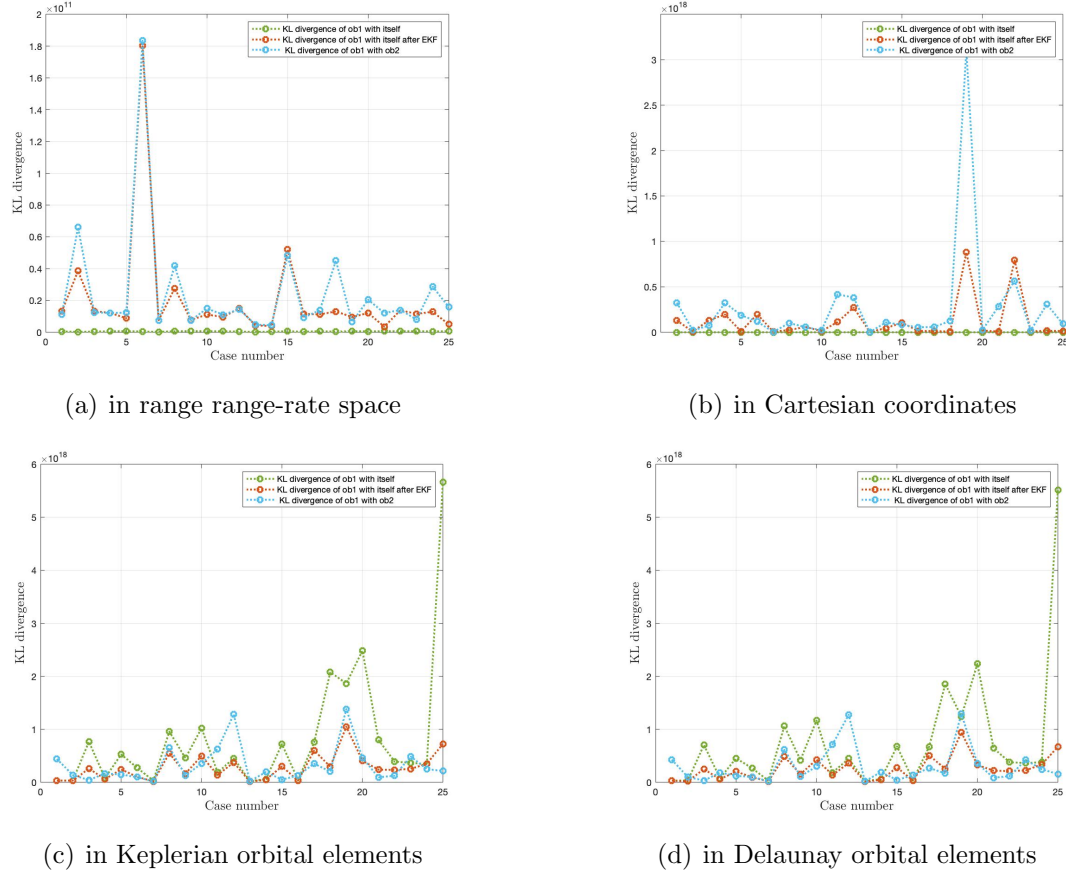


Fig. 11.30.: Plot for KL divergence vs case number. a) in range range-rate space b) in Cartesian coordinates c) in Keplerian orbital elements d) in Delaunay orbital elements for 10 minutes propagation time using all components

Figure 11.30 shows the plot for KL divergence in different frames with respect to each case for 10 minutes of propagation time. For each case, all components are used for the calculation of KL divergence as discussed in section 8.1.1. Here, the green line represents KL divergence between GMM of object 1 with itself obtained from TSA at time  $t_2$ . The KL values for the green line are non-zero for all parts as all the components are used for finding KL divergence. The red line represents KL divergence between two GMMs of object 1 obtained from TSA at time  $t_2$  and GMM propagation from time  $t_1$  to  $t_2$  using Extended Kalman filter. For part (a), the KL values red line is higher than the green line as the Admissible Region has changed EKF due to change in observation geometry. For part (b), a similar trend is observed for the red

and green line. For (c) and (d), the green line shows KL values higher than KL values for the red line because of numerical errors accumulated due to linearization. Lastly, the blue line represents the KL divergence between GMM of object 2 obtained from TSA at time  $t_2$  and GMM of object 1 obtained from uncertainty propagation from time  $t_1$  to  $t_2$  using Extended Kalman filter. For part (a) and (b), the blue line shows KL values higher than the red and green line for most cases. For part (c) and (d), the KL values for the green line is highest due to the numerical errors accumulated along with the use of all components for finding KL divergence.

## 12. SUMMARY

### 12.1 Conclusions

For the detection of new objects, the sky is scanned in an organized manner. These observations are made mostly with optical sensors for Medium Earth Orbits (MEO) and Geosynchronous Earth Orbits region (GEO). Each set of observation consists of two angles and several of these observations together form a Too Short Arc (TSA). For a newly detected unknown object, one TSA, which cover negligible part of an object's orbit, is not sufficient for the initial orbit determination as it only has information on one set of angles and angle rates. Therefore, it is required to correlate TSAs to find out if they belong to the same object in order to be able to determine an initial orbit. For this thesis, the framework of using the Gaussian Mixture Model representation of the Admissible Region in combination with the Extended Kalman filter is used for propagating the TSAs to the same epoch. These TSAs are then correlated using the concept of Kullback-Leibler divergence. The Kullback-Leibler divergence is calculated in different coordinates frames/orbital element spaces to find the best suited one for finding the overlap between two TSAs most reliably. The different coordinate frames/ orbital element spaces that are used are range range-rate space, Cartesian coordinates, Keplerian orbital elements and Delaunay orbital elements. Since there is no closed-form equation for finding the Kullback-Leibler divergence between two Gaussian Mixtures, two strategies have been developed and tested, namely, optimized matching of components and using all components. Numerical error build-up is observed during the Extended Kalman filter propagation. This is due to the fact of a Gaussian Mixture obtained from the Admissible Region, which is large in range and range-rate and small in angles and angular rate space. Two ways of covariance propagation have been tested. The covariance propagation using state transition ma-

trix has been adopted as least numerical errors accumulated for this method during Extended Kalman filter propagation. Furthermore, two methods for dealing with the rank deficient matrices have been tested, namely, Singular Value Decomposition and Cholesky decomposition. It is seen that the Cholesky decomposition better approximated the inverse of a covariance matrix in the presence of numerical errors and, therefore, has been used for this thesis. For selecting the objects, Low-Earth (LEO) and Geosynchronous Earth orbits have been used for different scenarios using different time duration. In GEO scenario one, visible GEO objects are selected from TLE data and the TSAs generated from them are correlated using Kullback-Leibler divergence for 10 minutes, 30 minutes and 500 minutes. In GEO scenario two, visible GEO objects are selected from TLE data and are sorted in Keplerian orbital elements space and the TSAs generated from them are correlated using Kullback-Leibler divergence for 10 minutes, 30 minutes and 500 minutes. The propagation in the Extended Kalman filter is done using Cartesian coordinates for GEO scenario one and two. For GEO scenario three, the same procedure is followed as GEO scenario one except that the Extended Kalman filter is propagated in Keplerian orbital elements.

For LEO objects, two scenarios have been developed. For LEO scenario one, visible LEO objects are taken for finding the overlap between the TSAs generated by them. For LEO scenario two, LEO objects are taken without taking visibility into account and after Extended Kalman filter propagation, the components with position less than the radius of the Earth are eliminated. For both of these scenarios, the Extended Kalman Filter is propagated in Cartesian coordinates space.

When matching all components with all components, the Kullback-Leibler divergence is not able to differentiate even when matching the same TSA or two TSAs of the same object. For GEO objects, Kullback-Leibler divergence using optimized matching of components and using all components with all components is able to distinguish between TSAs from two different objects as compared with TSAs from the same object up to 30 minutes of propagation time in Cartesian coordinates. This does not hold when the propagation time increases. For LEO objects, Kullback-Leibler di-

vergence using both the optimized matching of components and all components with all components is able to give a correlation between TSAs in Cartesian coordinates. In all, LEO and GEO cases do not show a clear distinction between correct correlations (when TSAs are indeed from the same object) when all components have been matched with all components in the Kullback-Leibler divergence computation independent of the coordinate frame in which the comparison has been made for propagation times more than 3 minutes and 30 minutes, respectively.

In range range-rate space, the Admissible Region changes considerably even for a 30 minutes of propagation time for GEO objects due to the change in observer to orbit geometry, which affects the shape of the Admissible Region and hence, the Kullback-Leibler divergence between two TSAs belonging to the same object. Therefore, as expected range range-rate frame cannot be exploited to indicate a clear overlap between two TSAs from the same object. In the Cartesian coordinates, the correlation using Kullback-Leibler divergence depends on the propagation time. For a duration up to 10 minutes, the Kullback-Leibler divergence between two TSAs coming from different objects is able to show correlation for both GEO and LEO cases. As the propagation time increases, the Kullback-Leibler divergence is not able to correlate the TSAs because of a larger shift in GMM of the TSA in Cartesian coordinates and numerical errors accumulation during the Extended Kalman Filter. In Keplerian and Delaunay orbital elements, Kullback-Leibler divergence is expected to give a higher value between two TSAs from the different object because all the orbital elements except for mean anomaly remain fixed in both the frames. However, it has been shown via Monte Carlo simulations, that the linearization used for transforming from one space to another has a tremendous impact on the Kullback-Leibler divergence. As a result, Kullback-Leibler divergence in these orbital element spaces is not able to correlate TSAs from the same object, especially for a duration longer than ten minutes. However, this is overcome by propagating the Extended Kalman filter in Keplerian orbital elements. Thus, the errors accumulated due to linearization after



Extended Kalman Filter have been reduced. This resulted in better correlation by Kullback-Leibler divergence even for 500 minutes of propagation time.

As the propagation time of object increases more than 30 minutes, the mean associated with each component shifts along with the shape of the uncertainty around that mean. This makes it difficult for Kullback-Leibler divergence to associate an object with itself because, due to the shift, it is possible that the GMM obtained from object one after Extended Kalman Filter has moved farther from the object itself as compared to the GMM of object two.

## 12.2 Recommendations

For time durations up to 30 minutes in GEO, Cartesian coordinates are best suited for finding the overlap between two TSAs to solve the correlation problem. However, for a longer time duration in GEO region, as the state of the object changes significantly, KL divergence is not able to distinguish between two TSAs of the same or of different objects. For longer propagation times of 500 minutes, Extended Kalman Filter propagation in Keplerian orbital elements gives more overlap with the same object. Therefore, depending upon length of time, different setups can be used for finding the overlap. For LEO objects, Kullback-Leibler divergence can differentiate between TSAs from different objects in Cartesian coordinate frame with up to three minutes of propagation time. Therefore, this frame can be used for a shorter time difference between two TSAs in LEO region. In the real world, two-body dynamics for the motion of the object does not hold. Therefore, the effects of perturbations should also be taken into account before applying the procedure followed in this thesis. For longer propagation time, the numerical errors accumulated have a significant impact on the Kullback-Leibler divergence, therefore the application of Unscented Kalman filter might be useful as it uses point transformation for transforming from one space to another.

## REFERENCES

## REFERENCES

- [1] A. Rossi, “Population models of space debris,” *Proceedings of the International Astronomical Union*, vol. 2004, no. IAUC197, pp. 427–438, 2004.
- [2] G. Tommei, A. Milani, and A. Rossi, “Orbit determination of space debris: admissible regions,” *Celestial Mechanics and Dynamical Astronomy*, vol. 97, no. 4, pp. 289–304, 2007.
- [3] A. Milani, G. F. Gronchi, M. d. Vitturi, and Z. Knežević, “Orbit determination with very short arcs. i admissible regions,” *Celestial Mechanics and Dynamical Astronomy*, vol. 90, no. 1-2, pp. 57–85, 2004.
- [4] A. Milani, G. F. Gronchi, Z. Knežević, M. E. Sansaturio, and O. Arratia, “Orbit determination with very short arcs: II. identifications,” *Icarus*, vol. 179, no. 2, pp. 350–374, 2005.
- [5] A. Milani and Z. Knežević, “From astrometry to celestial mechanics: orbit determination with very short arcs,” *Celestial Mechanics and Dynamical Astronomy*, vol. 92, no. 1-3, pp. 1–18, 2005.
- [6] J. M. Maruskin, D. J. Scheeres, and K. T. Alfriend, “Correlation of optical observations of objects in earth orbit,” *Journal of Guidance, Control, and Dynamics*, vol. 32, no. 1, pp. 194–209, 2009.
- [7] D. Farnocchia, G. Tommei, A. Milani, and A. Rossi, “Innovative methods of correlation and orbit determination for space debris,” *Celestial Mechanics and Dynamical Astronomy*, vol. 107, no. 1-2, pp. 169–185, 2010.
- [8] K. Fujimoto and D. J. Scheeres, “Correlation of optical observations of earth-orbiting objects and initial orbit determination,” *Journal of guidance, control, and dynamics*, vol. 35, no. 1, pp. 208–221, 2012.
- [9] —, “Short-arc correlation and initial orbit determination for space-based observations.”
- [10] A. Milani, G. Tommei, D. Farnocchia, A. Rossi, T. Schildknecht, and R. Jehn, “Correlation and orbit determination of space objects based on sparse optical data,” *Monthly Notices of the Royal Astronomical Society*, vol. 417, no. 3, pp. 2094–2103, 2011.
- [11] F. Khoury, C. Frueh, and S. Francis, “Aas 17-452: Initial orbit identification: Comparison of admissible region mapping for too short arc observations,” 02 2017.
- [12] R. Musci, T. Schildknecht, M. Ploner, and G. Beutler, “Orbit improvement for gto objects using follow-up observations,” *Advances in Space Research - ADV SPACE RES*, vol. 35, pp. 1236–1242, 12 2005.

- [13] M. J. Holzinger, D. J. Scheeres, and K. T. Alfriend, "Object correlation, maneuver detection, and characterization using control distance metrics," *Journal of Guidance, Control, and Dynamics*, vol. 35, no. 4, pp. 1312–1325, 2012.
- [14] K. J. DeMars and M. K. Jah, "Probabilistic initial orbit determination using gaussian mixture models," *Journal of Guidance, Control, and Dynamics*, vol. 36, no. 5, pp. 1324–1335, 2013.
- [15] A. H. Jazwinski, *Stochastic processes and filtering theory*. Courier Corporation, 2007.
- [16] S. Kullback and R. A. Leibler, "On information and sufficiency," *The annals of mathematical statistics*, vol. 22, no. 1, pp. 79–86, 1951.
- [17] C. Frueh, "Lecture notes of the course : Space traffic management,purdue university," Fall 2018.
- [18] S. M. Ross *et al.*, *A first course in probability*. Pearson Prentice Hall Upper Saddle River, NJ, 2006, vol. 7.
- [19] J. D. Gibbon, "Lecture notes of mathematics course : Imperial college london."
- [20] O. Montenbruck and T. Pfleger, *Astronomy on the personal computer*. Springer, 2013.
- [21] O. Montenbruck, E. Gill, and F. Lutze, "Satellite orbits: models, methods, and applications," *Appl. Mech. Rev.*, vol. 55, no. 2, pp. B27–B28, 2002.
- [22] D. A. Vallado, *Fundamentals of astrodynamics and applications*. Springer Science & Business Media, 2001, vol. 12.
- [23] R. A. Broucke and P. J. Cefola, "On the equinoctial orbit elements," *Celestial mechanics*, vol. 5, no. 3, pp. 303–310, 1972.
- [24] J. P. Vinti, *Orbital and celestial mechanics*. American Institute of Aeronautics and Astronautics, 1998.
- [25] B. T. Vo, "Random finite sets in multi-object filtering," Ph.D. dissertation, Cite-seer, 2008.
- [26] R. P. Mahler, *Statistical multisource-multitarget information fusion*. Artech House Norwood, MA, 2007, vol. 685.
- [27] G. H. Golub and C. F. Van Loan, *Matrix computations*. JHU press, 2012, vol. 3.
- [28] T. M. Cover and J. A. Thomas, *Elements of information theory*. John Wiley & Sons, 2012.
- [29] P. C. Mahalanobis, "On the generalized distance in statistics." National Institute of Science of India, 1936.